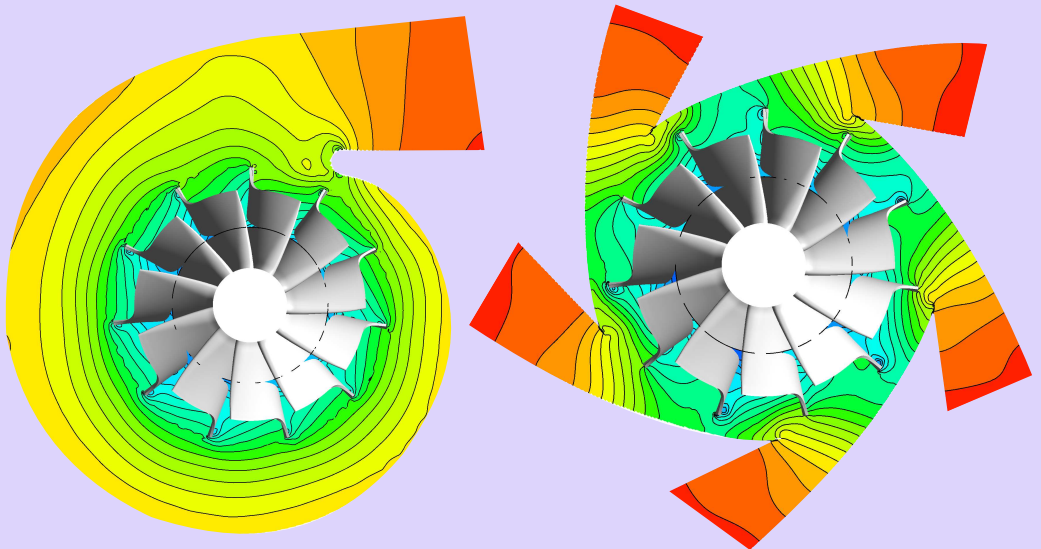


# Novel Concept for the Control and Operation of Radial Turbine

Ahmed Farid Ayad Hassan





# **Novel Concept for the Control and Operation of Radial Turbine**

Von der Fakultät Energie-, Verfahrens- und Biotechnik  
der Universität Stuttgart zur Erlangung der Würde eines Doktors  
der Ingenieurwissenschaften (Dr.-Ing.) genehmigte Abhandlung

Vorgelegt von

**Ahmed Farid Saad Ayad Hassan**

aus Kairo, Ägypten

Hauptberichter: Prof. Tekn. Dr. Damian M. Vogt

Mitberichter: Prof. Dr.-Ing. Markus Schatz

Tag der mündlichen Prüfung: 06. 07. 2022

Institut für Thermische Strömungsmaschinen  
und Maschinenlaboratorium der Universität Stuttgart

2023



**D 93 (Diss. Universität Stuttgart)**

**Copyright © 2023 Ahmed Farid Ayad Hassan.**

All rights reserved. No part of this publication may be reproduced, stored in a retrieval system, or transmitted, in any form or by any means, electronic, mechanical, photocopying, recording, or otherwise, without the prior permission of the author.

Ahmed Farid Ayad Hassan,

e-mail: [a.farid@mtc.edu.eg](mailto:a.farid@mtc.edu.eg) · <https://orcid.org/0000-0002-3321-7113>



# Acknowledgements

First and foremost I am extremely grateful to my supervisors, Prof. Tekn. Dr. Damian M. Vogt and Prof. Dr.-Ing. Markus Schatz for their invaluable advices, continuous support, and patience during my Ph.D. study. Their immense knowledge and plentiful experience have encouraged me in all the time of my academic research and daily life.

I would like to thank all my colleagues at ITSM. It is their kind help and support that have made my study and life in Germany a wonderful time. A special thank goes to Michaela Beierl, Jennifer Blackburne, Tobias Müller, and Nikola Kovachev for the nice time we spent in our office. A special "thank you" to everyone who helped me to learn and practice the German language.

I'm extremely grateful to all the organizers of my oral exam events especially Astrid Howard, Michaela Beierl, Arthur Zobel, Simon Hummel, Nikola Kovachev, Maximilian Bauer, and Christopher Fuhrer. It was really a great day and I won't forget it.

I would like to express my deepest appreciation to Prof. Mahmoud Yhea and Mr. Nikola Kovachev for proofreading and improving the manuscript of the thesis, and Mr. Fabian Müller for his support and help in my experimental study.

I also like to thank the Egyptian government represented in the ministry of defense for funding my study and keep supporting me until the end. Also to thank all my colleagues at the Military Technical College for supporting me during the last years and contributing to this work especially Prof. Hammed Abdalla who supported me since the beginning of my academic career.

Finally, I would like to express my gratitude to my parents, my brothers and sisters, my wife, and my children. Without their tremendous understanding and encouragement over the past few years, it would be impossible for me to complete my study.

**Ahmed Farid Ayad Hassan**  
*Stuttgart 2022*





# Abstract

Radial turbines have proven their capability in many applications, due to their ability to operate at high-pressure ratios, structure robustness, and inherent cost advantages compared to the axial turbine. Controlling their performance allows efficient operation, even when operating at off-design conditions. Various control concepts are used for this purpose. These concepts depend mainly on movable parts and complicated control mechanisms, which limits radial turbines usability in some applications. Hence the need rises for a new control concept based entirely on fixed parts.

Responding to these requirements, the Institute of Thermal Turbomachinery and Machinery Laboratory (ITSM) at the University of Stuttgart started a research project which aims to build and test a new control concept for radial turbines. The idea behind this concept is to replace the traditional spiral casing with a new casing. This casing consists of multiple channels which divided the rotor inlet circumferentially to many sectors. Each channel is connected to control valves. Opening and closing these valves will control the turbine inlet area and the operating mass flow by applying different partial admission configurations. The main advantage of this new concept is that it is based only on fixed geometry, and the control valves could be placed away upstream of the turbine. Therefore the turbine can operate under control in any application requiring higher temperature ranges and smaller turbine size.

Among various radial turbine applications, turbocharger has been chosen to apply and test the new control concept. In turbocharger application, matching between the radial turbine and the Internal Combustion Engine (ICE) is a complicated balance of many design parameters. Therefore it requires a control mechanism to adjust the turbine mass flow for different ICE operating regimes and achieve an efficient operation. Thus, it was chosen for this task due to its sensitivity toward the control aspects.

The first assignment of this study is to build a design tool in order to apply the new control concept by designing Multi-channel Casing (MC) for the radial turbine. This casing will replace the traditional spiral casing and

provide a mass flow characteristic comparable to that of the original turbine design at acceptable operating efficiency. Moreover, this design tool will be tested experimentally for a selected case to ensure the design requirements. After achieving the design requirements, different partial admission configurations will be applied to control the turbine performance. The second assignment is to study the effect of the casing replacement on many radial turbine design aspects such as performance, blade excitation and aerodynamic damping at full and different partial admissions conditions.

The thesis delivers a MC design model that is capable of replacing the spiral casing with an MC and ensuring comparable mass flow characteristics. It proves also that using the MC design can enhance the radial turbine operating efficiency by 1 up to 3 percent compared to the traditional spiral casing under some design considerations.

The results illustrate also the effect of using the MC on the turbine performance and blade vibration during full and partial admission. They explain the reason behind the efficiency drop during the partial admission which is attributed mainly to the flow deviation due to the pressure difference between open and closed channels. They show also how selecting the channel count and building the excitation map for different admission configurations is crucial to avoid high blade vibration amplitude and High Cyclic Fatigue (HCF) during the turbine operation.

# Kurzfassung

Radialturbinen haben ihre Leistungsfähigkeit in vielen Anwendungen bewiesen, nicht zuletzt aufgrund ihrer Fähigkeit bei hohen Druckverhältnissen zu arbeiten, robuster Bauart und inhärenten Kostenvorteilen im Vergleich zu Axialturbinen. Die Steuerung ihrer Leistung ermöglicht einen effizienten Betrieb, selbst wenn sie unter Bedingungen außerhalb des Designpunkts betrieben werden. Dazu werden verschiedene Steuerungskonzepte verwendet. Diese Konzepte hängen hauptsächlich von beweglichen Teilen und komplizierten Steuermechanismen ab, was die Verwendbarkeit von Radialturbinen in einigen Anwendungen einschränkt. Daraus ergibt sich die Notwendigkeit für ein neues Steuerungskonzept, das vollständig auf festen Teilen basiert.

Als Antwort auf diese Anforderungen hat das Institut für Thermische Strömungsmaschinen und Maschinenlaboratorium (ITSM) der Universität Stuttgart ein Forschungsprojekt gestartet, das den Aufbau und die Erprobung eines neuen Regelungskonzepts für Radialturbinen zum Ziel hat. Die Idee hinter diesem Konzept ist, das traditionelle Spiralgehäuse durch ein neues Gehäuse zu ersetzen. Dieses Gehäuse besteht aus mehreren Kanälen, die den Rotoreinlass über den Umfang in viele Sektoren aufteilen. Jeder Kanal ist dabei mit Steuerventilen verbunden. Das Öffnen und Schließen dieser Ventile steuert die Turbineneinlassfläche und den Betriebsmassenstrom durch Anwenden verschiedener Teilbeaufschlagungskonfigurationen. Der Hauptvorteil dieses neuen Konzepts besteht darin, dass es nur auf einer festen Geometrie basiert und die Steuerventile weiter stromaufwärts von der Turbine platziert werden können. Daher kann die Turbine in jeder Anwendung kontrolliert betrieben werden, die höhere Temperaturbereiche und eine kleinere Turbinengröße erfordert.

Unter verschiedenen Radialturbinenanwendungen wurde der Turbolader ausgewählt, um das neue Steuerungskonzept anzuwenden und zu testen. Bei Turboladeranwendungen ist die Abstimmung zwischen der Radialturbinen- und dem Verbrennungsmotor ein kompliziertes Gleichgewicht vieler Konstruktionsparameter. Daher ist ein Steuermechanismus erforderlich, um den Turbinenmassenstrom für verschiedene Betriebsbereiche des Verbren-

nungsmotors anzupassen und einen effizienten Betrieb zu gewährleisten. Aufgrund seiner Sensitivität gegenüber den Steuerungsaspekten wurde dieser für die Aufgabe ausgewählt.

Die erste Aufgabe der vorliegenden Studie besteht darin, ein Konstruktionswerkzeug aufzubauen, um das neue Steuerungskonzept anzuwenden, indem ein Mehrkanalgehäuse für die Radialturbine entworfen wird. Dieses Gehäuse wird das herkömmliche Spiralgehäuse ersetzen und bei akzeptabler Betriebseffizienz eine Massendurchflusscharakteristik bereitstellen, die mit der des ursprünglichen Turbinendesigns vergleichbar ist. Darüber hinaus wird dieses Designtool experimentell für einen ausgewählten Fall getestet, um die Designanforderungen sicherzustellen. Nach Erreichen der Auslegungsanforderungen werden verschiedene Teilbeaufschlagungskonfigurationen angewendet, um die Turbinenleistung zu steuern. Die zweite Aufgabe besteht darin, die Auswirkung des Gehäuseaustauschs auf viele Designaspekte von Radialturbinen wie Leistung, Schaufelanregung und aerodynamische Dämpfung bei Voll- und verschiedenen Teilbeaufschlagungsbedingungen zu untersuchen.

Die Dissertation liefert ein Modell zur Auslegung von Mehrkanalgehäusen, das in der Lage ist, das Spiralgehäuse durch ein Mehrkanalgehäuse zu ersetzen und vergleichbare Massenstromeigenschaften zu gewährleisten. Es beweist auch, dass die Verwendung des Mehrkanalgehäuses den Betriebswirkungsgrad der Radialturbine im Vergleich zum herkömmlichen Spiralgehäuse unter bestimmten Designaspekten um 1 bis 3 Prozent verbessern kann.

Die Ergebnisse veranschaulichen auch die Auswirkungen der Verwendung des Mehrkanalgehäuses auf die Turbinenleistung und die Schaufelschwingungen während der vollständigen und teilweisen Beaufschlagung. Sie erklären den Grund für den Wirkungsgradabfall während der Teilbeaufschlagung, der hauptsächlich auf die Strömungsumlenkung aufgrund des Druckunterschieds zwischen offenen und geschlossenen Kanälen zurückzuführen ist. Sie zeigen auch, wie entscheidend die Auswahl der Kanalanzahl und die Bewertung der Anregung für verschiedene Einlasskonfigurationen ist, um eine hohe Schaufelschwingungsamplitude und hohe Lastwechselfrequenzen während des Turbinenbetriebs zu vermeiden.

# Table of Contents

<b>Acknowledgements</b>	<b>iii</b>
<b>Abstract</b>	<b>v</b>
<b>kurzfassung</b>	<b>vii</b>
<b>Table of Contents</b>	<b>ix</b>
<b>List of Figures</b>	<b>xiii</b>
<b>List of Tables</b>	<b>xix</b>
<b>Nomenclature</b>	<b>xxi</b>
<b>1 Introduction</b>	<b>1</b>
1.1 Motivation . . . . .	1
1.2 Thesis aim . . . . .	4
1.3 Thesis structure . . . . .	5
<b>2 Basics and Definitions</b>	<b>7</b>
2.1 Radial Turbine . . . . .	7
2.1.1 Basic Principles . . . . .	7
2.1.2 Thermodynamic Characteristics . . . . .	9
2.1.3 Losses . . . . .	12
2.1.4 Applications . . . . .	13
2.2 Turbocharger . . . . .	13
2.2.1 Turbine performance . . . . .	14

2.2.2	Compressor performance . . . . .	16
2.2.3	Power Balance . . . . .	17
2.2.4	Matching of turbochargers . . . . .	18
2.3	Radial Turbine Design Aspects . . . . .	20
2.3.1	Static Loads . . . . .	20
2.3.2	Dynamic Loads . . . . .	20
2.3.3	Structural Dynamics . . . . .	21
2.3.4	Resonance Crossings . . . . .	23
2.3.5	Excitation Forces . . . . .	24
2.3.6	Damping . . . . .	26
2.4	Computational Fluid Dynamics . . . . .	26
<b>3</b>	<b>State-of-the-art of RT Operation Control</b>	<b>31</b>
3.1	Wastegate . . . . .	31
3.1.1	Function . . . . .	31
3.1.2	Classifications . . . . .	32
3.2	Variable Geometry Turbine . . . . .	34
<b>4</b>	<b>Multi-channel Casing Design</b>	<b>39</b>
4.1	Definitions . . . . .	39
4.2	Design parameters . . . . .	40
4.3	Test case . . . . .	42
4.4	Parametric study . . . . .	43
4.4.1	Channel Count . . . . .	43
4.4.2	Channel Outlet Diameter . . . . .	46
4.4.3	Other Geometrical parameters . . . . .	49
4.5	Spiral casing replacement . . . . .	52

---

<b>5</b>	<b>Experimental Work</b>	<b>57</b>
5.1	Test Setup . . . . .	57
5.1.1	Test Rig . . . . .	57
5.1.2	Turbine casing installation . . . . .	58
5.2	Technical Measurements . . . . .	60
5.2.1	Turbine performance measurements . . . . .	61
5.2.2	Blade vibration measurements . . . . .	63
5.3	Turbine Performance . . . . .	64
5.4	Blade Vibration . . . . .	73
<b>6</b>	<b>Numerical Study</b>	<b>81</b>
6.1	Fluid Model . . . . .	82
6.1.1	Boundary Condition . . . . .	84
6.1.2	Domains Grid and Sensitivity Study . . . . .	84
6.1.3	Unsteady simulation . . . . .	87
6.1.4	CFD Model Results and Validation . . . . .	87
6.2	Structural Model . . . . .	92
6.3	Fluid Structure Interaction . . . . .	97
6.3.1	Aerodynamic Excitation . . . . .	97
6.3.2	Aerodynamic Damping . . . . .	98
6.3.3	Forced response analysis . . . . .	99
<b>7</b>	<b>Effect of Multi-channel Casing on Turbine Performance</b>	<b>101</b>
7.1	Performance and Flow Analysis . . . . .	101
7.2	Loss Mechanisms . . . . .	105
<b>8</b>	<b>Effect of Multi-channel casing on Blade Vibration</b>	<b>113</b>
8.1	Aerodynamic Excitation . . . . .	113
8.2	Aerodynamic Damping . . . . .	118
8.3	Forced Response Analysis . . . . .	125

<b>9</b>	<b>Conclusions and Future Work</b>	<b>129</b>
9.1	Multi-channel Casing Design . . . . .	129
9.2	Effect of MC on the Turbine Performance . . . . .	130
9.3	Effect of MC on the Blade Vibration . . . . .	131
9.4	Future Work . . . . .	131
	<b>References</b>	<b>133</b>
<b>A</b>	<b>Geometrical Relations</b>	<b>141</b>
A.1	Throat Area (Equation 4.1) . . . . .	141
A.2	Inlet Area . . . . .	143
A.3	Inlet tube angles and diameter . . . . .	146
<b>B</b>	<b>Detail Drawing</b>	<b>149</b>



# List of Figures

1.1	Variable Turbine Geometry, (a) Sliding ring mechanism (b) Pivoting inlet vane (c) Movable wall volute [20]. . . . .	2
1.2	Radial turbine featuring: (a) spiral casing (b) Multi-channel casing . . . . .	3
2.1	Radial turbine components and flow directions . . . . .	8
2.2	Variation of total-to-static efficiency for a different stator exit flow angles (adapted from Rohlik 1968) [65] . . . . .	10
2.3	h-s diagram for radial inflow turbine featuring MC . . . . .	11
2.4	Loss distribution along the maximum static efficiency (adapted from Rohlik 1968) [65] . . . . .	13
2.5	Construction of Turbocharger [68] . . . . .	14
2.6	Radial turbine performance map . . . . .	15
2.7	Compressor performance map . . . . .	16
2.8	Turbine and compressor pressure ratios relation . . . . .	18
2.9	Matching procedure of a conventional turbocharger with fixed geometry turbochargers . . . . .	19
2.10	Haigh Diagram . . . . .	21
2.11	Beam mode-shapes . . . . .	22
2.12	Disk mode-shapes . . . . .	22
2.13	ZZENF diagram . . . . .	23
2.14	Excitation mechanisms in RT featuring MC . . . . .	25
2.15	Static pressure perturbation due to blade vibration . . . . .	27
2.16	Law of the wall, flow between two parallel plates . . . . .	30

3.1	Turbocharger featuring wastegate schematic drawing . . . . .	32
3.2	Turbocharger matching map for wastegate . . . . .	33
3.3	Schematic of the VAT (a) and VNT (b) control mechanisms . . .	34
3.4	Turbine performance for VTG and FTG (adapted from Capobianco and Gambarotta [9]) . . . . .	35
3.5	Optimum efficiency for VGT and FTG (adapted from Capobianco and Gambarotta [9]) . . . . .	36
3.6	Turbocharger matching map for VGT . . . . .	37
4.1	Multi-channel casing geometrical parameters . . . . .	39
4.2	Multi-channel casing geometrical parameters . . . . .	40
4.3	Multi-channel casing throat cross-section area . . . . .	41
4.4	Turbine rotor . . . . .	42
4.5	Effect of channel count on the turbine performance . . . . .	44
4.6	Radial velocity component at rotor inlet . . . . .	44
4.7	Relation between throat area and flow circulation for different $N_{ch}$ . . . . .	45
4.8	Turbine performance for different $N_{ch}$ . . . . .	46
4.9	Absolute velocity angle ( $\alpha$ ) contours: (left) rotor inlet, (right) casing outlet . . . . .	47
4.10	Effect of the channel outlet diameter on the turbine performance	47
4.11	Effect of the channel outlet diameter on the flow direction, Top: Velocity triangle at rotor inlet. Bottom: Streamlines at rotor mid span. . . . .	48
4.12	Effect of the channel outlet diameter on the turbine performance, at comparable mass flow rate . . . . .	49
4.13	Effect of the channel outlet angle on the turbine performance for different casing area ratios . . . . .	51
4.14	Effect of the channel area ratio on the turbine performance for different casing outlet angles . . . . .	52
4.15	Effect of the channel outlet angle on the turbine performance, for different casing inlet diameters . . . . .	54

---

4.16	Effect of the channel Inlet diameter on the turbine performance, for different outlet angle . . . . .	54
4.17	MC casing replacement procedures . . . . .	55
5.1	Hot gas test rig schematic drawing . . . . .	57
5.2	Turbine MC with 5 channels, Top: half section view - Bottom: Exploded view. . . . .	59
5.3	Flow distributor (Exploded view) . . . . .	60
5.4	Radial turbinate installation in test rig . . . . .	61
5.5	Pressure and temperature sensors locations . . . . .	62
5.6	BTT sensor position, left: Circumferential - Right: Axial . . . . .	64
5.7	Multi-channel casing unified symbol . . . . .	65
5.8	Turbine reduced mass flow rate at different inlet temperature, MC5-100 . . . . .	67
5.9	Turbine efficiency at different inlet temperature, MC5-100 . . . . .	67
5.10	Turbine reduced mass flow rate at different admission percentage, T=300K . . . . .	68
5.11	Turbine efficiency at different admission percentage, T=300K . . . . .	68
5.12	Turbine reduced mass flow rate at different admission percentage, T=783K . . . . .	69
5.13	Turbine efficiency at different admission percentage, T=783K . . . . .	69
5.14	Turbocharger compressor map . . . . .	70
5.15	Turbocharger compressor isentropic efficiency . . . . .	70
5.16	Mass flow measurement repeatability for selected rotational speed and admission percentage . . . . .	71
5.17	Efficiency measurement repeatability for selected rotational speed and admission percentage . . . . .	71
5.18	Turbine reduced mass flow rate for different casing types, Full admission . . . . .	72
5.19	Turbine isentropic efficiency for different casing types, Full admission . . . . .	73
5.20	Speed ramp for different admission configurations, EO6 . . . . .	74

5.21 Blade vibration amplitude, EO6 . . . . .	75
5.22 Blade vibration amplitude, EO7 . . . . .	76
5.23 Blade vibration amplitude, EO8 . . . . .	77
5.24 Blade vibration data for different EOs and admission configurations . . . . .	78
6.1 MC casing design and assessment process . . . . .	81
6.2 Radial turbine featuring five channel casing CFD domains . . . . .	82
6.3 CFD domains main metrics . . . . .	83
6.4 CFD domains mesh, one-sector model . . . . .	85
6.5 MC CFD domains mesh topology at meridional plan . . . . .	86
6.6 Mass flow rate and efficiency for different mesh size, CFD steady . . . . .	87
6.7 pressure amplitude for different time step, CFD unsteady . . . . .	88
6.8 Turbine mass flow characteristics for different admission configuration, CFD steady and test data, five-channels casing . . . . .	89
6.9 Static pressure at turbine stage mid-span for different casing types, transient simulation . . . . .	90
6.10 Time-averaged static pressure at blade surface for different casing types . . . . .	91
6.11 Time-averaged blade loading for different casing types, mid-span . . . . .	92
6.12 Unsteady pressure at different monitor points for different casings, 90% span . . . . .	93
6.13 Unsteady pressure ant its harmonic spectrum for different casings . . . . .	94
6.14 Investigated turbine rotor . . . . .	95
6.15 FE model of a turbine wheel . . . . .	95
6.16 Turbine rotor Campbell diagram . . . . .	96
6.17 ZZNF diagram . . . . .	96
6.18 Different nodal diameter for resonance crossing, first bending mode . . . . .	97

---

7.1	Effect of the admission percentage (top) and rotational speed (bottom) on the turbine efficiency at BEP, four-channel casing, steady simulation . . . . .	102
7.2	Effect of the admission percentage (top) and rotational speed (bottom) on the turbine efficiency at BEP, four-channel casing, unsteady simulation . . . . .	103
7.3	Static pressure contour at rotor mid-span at a specific instance for different admission percentage . . . . .	104
7.4	Blade torque for different admission configurations . . . . .	105
7.5	Entropy generation rate contour at rotor mid-span for different admission percentage . . . . .	107
7.6	EGR contour and normalized relative velocity at zone (A) . . . .	108
7.7	EGR contour at casing mid-span for different admission percentage . . . . .	110
7.8	EGR contour and normalized relative velocity at casing mid-span, MC4-75 . . . . .	111
7.9	Entropy increase in different turbine domains, for different admission configurations . . . . .	111
7.10	EGR contour and normalized relative velocity for different radial gap, MC4-50b . . . . .	112
7.11	Entropy increase for different radial gap, MC4-50b . . . . .	112
8.1	FSI Simulation Results at EO6, different admission configuration	114
8.2	Generalized force convergence, EO6 . . . . .	115
8.3	Generalized Force (GF) compared to vibration test data, different admission configuration . . . . .	116
8.4	FSI Simulation Results at EO8 for different casing type, Full admission . . . . .	117
8.5	Generalized force for different casing types and admission configurations, EO8 . . . . .	118
8.6	CFD domains for aerodynamic damping calculation: (a) Full model (b) Isolated rotor model . . . . .	119
8.7	Transient averaged blade loading at 50% span . . . . .	120

---

8.8	Top: Blade pressure for a complete revolution. Bottom: Pressure perturbation due to the blade vibration, MC4-100 at the blade tip . . . . .	121
8.9	Wall power density and the work per cycle for a rotor blade, MC4-100 . . . . .	122
8.10	Wall power density and work per cycle for MC different admission configuration, full model . . . . .	124
8.11	Damping ratios for different MC admission configurations. . . . .	125
8.12	Blade tip displacement for different admission configuration, EO6 . . . . .	126
8.13	First bending mode at blade tip, scale 100:1 . . . . .	126
8.14	Haigh diagram for different admission configuration, EO6 . . . . .	127
8.15	Dynamic stresses contour for different admission configuration, EO6 . . . . .	127
8.16	FRA tangential vibration amplitude validation . . . . .	128

# List of Tables

4.1	Multi-channel casing design parameters . . . . .	41
4.2	Geometrical parameters for the first group of selected cases . .	50
4.3	Geometrical parameters for the second group of selected cases	53
5.1	Test rig specifications [32] . . . . .	58
5.2	MC different admission percentage and configuration . . . . .	65
5.3	Blade vibration data (Median values) . . . . .	79
6.1	MC mesh element count . . . . .	84





# Nomenclature

<b>Symbol</b>	<b>Description</b>	<b>Unit</b>
$A$	Area	[m <sup>2</sup> ]
$atstep$	Accumulated Time Step	[-]
$C$	Absolute velocity component	[m/s]
$D$	Diameter	[m]
$F$	Force	[N]
$f$	Frequency	[Hz]
$h$	Specific enthalpy	[J/kg.K]
$k$	Turbulent kinetic energy	[J/kg]
$\dot{m}$	Mass flow rate	[kg/s]
$N$	Rotational speed	[rpm]
$N_{ch}$	Channel count	[-]
$N_s$	Specific speed number	[rpm/(ft <sup>3/4</sup> )(s <sup>1/2</sup> )]
$n$	Harmonic index	[-]
$\vec{n}$	Surface normal unit vector	[-]
$p$	Pressure	[Pa]
$\dot{S}$	Entropy generation rate	[J/s.K]
$Q$	Volumetric flow rate	[m <sup>3</sup> /s]
$SF$	Scaling factor	[-]
$ssp$	Number of Step per Period	[-]
$t$	Time	[sec]
$T$	Total time for one blade vibration cycle	[sec]
$T$	Temperature	[K]
$U$	Base velocity component	[m/s]
$u$	Velocity in x-direction	[m/s]
$V$	Volume	[m <sup>3</sup> ]
$\dot{V}$	Volumetric flow rate	[m <sup>3</sup> /s]
$v$	Velocity in y-direction	[m/s]
$\vec{v}$	Velocity vector	[m/s]

---

$w$	Velocity in z-direction	[m/s]
$w$	Specific work	[J/kg]
$W$	Work	[J]
$W$	Relative Velocity	[m/s]
$x$	displacement in x-direction	[m]
$y$	displacement in y-direction	[m]
$z$	displacement in z-direction	[m]
$Z$	Blade count	[-]

### Greek Symbols

$\alpha$	Absolute velocity angle	[deg]
$\alpha$	Empirical constant	[m <sup>3</sup> ]
$\beta$	Relative velocity angle	[deg]
$\gamma$	Casing hub inclination angle	[deg]
$\delta$	Casing opening angle	[deg]
$\theta$	Casing wall angle	[deg]
$\lambda$	Thermal diffusivity	[m <sup>2</sup> /s]
$\pi$	Pressure ratio	[ ]
$\rho$	Density	[kg/m <sup>3</sup> ]
$\sigma$	Stress	[Pa]
$\vec{\Phi}$	Nodal displacement vector	[m]
$\Omega$	Angular frequency or speed	[rad/s]
$\omega$	The specific turbulence dissipation or turbulence frequency	[1/s]
$\eta$	Efficiency	[-]

### Superscripts

$c$	Compressor
$e$	Internal Combustion Engine (ICE)
$t$	Turbine
$tc$	Turbocharger

## Subscripts

0	Initial time step
1	Turbine Casing inlet
2	Turbine casing outlet
$2r$	Turbine rotor Inlet
3	Turbine Rotor outlet
$eff$	Effective
$a$	Alternating
$f$	Fatigue
$fix$	Fixed blade simulation
$full$	Full 3D model for turbine stage
$gen$	Generalized
$i$	Nodal index
$i$	Imaginary
$in$	at Inlet
$iso$	Isolated rotor model
$L$	Left
$m$	Mean
$max$	Maximum
$min$	Minimum
$n$	Harmonic property at index $n$
$out$	at Outlet
$r$	Right
$r$	Radial component
$red$	Reduced
$s$	Static
$sw$	Swept
$S$	Isentropic
$sg$	Single
$t$	Total flow condition
$T$	Thermal diffusion
$th$	Throat
$t - t$	Total-to-total
$t - s$	Total-to-static
$u$	Ultimate

<i>u</i>	Circumferential component
<i>v</i>	Viscous dissipation
<i>vol</i>	Volumetric
<i>vib</i>	Vibrating blade model
<i>y</i>	Yield

## Abbreviations

<i>BC</i>	Boundary Condition
<i>BEP</i>	Best Efficiency Point
<i>BL</i>	Blade loading
<i>Bl</i>	Blade
<i>BM</i>	Bending Mode
<i>BMEP</i>	Brake Mean Effective Pressure
<i>BTW</i>	Backward Traveling Wave
<i>CFD</i>	Computational Fluid Dynamics
<i>CCH</i>	Combustion Chamber
<i>EGR</i>	Entropy Generation Rate
<i>EO</i>	Engine Order
<i>FE</i>	Finite Element
<i>FRA</i>	Forced Responce Analysis
<i>FTW</i>	Forward Traveling Wave
<i>HCF</i>	High Cyclic Fatigue
<i>ICE</i>	Internal Combustion Engine
<i>ITSM</i>	Institute of Thermal Turbomachinery and Machinery Laboratory
<i>GF</i>	Generalized Force
<i>GP</i>	Generalized Pressure
<i>LE</i>	Leading-Edge
<i>M</i>	Mode shape
<i>MC</i>	Multi-channel Casing
<i>ND</i>	Nodal Diameter
<i>PA</i>	Partial Admission
<i>PS</i>	Pressure Side
<i>RT</i>	Radial Turbine
<i>SS</i>	Suction Side

<i>TE</i>	Trailing-Edge
<i>VTG</i>	Variable Turbine Geometry
<i>WPD</i>	Work Power Density

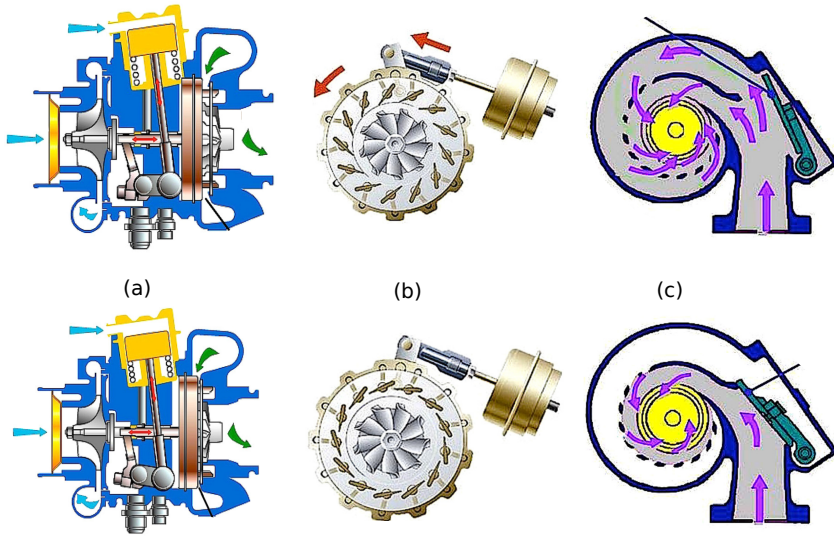


# 1 Introduction

## 1.1 Motivation

Controlling radial turbine during its operation can enhance the working efficiency mainly during the off-design operating conditions. One of the examples of how important controlling the radial turbine is the turbocharger and its application in downsizing the Internal Combustion Engine (ICE). Matching between the turbine and the compressor onto the ICE requires a control mechanism for the radial turbine to operate it at a wide mass flow range with acceptable response time as discussed by Cleni et al. and Glahn et al. [15, 27]. All the currently used control techniques which provide efficient operation are based on movable parts and complicated control mechanisms. It is known as Variable Turbine Geometry (VTG). Feneley et al. and Tang et al. [20, 74] have summarized and explained the operation of almost all the used VTG and its role in controlling the radial turbine to match it with the compressor in the turbochargers application. Examples of the VTG are sliding ring turbine mechanism, pivoting inlet vane, movable wall volute as shown in Figure 1.1.

The VTG still has a limitation at high exhaust gas temperatures due to thermo-mechanical concerns [63] and consequently, it has limited use for downsized engines, as exhaust gas temperatures increase with increasing brake mean effective pressure (BMEP) [71]. Most of these engines types depend mainly on the wastegate valve in order to limit the maximum boosting pressure. Capobianco et al. [9, 10] discussed in detail the performance of a radial turbine featuring a wastegate valve. Although the wastegate technique is widely used, it still does not provide the best performance for the radial turbine in zones of application where the VTG has a limitations. It wastes part of the energy by bypassing part of the exhaust gases without energy extraction. Therefore, the need for a novel control system rises. It should be based completely on fixed geometry to avoid the drawbacks of the previously mentioned control system.

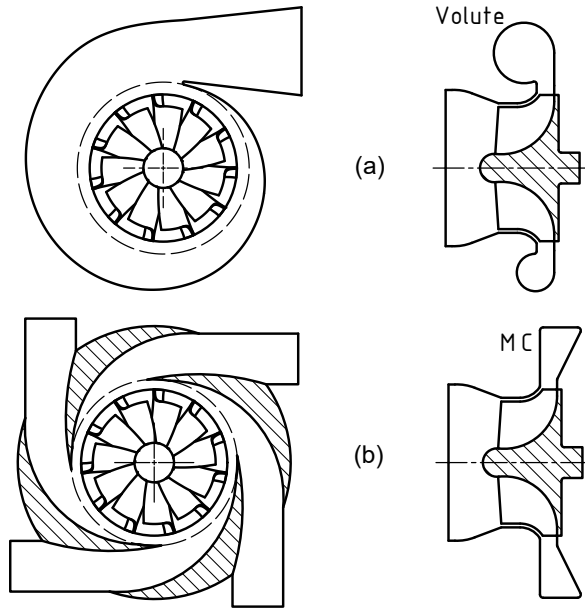


**Figure 1.1:** Variable Turbine Geometry, (a) Sliding ring mechanism (b) Pivoting inlet vane (c) Movable wall volute [20].

In response to these needs, the institute of thermal turbomachinery and machinery laboratory (ITSM) at the University of Stuttgart is researching on replacing the traditional spiral volute with a Multi-channel Casing (MC) as shown in Figure 1.2. The idea behind using this type of casing is to divide the turbine rotor inlet circumferentially into many divisions based on certain number of channels. This division can be opened or closed by means of control valves to control the turbine inlet area and consequently provide mass flow controllability. The MC control concept has advantages compared to the VTG as it is based on a fixed geometry and the control valves could be placed an appropriate upstream distance from the turbine rotor. These advantages will help the new control concept to exist in a wider range of applications beside giving it more design flexibility and reliability.

Firstly, the idea of connecting a turbocharger featuring a MC turbine to an IC engine was investigated by Challand et al. [14] after registering the idea as a European patent (21326 - EP)[13]. This investigation was based on a theoretical one-dimensional model and Computational Fluid Dynamics (CFD) simulation to the MC concept and comparing its performance to the





**Figure 1.2:** Radial turbine featuring: (a) spiral casing (b) Multi-channel casing

turbocharger featuring VTG turbine. The initial conclusion from this study showed that the MC has a comparable or even better performance compared to the VTG and it predicted that the MC could provide an efficient radial turbine controllability.

Secondly, Fuhrer [24] performed a numerical parametric study to choose between many geometrical parameters to create a first prototype for the experimental tests. This study investigated the effect of the channel shape (curved and straight), adding a splitter to the channel, and some of the channel geometrical parameters on the turbine performance. Based on this investigation, a first prototype was recommended to be used in the experimental test.

Thirdly, Ilievski and Müller [36, 56] performed the experimental test for the turbine featuring the selected MC at the hot gas test stand at ITSM University of Stuttgart. The result of this test showed the performance map of the new MC concept at full and partial admission and compared it to the spiral

casing. It showed also that MC has higher swallowing capacity compared to the spiral casing. Regarding the operating efficiency, the full admission gives comparable efficiency to the spiral casing with an efficiency drop during the partial admission, especially at the lower admission percentage.

Finally, Schatz et al. [67] investigated the MC concept in real engine test rig using a four-cylinder turbocharged Direct Injection Spark Ignition (DISI) engine from the Volkswagen group. The results showed that the partial admission concept allows increasing the higher turbine expansion ratio. However, at low mass flows the efficiency drops related to partial admission were recorded.

All these investigations paved the way to understand the new concept and highlighted many questions such as: how could the use of an MC affects radial turbine design aspects such as performance, reliability, and lifetime? What are the loss mechanisms of the radial turbine featuring MC on full and partial admission operation? This study aims to build a numerical design model for the radial turbine featuring MC and answer these questions.

## **1.2 Thesis aim**

This study aims first to create a numerical design tool to produce an MC to replace the traditional spiral volute and fulfill the turbine performance requirements. This design model is based on a CFD model and aims to investigate some new parameters which have not been covered in the previous studies and compare their effects on the radial turbine with the currently used casing. To achieve reasonable comparability, the design model should provide a comparable operating mass flow rate between the MC at full admission and the spiral casing while maintaining an acceptable operating efficiency.

Secondly, this design model is validated using experimental test data for selected design cases. The experimental test takes place on the hot gas test stand at ITSM University of Stuttgart.

Thirdly, a CFD model for the MC and the spiral casing are built to study and understand the internal flow field of the new concept in comparison with the spiral casing internal flow by performing different parametric studies. The results of these studies are used to discuss many MC aspects and their effect on the performance: different channel shapes, different channel

count, different geometrical parameters, the turbine performance during the full and partial admission, and the loss mechanisms.

Finally, replacing the spiral volute with the MC affects the unsteady loading on the rotor blades and consequently the blade vibration behavior. To avoid High Cycle Fatigue (HCF) and blade failure, the aerodynamic loads and the blade vibration behavior caused by using the MC concept during full and partial admission are investigated in the last part of this study.

### **1.3 Thesis structure**

The thesis consists of nine chapters. Chapter 1 introduces the current study and addresses in detail the motivation of researching in a novel control mechanism for the radial turbine and the idea behind using MC for this purpose. It states also the history of the MC control concept and what is added to this topic during this study. Chapter 2 presents the required theoretical background to understanding the following investigations including the radial turbine and turbochargers basics and definitions. The state of the art of controlling the radial turbine is explained in Chapter 3 with focus on the most commonly used technologies such as the wastegate valve and the variable turbine geometry with rotating guide vanes. Chapter 4 explains the design model for the MC including all required equations. Following this a parametric study is conducted to understand the effect of all the geometrical parameters on the turbine performance. Chapter 5 addresses the experimental test setup which is used to validate this study. Chapter 6 presents the numerical simulation setup and its validation with the test data. Replacing the traditional spiral casing with an MC affects different radial turbine design aspects, Chapters 7 and 8 discuss the effect of this replacement on the turbine performance and the blade vibration, respectively. Finally, Chapter 9 sums up all the previous results in the conclusion section.



## **2 Basics and Definitions**

This chapter deals with the theoretical background of the present study. First, it presents the basics of a radial turbine and its applications. Then it focuses on radial turbine application on the turbocharger including many topics that are investigated in this study. Finally, it presents the governing equations which are used in the CFD model which is used to study the turbine flow.

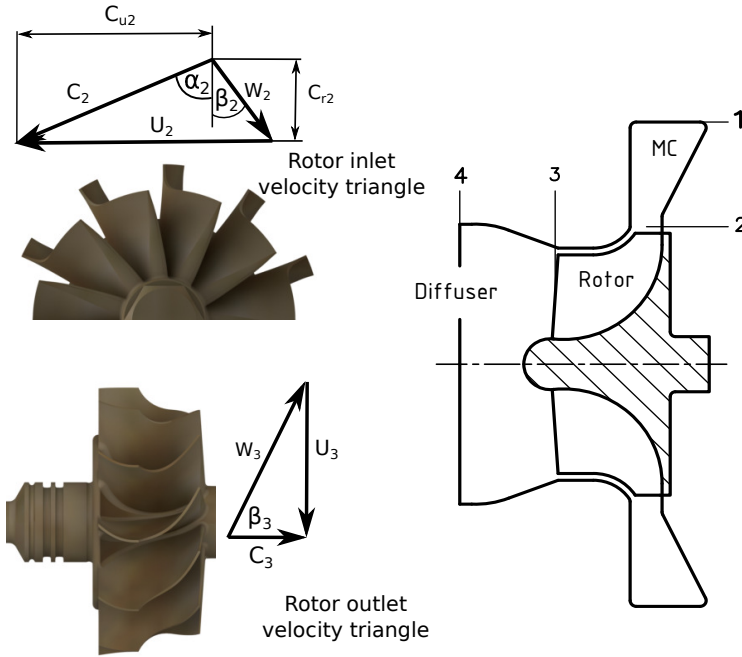
### **2.1 Radial Turbine**

The radial-inflow turbine, or inward-flow radial turbine, is a rotating machine that converts the pressure and thermal energy stored in the working fluid into kinetic energy by rotating the turbine wheel. The fluid enters the rotor radially from a larger area at its tip and leaves it axially from smaller area at the rotor eye.

The radial turbine consists mainly of a spiral volute (scroll), inlet guide vanes, a rotor and an outlet diffuser. In some cheaper applications, the inlet guide vane can be dispensed, provided that the volute executes his role in directing the flow toward the rotor inlet. Radial turbine featuring a multi-channel casing is a new design concept that replaces the spiral volute and the inlet guide vanes with the multi-channel casing. MC performs the same function of accelerating and guiding the flow before entering the rotor. Besides, it applies a turbine partial admission to control the turbine performance.

#### **2.1.1 Basic Principles**

The specific work done by the fluid on the turbine rotor can be calculated as a function of the velocity components as shown in the Euler turbomachinery equation 2.1. where station 2 represents the turbine rotor inlet and 3 represents the rotor outlet as described in Figure 2.1.



**Figure 2.1:** Radial turbine components and flow directions

$$w = U_2 C_{u2} - U_3 C_{u3} \quad (2.1)$$

A typical design case for the radial inflow turbine is characterized by a radial relative velocity at the rotor inlet ( $\beta_2 = 0$ ) and an axial absolute velocity at the rotor outlet ( $C_{u3} = 0$ ). Applying this case conditions reduces the Euler equation to simpler form as shown in Equation 2.2. Moreover, the radial inflow turbine can achieve higher work if the outlet has a negative circumferential absolute velocity component ( $C_{u3} < 0$ ). This is accompanied by an increase in kinetic exhaust losses.

$$w = U_2^2 \quad (2.2)$$

Having studied the radial turbine internal flow experimentally and numerically by means of CFD, it has been confirmed that the optimum incidence

angle which leads to the best efficient turbine operation is between  $\beta_2 = -20^\circ$  and  $\beta_2 = -40^\circ$ , which leads to a uniform flow within the rotor passage as reported by [54, 77].

In contrast to variable turbine geometry, the MC has a fixed geometry. It is designed to provide an optimum exit flow angle for both full and partial admission. Rohlik [65] performed an analytical investigation to the radial inflow turbine for different stator exit flow angles  $\alpha$  and different specific speeds  $N_s$  as described in Equation 2.3, where  $N$  is the shaft speed,  $Q$  is the volumetric flow rate, and  $\Delta h_s$  is the ideal work done by the rotor. The results of this study are presented in Figure 2.2. It shows the optimum casing exit angle between 70 and 74 deg.

$$N_s = \frac{N\sqrt{Q}}{(\Delta h_s)^{\frac{3}{4}}} \quad (2.3)$$

### 2.1.2 Thermodynamic Characteristics

The adiabatic expansion process for a radial turbine featuring an MC is presented in Figure 2.3. Station 1-2 represents the MC, 2-3 the rotor, and 3-4 the outlet diffuser. The total enthalpy across the MC is assumed to be constant,  $h_{t1} = h_{t2}$ , therefore the static enthalpy drop is calculated as:

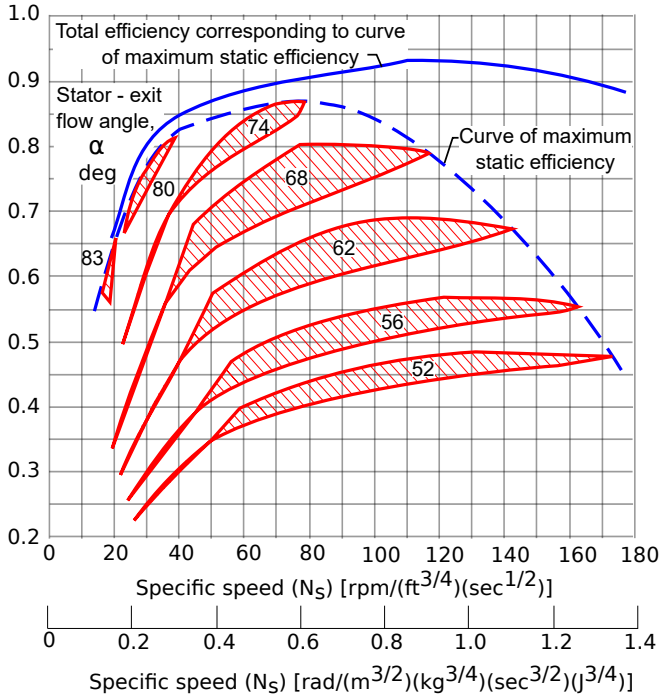
$$h_1 - h_2 = \frac{1}{2}(C_2^2 - C_1^2) \quad (2.4)$$

A drop in total pressure occurs between stations 1 and 2 that is due to friction losses. Whereas the static pressure at station 2 is lower than that at station 1 resulting in fluid acceleration across the MC.

The drop in total specific enthalpy across the rotor is equal to the specific work done by the fluid on the turbine rotor as:

$$w = h_{t2} - h_{t3} \quad (2.5)$$

The total pressure along the outlet diffuser decreases from  $p_{t3}$  to  $p_{t4}$  due to losses while the static pressure usually increases from  $p_3$  to  $p_4$  given that part of the kinetic energy from the turbine outlet flow is retrieved. Still assuming adiabatic conditions, the total enthalpy across the outlet diffuser remains constant,  $h_{t3} = h_{t4}$ , therefore the static enthalpy drop is calculated as:



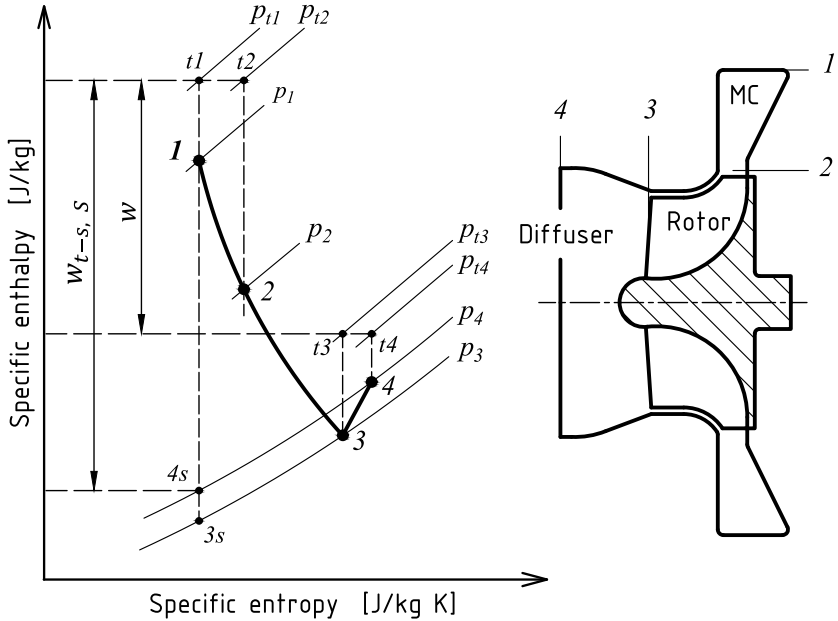
**Figure 2.2:** Variation of total-to-static efficiency for a different stator exit flow angles (adapted from Rohlik 1968) [65]

$$h_3 - h_4 = \frac{1}{2}(C_4^2 - C_3^2) \quad (2.6)$$

Radial turbine isentropic efficiency can be calculated based on two different definitions. The selection between these two different definitions depends mainly on the status of the exit kinetic energy whether it adds to the useful work or it is just a waste. In the case of useful kinetic energy, the ideal isentropic specific work and the isentropic efficiency are defined using the total-to-total definition as shown in Equations 2.7 and 2.8 respectively.

$$w_{t-t, S} = h_{t2} - h_{t4S} \quad (2.7)$$





**Figure 2.3:** h-s diagram for radial inflow turbine featuring MC

$$\eta_{t-t} = \frac{w}{w_{t-t, S}} = \frac{h_{t2} - h_{t4}}{h_{t2} - h_{t4S}} \quad (2.8)$$

In the case of non-useful kinetic energy, the total-to -static definition is used and the isentropic specific work and efficiency are calculated as shown in Equations 2.9 and 2.10 respectively.

$$w_{t-s, S} = h_{t2} - h_{s4S} \quad (2.9)$$

$$\eta_{t-s} = \frac{w}{w_{t-s, S}} = \frac{h_{t2} - h_{t4}}{h_{t2} - h_{s4S}} \quad (2.10)$$

The radial turbine degree of reaction is defined as the ratio between the static enthalpy drop across the rotor and its drop across the entire turbine stage:

$$R = \frac{h_{s2} - h_{s3}}{h_{s1} - h_{s3}} \quad (2.11)$$

### 2.1.3 Losses

The useful turbine shaft work can be calculated after subtracting the bearing and the disk friction losses from the turbine stage work. The turbine stage work is obtained from the isentropic enthalpy difference after having subtracted the aerodynamic losses, which can be described as follow:

(a) Friction and separation losses

All radial turbine components feature these types of losses to some degree which mainly depends on blade and channel geometry as well as surface quality of the wetted surfaces.

(b) Secondary flow losses

Flow circulation in various blade channels and flow phenomena related to boundary layers are the main reason for these types of losses. They depend mainly on the aerodynamic blade loading and the geometrical shape of the flow channel.

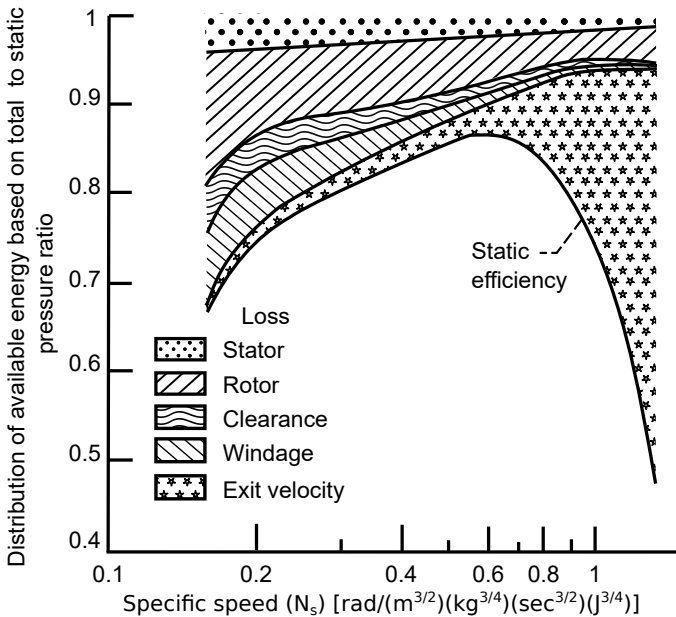
(c) Shock and incidence losses

Whereas incidence losses appear during the off-design operation, shock losses appear in case the flow velocities attain or exceed transonic levels.

(d) Tip Clearance loss

Part of the flow flows through the gap between the turbine rotor tip and the shroud casing without contributing to the useful energy transfer. This is the main reason for this loss type.

For better understanding, Figure 2.4 represents the relative contributions of the different types of losses to the maximum total-to-static isentropic efficiency at different specific speeds.



**Figure 2.4:** Loss distribution along the maximum static efficiency (adapted from Rohlik 1968) [65]

### 2.1.4 Applications

Compared to axial turbines, Inflow Radial Turbines (IRT) have an extensive range of applications by virtue of their suitability for low volume flow rates, capacity for higher pressure ratios, and their significant inherent cost advantage. For these reasons, radial turbines are still used in turbochargers for cars, buses, trucks, railway locomotives, ships, small gas turbines, rocket engine turbo-pump, diesel power generators, special steam turbines, and cryogenic and process expander.

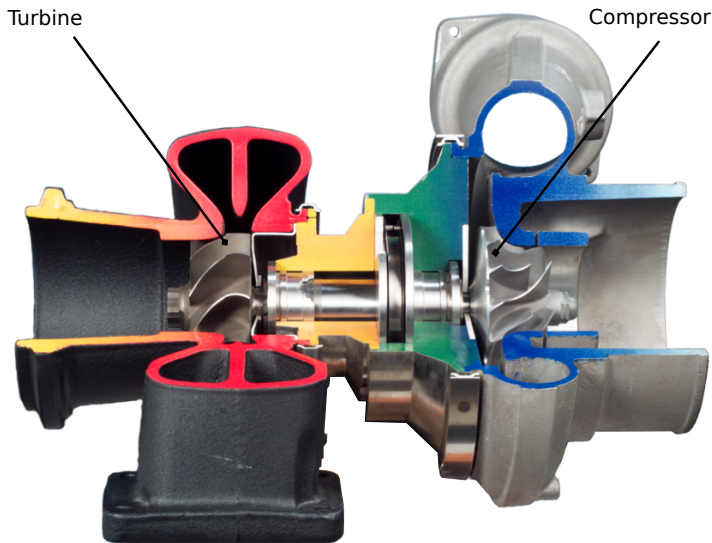
## 2.2 Turbocharger

Turbocharger is a turbomachine in which a turbine and compressor wheel are combined to increase the output power of the internal combustion

engine by making its exhaust gases contribute to this power. The main components of the turbocharger are shown in Figure 2.5.

The main objective of the turbocharger is to improve the volumetric efficiency of an ICE by boosting more air into it during the intake stroke. It can achieve this objective through the following steps:

- (a) The turbine wheel converts the pressure and thermal energy stored in the exhaust gases into kinetic energy in a shaft rotation form.
- (b) The extracted power drives the compressor wheel to compress the ambient air and increase the intake air density.

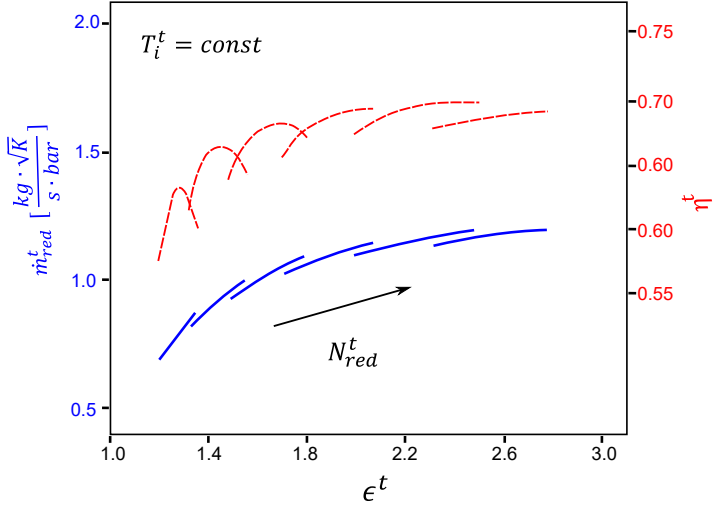


**Figure 2.5:** Construction of Turbocharger [68]

### 2.2.1 Turbine performance

The performance of radial turbine in turbocharger application is presented in terms of reduced mass flow rate and isentropic total to static efficiency for different turbine pressure ratio and rotational speed as shown in Figure 2.6.

This is based on the compressible flow analysis in turbomachinery which is explained by Dixon and Hall [17]. This analysis expressed the performance non-dimensional groups as:



**Figure 2.6:** Radial turbine performance map

$$\epsilon, \eta = f \left\{ \frac{\dot{m} \sqrt{RT_{i1}^t}}{D^2 p_{t1}^t}, \frac{ND}{\sqrt{RT_{i1}^t}}, Re, \gamma \right\} \quad (2.12)$$

For a radial turbine of a specific size, operating with a single gas at high Reynolds number, the terms  $\{D, Re, \gamma, R\}$  can be deleted from equation 2.12. Under this conditions equation 2.12 becomes:

$$\epsilon^t, \eta^t = f \left\{ \frac{\dot{m}^t \sqrt{T_{i1}^t}}{p_{t1}^t}, \frac{N^t}{\sqrt{T_{i1}^t}} \right\} = f \left\{ \dot{m}_{red}^t, N_{red}^t \right\} \quad (2.13)$$

where,  $\eta$ , turbine total to static isentropic efficiency, Equation 2.10.  $\epsilon$ , turbine total to static expansion ratio,  $\dot{m}_{red}$ , reduced mass flow rate and  $N_{red}$ , reduced rotational speed are represented, respectively, as follow:

$$\varepsilon^t = \frac{p_{t1}^t}{p_{s4}^t} \quad (2.14)$$

$$\dot{m}_{red}^t = \frac{\dot{m}^t \sqrt{T_{t1}^t}}{p_{t1}^t} \quad (2.15)$$

$$N_{red}^t = \frac{N^t}{\sqrt{T_{t1}^t}} \quad (2.16)$$

This reduction is done to eliminate the effect of different inlet conditions on the turbine performance characteristics.

## 2.2.2 Compressor performance

The compressor performance is plotted in a map represented by relating the compressor corrected mass flow ( $\dot{m}_{corr}$ ) and the isentropic efficiency ( $\eta^C$ ) to the pressure ratio ( $\pi$ ) as shown in Figure 2.7. This performance map is limited from the left side by the surge line and from the right side by the choke line.

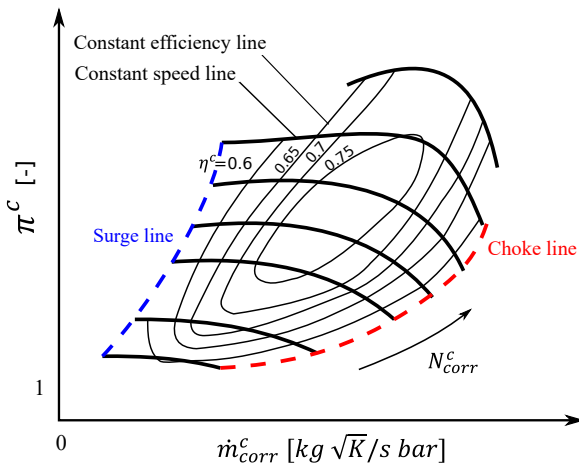


Figure 2.7: Compressor performance map

### Surge Line

Operating the compressor at high-pressure ratio and relatively low mass flow causes an air flow stall at the compressor inlet. This condition interrupts the flow discharge until a stable mass flow rate and pressure ratio are achieved. This phenomenon is accompanied by noise and is known as "surging".

### Choke Line

The highest compressor mass flow rate is limited by the compressor inlet cross-section. The mass flow rate cannot be increased when the flow speed at the rotor inlet reaches sonic velocity. This can be seen on the compressor map by drawing a choke line which connects maximum possible mass flow for different speed line.

### 2.2.3 Power Balance

In turbocharger, the radial turbine wheel and the compressor wheel are installed on the same shaft. Therefore, the compressor boost pressure ratio linked to turbine expansion ratio as derived by Nguyen [61]:

$$\pi^c = \frac{p_{out}^c}{p_{in}^c} = \left( 1 + \eta^{tc} \frac{\dot{m}^t}{\dot{m}^c} \frac{c_p^t}{c_p^c} \frac{T_{in}^t}{T_{in}^c} \left[ 1 - (\pi^t)^{\left(\frac{\gamma^t-1}{\gamma^t}\right)} \right] \right)^{\frac{\gamma^c}{(\gamma^c-1)}} \quad (2.17)$$

which can be simplified as:

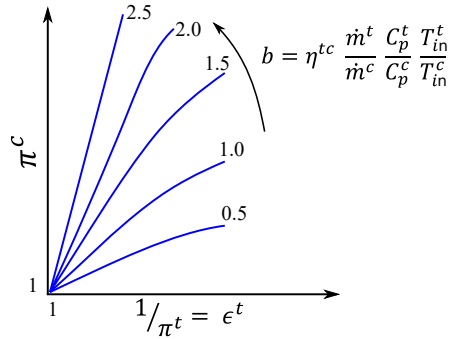
$$\pi^c = \frac{p_{out}^c}{p_{in}^c} = \left( 1 + b \left[ 1 - (\pi^t)^{\left(\frac{\gamma^t-1}{\gamma^t}\right)} \right] \right)^{\frac{\gamma^c}{(\gamma^c-1)}} \quad (2.18)$$

where b is a parameter determined mainly by the ICE exhaust temperature and the overall turbocharger efficiency ( $\eta^{tc}$ ) as follow:

$$b = \eta^{tc} \frac{\dot{m}^t}{\dot{m}^c} \frac{c_p^t}{c_p^c} \frac{T_{in}^t}{T_{in}^c} \quad (2.19)$$

where, ( $\eta^{tc}$ ) is the turbocharger overall efficiency which equal the product of turbine, compressor, and mechanical efficiency. Figure 2.8 represents the

relation between the compressor boosting and the turbine expansion ratio for different engine operating condition.



**Figure 2.8:** Turbine and compressor pressure ratios relation

## 2.2.4 Matching of turbochargers

The ICE is a positive displacement device that has operating characteristics that differ from those of rotating machinery. Therefore, matching between them is a complicated process that usually requires an iteration process. This matching process is described in Figure 2.9. It represents the matching procedures for a conventional turbocharger with fixed geometry and without a wastegate valve.

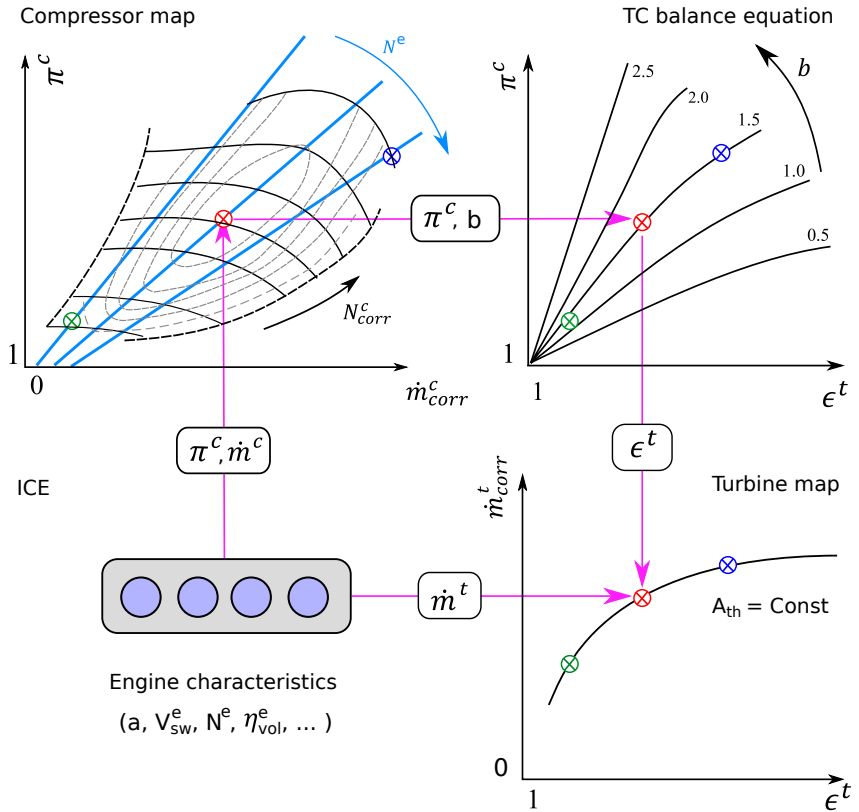
Starting from the ICE the operating point can be projected on the compressor map using the following equation [77]:

$$\pi^c = \dot{V}_{in}^c \frac{T_{out}^c}{T_{in}^c} \frac{a}{V_{sw}^e \eta_{vol}^e N^e} \quad (2.20)$$

where,  $a$  equals 1 for 2-stroke engine and 2 for 4-stroke engine.

Then the turbine expansion ratio can be calculated after calculating the parameter  $(b)$  using Equations 2.18 and 2.19. Parameter  $(b)$  depends on the TC efficiency, therefore, calculating the turbine expansion ratio might need an iterative process of calculation. The operating point then can be mapped to the turbine performance map by knowing the ICE exhaust mass flow rate.





**Figure 2.9:** Matching procedure of a conventional turbocharger with fixed geometry turbochargers

Figure 2.9 describes different operating conditions by the red, green, and blue dot which represents the TC operation at the normal, part-load, and over-load operating conditions, respectively. Assuming that all parameters in the b-param equation remained the same.

The turbine and compressor are designed to have the best efficiency operation when the ICE operates at a medium speed which is plotted on the TC matching map by the red dot.

At low ICE rotational speed, the ICE delivers low mass flow rate of the exhaust gases. These gases drive the turbine at a low expansion ratio. This results in operating the compressor at a low-efficiency and low boost region near the surge line as described by the green dot.

Operating the ICE at a high rotational speed leads to a high amount of exhaust gases which drives the turbine at a high expansion ratio. This forces the compressor to operate near the choke condition at low operating efficiency as represented by the blue dot.

## **2.3 Radial Turbine Design Aspects**

### **2.3.1 Static Loads**

During radial turbine operation, the rotor blades are exposed to static loads which cause static stresses. These stresses can be quantified by measuring the rotor deformation. Typical static stresses applied to the turbine rotor are the working fluid pressure loads, thermal loads and centrifugal loads.

### **2.3.2 Dynamic Loads**

In addition to static loads during operation, the turbine rotor is exposed to dynamic loads that may cause vibrations and alternating stresses. The main reason for such vibrations is the interaction of unsteady aerodynamic forces (both in terms of damping and excitation) and structural dynamics, which commonly is referred to as "fluid-structure interaction". The frequency of these periodic forces depends mainly on the relative motion between the rotor and stator. Based on its frequency, the blade vibration can be classified into synchronous vibration which occurs at a frequency equal to a multiple of the rotational speed or Non-Synchronous Vibration which is not related to the rotational speed.

The turbine rotor blade vibrates at resonance conditions when the frequency of the excitation force equals one of the natural frequencies of the rotor structure. This vibration can lead to serious problems such as High Cyclic Fatigue (HCF). One possibility to assess whether a component may fail due to HCF is by using a Haigh diagram as the one shown in Figure 2.10 in which stress situations at various locations are characterized by means of mean

and alternating stresses. Any combination of these stresses above the fatigue line would indicate a potentially damaging situation. The second problem is the blade flutter that can take place in case of undamped motion (i.e., negative damping coefficient).

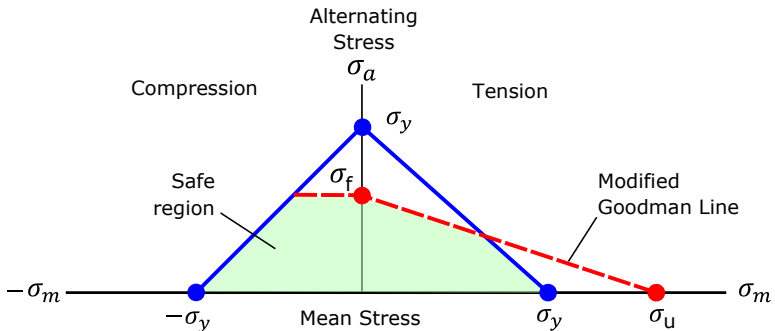


Figure 2.10: Haigh Diagram

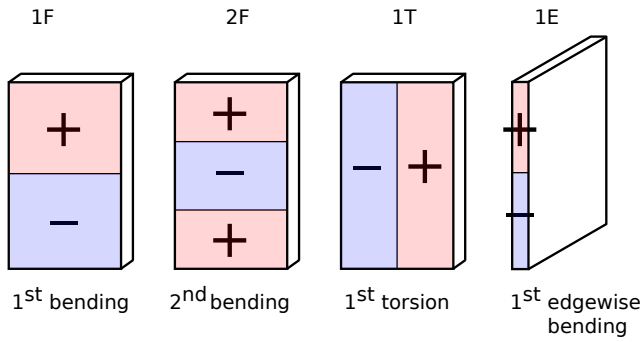
### 2.3.3 Structural Dynamics

Radial turbine wheel consists of disk and set of blades which together are known as turbine blisk. The eigen-frequencies and mode-shapes of the blisk can be determined by solving the equation of motion considering the structure mass and stiffness as shown as follow:

$$[K] - [M]\lambda = 0 \quad (2.21)$$

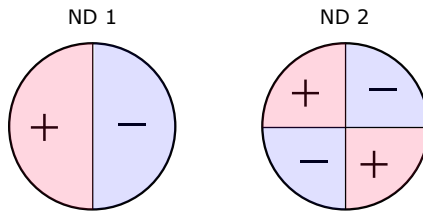
The mode-shapes of the turbine blisk are described as a combination of the blade (simple beam) and the disk mode-shapes. The blade mode-shapes are classified into bending, torsion, and edgewise bending modes depending on the inflection lines count and its orientation as shown in Figure 2.11.

Besides, the disk mode-shapes are classified based on the Nodal Diameter (ND) which refers to the number of the inflection lines across the disc diameter as shown in Figure 2.12. Blade and disk combination in the turbine blisk limits the maximum possible ND by the maximum possible



**Figure 2.11:** Beam mode-shapes

axis-symmetric division count which can be written as a function on the blades count as shown in Equation 2.22



**Figure 2.12:** Disk mode-shapes

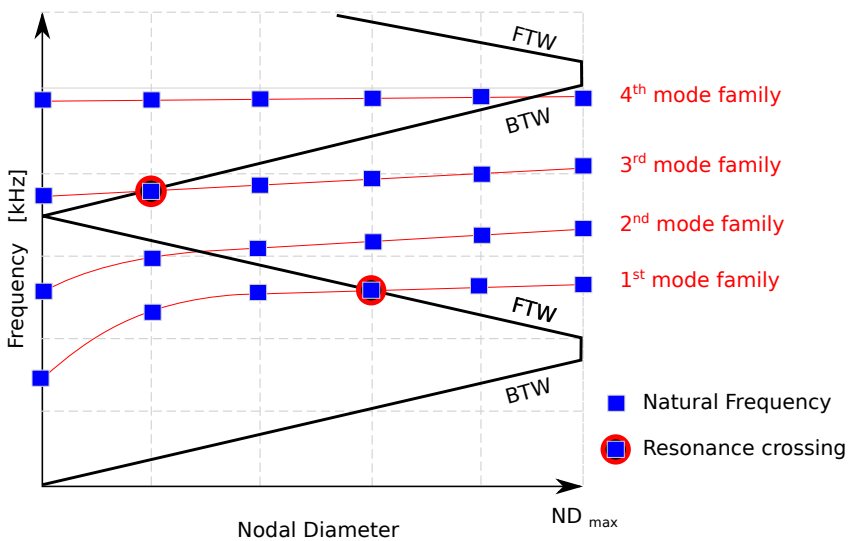
$$ND_{max} = \begin{cases} Z/2 & \text{Even Blade Count} \\ (Z-1)/2 & \text{Odd Blade Count} \end{cases} \quad (2.22)$$

### 2.3.4 Resonance Crossings

To excite the turbine blisk mode-shapes, two conditions are required to be fulfilled:

- (a) Excitation frequency must equal the natural frequency of the rotor.
- (b) the circumferential excitation pattern and nodal diameter pattern must coincide.

These conditions are satisfied at the crossing of the natural frequency and the excitation zig zag line as shown in the ZZENF (Zig Zag shaped Excitation line in Nodal diameter versus Frequency) diagram in Figure 2.13.



**Figure 2.13:** ZZENF diagram

The blue squares represent the rotor eigenfrequencies, and the zig-zag line represents the excitation frequency at a single rotational speed, ( $N$ ) as a function of  $ND$ . This is described in Equations 2.23 and 2.24, where  $EO$  is the Engine Order (integer multiple of the rotational speed),  $ND_{max}$  is the max possible  $ND$  according to Equation 2.22.

$$f_{excit} = EO \frac{N}{60} \quad (2.23)$$

$$EO = \begin{cases} \exists a \geq 0, \forall ND = \{0 : ND_{max}\} : EO = (aZ + ND) & \text{BTW} \\ \exists b > 0, \forall ND = \{0 : ND_{max}\} : EO = (bZ - ND) & \text{FTW} \end{cases} \quad (2.24)$$

Different NDs can also be represented in terms of the Traveling Wave Modes (TWM), which result from the nodal diameter lines rotation. The traveling wave has two possible directions with respect to the blisk rotational direction. BTW is Backward Traveling Wave (counter the rotational direction), and FTW is the Forward Traveling Wave (with the rotational direction). This traveling wave is defined by the Inter-Blade Phase Angle (IBPA) which represent the relation between the ND and the blade count as follow:

$$\sigma = \frac{2 \pi ND}{Z} \quad (2.25)$$

### 2.3.5 Excitation Forces

In several applications, it may be impossible to avoid operating at resonance crossing as shown in the ZENF diagram Figure 2.13. Therefore it becomes crucial to investigate the excitation forces to avoid the HCF consequences.

An evaluation to the excitation mechanism and its intensity takes place followed by a forced response analysis to confirm that the turbine will operate at the infinite lifetime region as described in the Figure 2.10. The turbine blisk excitation sources are described in Figure 2.14 and are classified as follow:

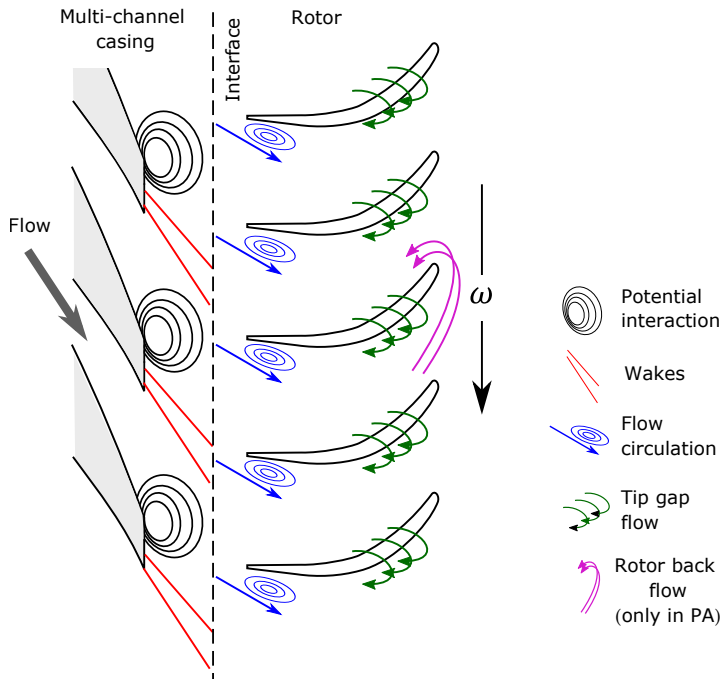
(a) Potential interaction

The relative motion between the rotor and the casing creates an unsteady potential field which results in unsteadiness in the static pressure field acting on the rotor.

(b) Wakes

The dead zone between two casing channels forms a wake region. When the rotor passes through this region the leading edge static pressure is reduced and causes flow unsteadiness.

(c) Flow circulation at LE



**Figure 2.14:** Excitation mechanisms in RT featuring MC

Operating at off-design condition causes a flow incidence that produces an unsteady flow circulation at the leading edge.

(d) Tip gap flow

The pressure difference between the pressure and suction sides results in flow leakage between the rotor tip and the casing shroud. This flow is characterized by unsteady circulation.

(e) Rotor back flow

Operating the radial turbine at Partial Admission (PA) mode causes an unsteady backflow between two adjacent rotor passages having different static pressure.

All these flow unsteadiness can excite the turbine blisk and cause blade vibration if the resonance conditions are satisfied as described before.

### 2.3.6 Damping

At the resonance crossing, the maximum vibration amplitude is not only controlled by the excitation force but also by the system damping. Therefore predicting the damping coefficient is important to solve the dynamic equation of motion. Mechanical and aerodynamic damping are considered the main damping sources for turbomachinery blisks. In radial turbine application, the contribution of the mechanical damping is negligible compared to the contribution aerodynamic damping as described by Giersch et al., Kammerer et al. and Zemp et al. [26, 38, 84].

There may be situations in which the aerodynamic damping is dominant in the radial turbine application. Aerodynamic damping can reach up to 0.02 of the critical damping ration as reported in [47]. It is generated by the static pressure perturbation caused by fluid-structure interaction during the blade vibration. The effect of fluid-structure interaction on the static pressure is explained in Figure 2.15. Aerodynamic damping is affected mainly by the operating condition, mode-shapes, vibration frequency, and IBPA.

Mayorca [47], Vasanthakumar [75], and Elder et al. [19] calculated the aerodynamic damping coefficient using the following derived equation:

$$\zeta_{aero} = \frac{-W_{cycle}}{8 \cdot \pi^3 \cdot f^2 \cdot SF^2} \quad (2.26)$$

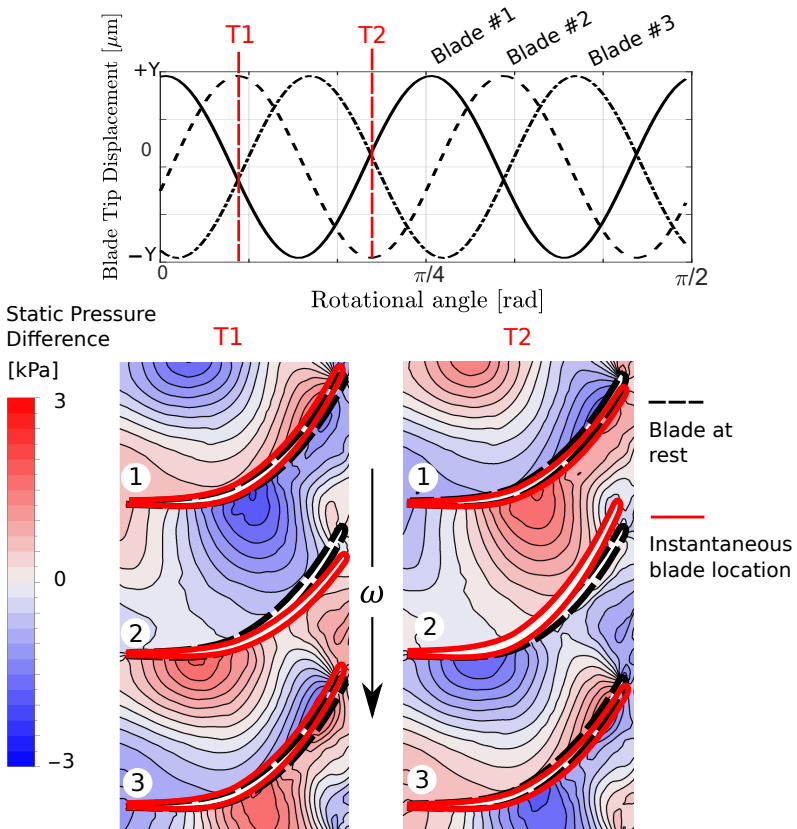
where  $W_{cycle}$  is the exchange work between the blade and the surrounding fluid during one vibration cycle and can be calculated using the following equation:

$$W_{cycle} = \int_{t_0}^{t_0+T} \int p \vec{v} \cdot \vec{n} dA dt \quad (2.27)$$

## 2.4 Computational Fluid Dynamics

Similar to other types of turbomachinery, radial turbines are characterized by a highly turbulent flow with a wide range of time and length scales.





**Figure 2.15:** Static pressure perturbation due to blade vibration

Navier-Stokes equations are used to describe the flow in the radial turbine. Many approaches are presented to solve these equations numerically and simulate the flow in the turbine. Resolving all range of time and length scale can be achieved by the Direct Numerical Simulation (DNS) which is not used because of its high computational cost. Smagorinsky [73] presented another approach to solve the Navier-Stokes equation by filtering out the smallest length scales, which are the most computationally expensive to resolve. This approach is known as Large Eddy Simulation (LES) and its application in turbomachines flow simulation started to grow after the exponential increase of

the computational power. However, it still requires relatively high calculation time.

Applying Reynold decomposition to the Navier-Stokes equations and averaging it with respect to time results into the Reynolds-averaged Navier-Stokes equations (RANS) [1]. These equations can be used with some approximation to model the turbulent flow as presented for the first time by Reynold [64]. RANS equations for compressible flow can be written after dropping the bar for averaged quantities, except for products of fluctuating parts as follows [4]:

$$\frac{\partial \rho}{\partial t} + \frac{\partial}{\partial x_i} (\rho u_i) = 0 \quad (2.28)$$

$$\frac{\partial \rho u_i}{\partial t} + \frac{\partial}{\partial x_j} (\rho u_i u_j) = -\frac{\partial p}{\partial x_i} + \frac{\partial}{\partial x_j} (\tau_{ij} - \rho \overline{u_i u_j}) + S_M \quad (2.29)$$

$$\frac{\partial \rho h_t}{\partial t} - \frac{\partial p}{\partial t} + \frac{\partial}{\partial x_j} (\rho u_j h_t) = \frac{\partial}{\partial x_j} \left( \lambda \frac{\partial T}{\partial x_j} - \rho \overline{u_j h} \right) + \frac{\partial}{\partial x_j} \left[ u_j (\tau_{ij} - \rho \overline{u_i u_j}) \right] + S_E \quad (2.30)$$

The presented equations are second-order nonlinear partial differential equations in 3D space. They have three velocity components  $u_i$ , pressure  $p$ , temperature  $T$ , density  $\rho$ , and enthalpy  $h$  as unknown variables. To close the system of equations, the equations of state for density  $\rho$  and for enthalpy  $h$  are required. they can be described for the ideal gas as follows [4]:

$$\rho = \frac{p}{RT} \quad (2.31)$$

$$dh = c_p(T) dT \quad (2.32)$$

In the framework of this study, the RANS equations are solved using the commercial software Ansys CFX 19.2 [2–4]. The Reynold stresses ( $\rho \overline{u_i u_j}$ ) and Reynold flux ( $\rho \overline{u_j h}$ ) terms in RANS equations are modeled using the Shear Stress Transport (SST) two-equation eddy-viscosity turbulence model. The model combines the  $k-\omega$  turbulence model [81, 82], and  $k-\epsilon$  turbulence model [37, 44] such that the  $k-\omega$  is used in the inner region of the boundary layer and switches to the  $k-\epsilon$  in the free shear flow [52].

The gradients of the flow variables in the near wall region (boundary layer) are higher compared those in the mainstream region. Therefore the numerical grid of this region requires special treatment for accurate flow prediction. Flow in turbulent boundary layer depends on the wall distance  $y$ , kinematic viscosity  $\nu$  and the shear-stress velocity  $u_\tau$ . These parameters form a dimensionless parameter  $y^+$  as follow:

$$y^+ = \frac{y u_\tau}{\nu} \quad (2.33)$$

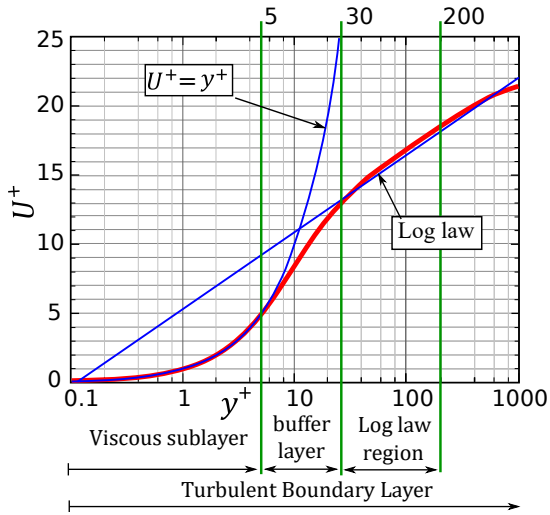
where the shear-stress velocity  $u_\tau$  is function of the wall shear-stress and the fluid density  $\rho$  as follow:

$$u_\tau = \sqrt{\frac{\tau_w}{\rho}} \quad (2.34)$$

The dimensionless parameter is used in the CFD simulation to assess the boundary layer discretization.

Choosing appropriate  $y^+$  value is very important to accurately predict the flow in the boundary layer and save the computational time. For instance, when using the SST it is important to choose  $y^+$  between 1 and 5 to use the enhanced wall treatment method and accurately resolve the viscous sub-layer as described in Figure 2.16. In the turbomachinery application, the transition from the viscous sublayer to the buffer layer takes place at  $y^+$  lower than 5 due to the strong curvature, separation, and pressure gradient. Therefore, in Turbomachinery simulation,  $y^+$  is recommended to be around 1 to avoid placing the first cell on the buffer layer.

For complex geometries it becomes difficult to place the first cell in the viscous sub-layer. Thus it can be placed in the log law region with  $y^+$  between 30 and 200 and using a scalable wall function to reasonably predict the majority of high-Reynolds-number, wall-bounded flows. The automatic wall function in the CFX solver is a powerful tool to switch between the enhanced wall treatment and the selected wall function based on the  $y^+$  value. At any cases, the  $y^+$  is not recommended to be between 5 and 30 because it fails to predict the flow using neither the linear nor the logarithmic function as shown in the buffer layer region in Figure 2.16.



**Figure 2.16:** Law of the wall, flow between two parallel plates

## **3 State-of-the-art of RT Operation Control**

Fixed geometry turbochargers without control mechanisms have two main problems. Firstly, at a low ICE rotation speed, the amount of exhaust gas is not enough to efficiently drive the turbine which leads to an insufficient or none compressor boost. Secondly, at high ICE rotational speed, the exhaust gases with high mass flow rate drive the turbine at high rotational speed and expansion ratios which result in an excessive compressor boost. Besides, the turbine choke results in an increase in the ICE back-pressure and cut on power. These matching problems are illustrated in Figure 2.9.

This chapter presents and explains the most commonly used mechanisms in controlling the operation of the radial turbine and solve these problems. Two main control concepts are being widely used: the wastegate and the Variable Geometry Turbine (VGT). VGT is presented in this study by the Variable Nozzle Turbine (VNT) mechanism and the Variable Area turbine (VAT) mechanism. The other machines which are used to vary the turbine geometry are not considered in this chapter.

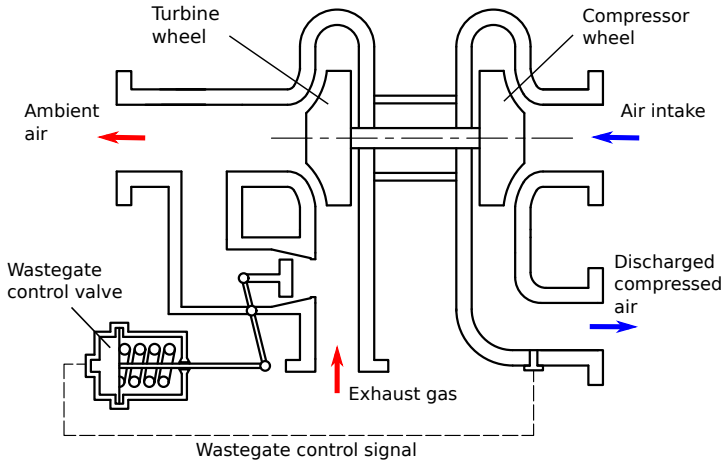
### **3.1 Wastegate**

A wastegate is a bypass valve that redirects a certain amount of the exhaust gases around the turbine rotor in a turbocharger to limit the compressor boost. A schematic drawing for the wastegate turbocharger is shown in Figure 3.1

#### **3.1.1 Function**

- (a) Limit the compressor boost at high ICE speed

A portion of the ICE exhaust gases is discharged through the wastegate valve i.e. bypassed around the turbine wheel. This results in a lower



**Figure 3.1:** Turbocharger featuring wastegate schematic drawing

turbine flow and gives a constant boost pressure at high ICE speed which avoids choke conditions. This process is described in the turbocharger matching map by the blue points in Figure 3.2.

(b) More compressor boost at low ICE speed

Wastegate usage facilitates utilizing a lower flow capacity turbine (low  $A/R$  ratio) compared to the ideal size for mid-speed design point. This provides a higher low-speed boost pressure far from the surge conditions. This process is described in the turbocharger matching map by the green points in Figure 3.2.

### 3.1.2 Classifications

#### According to installation position

(a) External

An external wastegate is an unconnected self-contained mechanism typically used with turbochargers that do not have an internal wastegate.

## (b) Internal

An internal wastegate is an integrated bypass valve and passage within the turbine casing which allows part of the exhaust gases to bypass the turbine wheel into the downstream exhaust.

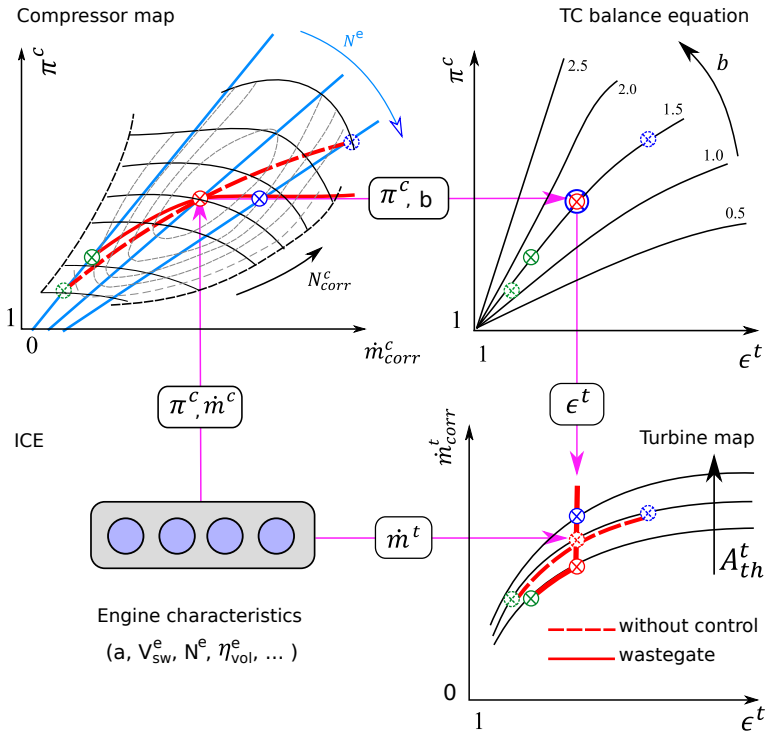


Figure 3.2: Turbocharger matching map for wastegate

### According to control type

## (a) Pneumatic

The pneumatic control mechanism is considered the simplest closed-loop control mechanism for a wastegate. It is based on supplying pressurized air directly from the discharge side of the compressor

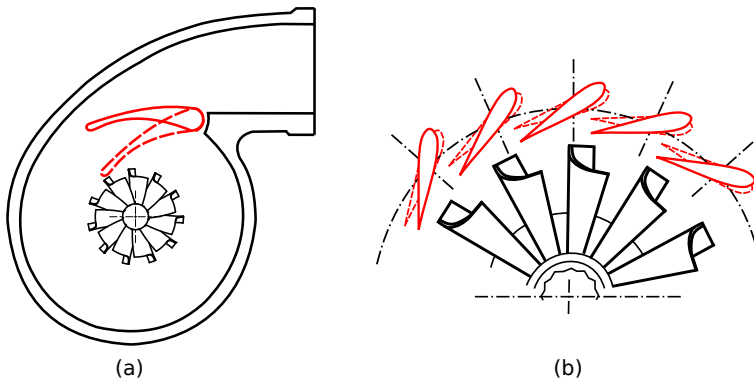
to the wastegate actuator. The wastegate will open further as the pressurized air pushes against the spring in the wastegate actuator till equilibrium is reached.

(b) Electric

The Electric control mechanism is based on an electric signal from the Electronic Control Unit (ECU) of the engine to open or close the wastegate and achieve the required boost level.

## 3.2 Variable Geometry Turbine

Although the wastegate provides a higher boost at low ICE speed and limits the boost at high speed, it wastes part of the exhaust gases and limits the boost at design point. This where the advantage of using the Variable Geometry Turbine (VGT) mechanisms comes in. It is a controlling approach that changes the geometry of the turbine housing as the ICE speed changes. Many different mechanisms are used to achieve this geometry change. In this section, the Variable Area Turbine (VAT) and the Variable Nozzle Turbine (VNT) are presented as the most commonly used mechanisms nowadays. The schematic drawing for both control mechanisms is shown in Figure 3.3.

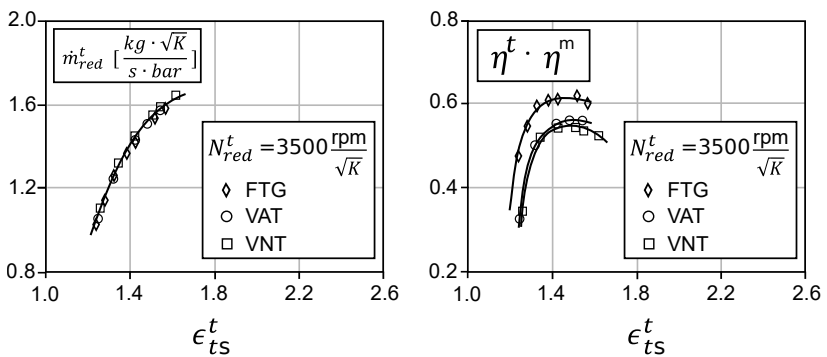


**Figure 3.3:** Schematic of the VAT (a) and VNT (b) control mechanisms

Capobianco and Gambarotta [9] performed a comparison between the VGT and the wastegate. The first step of this comparison was to ensure a comparable mass flow condition for all these turbocharger control mechanisms.



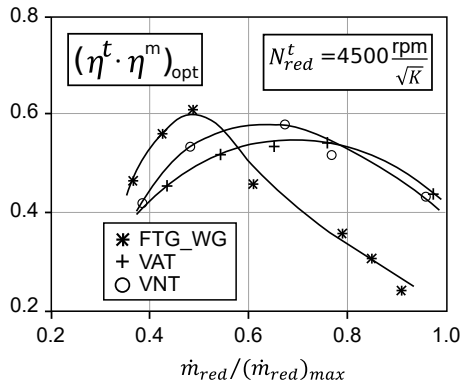
Therefore, they adjusted the position of the guide vane in case of the VNT and the movable element in case of the VAT to operate the turbocharger at the same mass flow compared to Fixed Turbine Geometry (FTG) with completely closed wastegate as shown in Figure 3.4. The comparison shows that the FTG with a closed wastegate at low ICE speed has relatively higher efficiency compared to the VGT. This is due to incidence losses, increased friction surface (due to the more walls), leakage losses through clearances between contour walls and vanes and, the wake losses behind the guiding element in the case of VAT as reported by Flaxington et al. and Hirihikawa et al. [21, 33].



**Figure 3.4:** Turbine performance for VTG and FTG (adapted from Capobianco and Gambarotta [9])

Although the wastegate has a relatively high-efficiency at low ICE operating speed, its efficiency drop after being opened at the higher speed range in order to bypass part of the ICE exhaust gases to limit the compressor boost [8]. In contrast, the VGT can adjust the throat area and shows better performance at a wider range of operation compared to the wastegate as described in Figure 3.5.

Matching between the turbine featuring VGT mechanisms and the compressor to the ICE is described in Figure 3.6. At low engine speed, the control mechanism reduces the turbine inlet area to accelerate the exhaust gases and increase the turbine operating pressure ratio. These in turn provide higher compressor boost and avoid operating it at surge conditions. Turbocharger operation at low engine speed for both controlled and uncontrolled turbine are represented by the green points in Figure 3.6.



**Figure 3.5:** Optimum efficiency for VGT and FTG (adapted from Capobianco and Gambarotta [9])

At high engine speed, the control mechanism increases the inlet turbine area to provide more turbine capacity and adjust the turbine expansion ratio to avoid high compressor boost and choke condition. This operation is represented by the blue points in Figure 3.6.

Most of the gasoline engines depend on the wastegate mechanism in controlling turbocharger. The idea of the VGT is still not widely applicable to such engine type. Two main reasons are behind the difficulty of using VGT in the gasoline engine. First, the high temperature of the exhaust gases which produce high thermal stresses on the movable parts. seconds, the turbocharger size is small which makes it difficult to fit such movable parts in the turbine housing.

In contrast, the diesel engine is characterized by a lower exhaust gas temperature compared to gasoline engines. besides, the turbochargers attached to it are relatively bigger. Therefore, the VGT is applicable for such engines.

The gasoline engine still waiting for a cheap and reliable control system that has efficient performance than the wastegate systems [76].

MC is a novel control system based on fixed geometry and aims to achieve a controlled operation comparable to the VGT by applying different partial admission configuration. This achieves the simplicity of the wastegate with

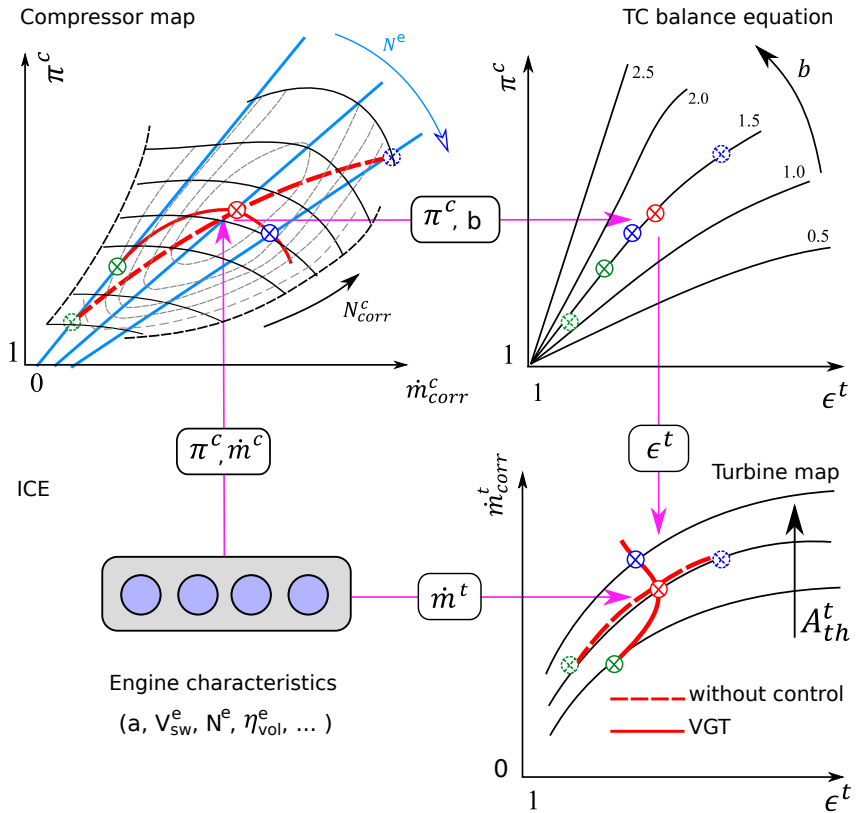


Figure 3.6: Turbocharger matching map for VGT

the efficiency of the VGT. The design model of the MC and its effect on many radial turbine design aspects is explained in the following chapters.

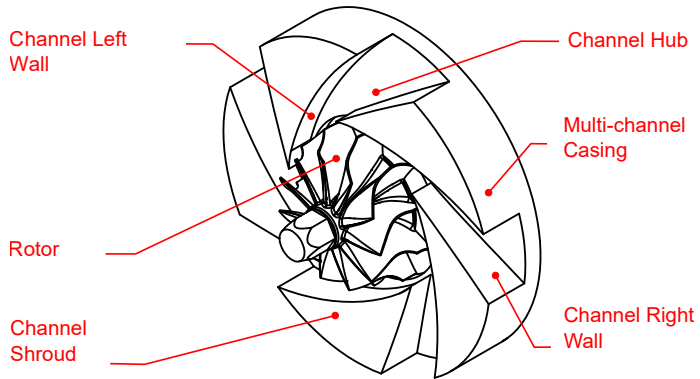


## 4 Multi-channel Casing Design

This chapter illustrates the MC concept and the design procedures to replace the traditional spiral casing while fulfilling the basic requirements from the turbine casing as described by Ebaid [18]. The replacement process takes place based on two objectives. Firstly, MC should provide a comparable mass flow rates during turbine operation. Secondly, running the turbine at an acceptable efficiency compared to the original system.

### 4.1 Definitions

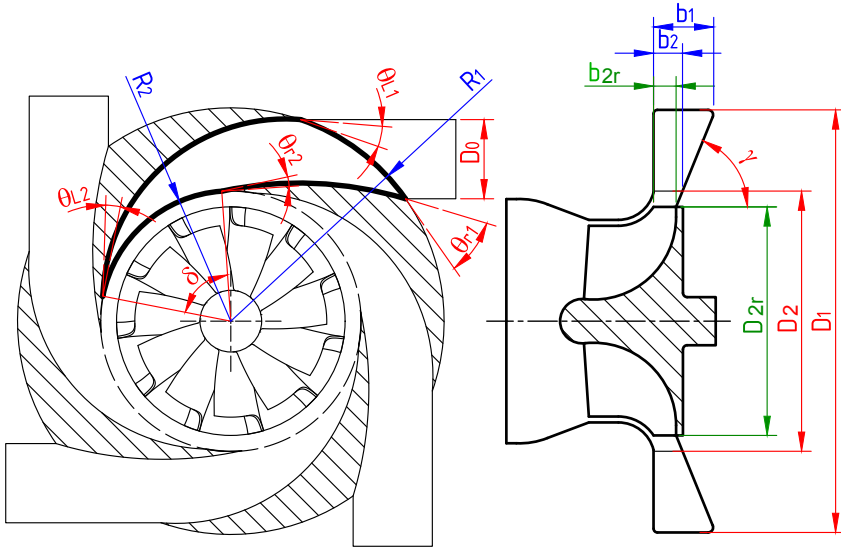
Multi-channel Casing is a radial turbine casing that replaces the traditional spiral one to provide a turbine operation controllability. It consists of multiple flow channels, each channel bound by four surfaces: right and left side-walls (single arc curvature), hub wall and shroud wall as shown in Figure 4.1. Each channel provides the turbine separately with the working fluid. The turbine operation can be controlled by closing and opening different channel combinations.



**Figure 4.1:** Multi-channel casing geometrical parameters

## 4.2 Design parameters

Nine independent parameters describe the shape of the channel. These parameters are represented in red color in Figure 4.2 and listed in Table 4.1. The other input or dependent parameters are represented in green and blue, respectively.



**Figure 4.2:** Multi-channel casing geometrical parameters

The flow channel can be represented as a curved nozzle with a throat area ( $A_{th}$ ) as shown in Figure 4.3. This area can be represented as follows:

$$A_{th} = f_1(D_1, D_2, \delta, \gamma, \theta_{r1}, \theta_{r2}, \theta_{L1}, \theta_{L2}) \quad (4.1)$$

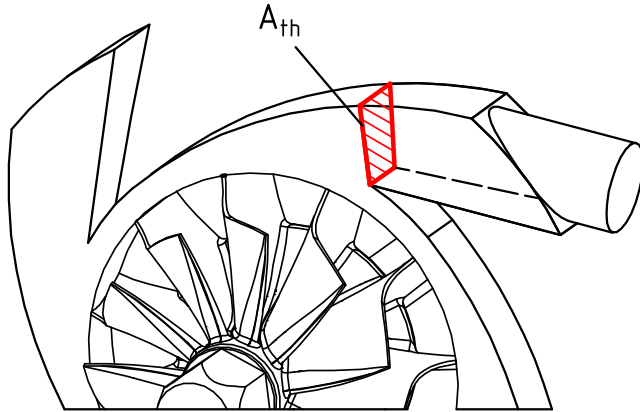
The function  $f_1$  is derived in Appendix 1. Part of the design parameters can be constrained based on practical considerations as follows:

- (a) Minimizing the flow separation in the interaction between the inlet tube outlet and channel inlet by installing them tangentially.

$$D_0 = b_1 = f_2(\gamma), \quad \theta_{r1} = f_3(\theta_{L1}) \quad (4.2)$$

**Table 4.1:** Multi-channel casing design parameters

Parameter	Description	Type
$D_1$	Casing inlet diameter	Independent parameter
$D_2$	Casing outlet diameter	Independent parameter
$D_0$	Inlet tube diameter	Independent parameter
$b_1$	Casing inlet width	Dependent parameter
$b_2$	Casing outlet width	Dependent parameter
$\delta$	Opening angle	Independent parameter
$\gamma$	Hub inclination angle	Independent parameter
$\theta_{r1}$	Casing right wall inlet angle	Independent parameter
$\theta_{r2}$	Casing right wall outlet angle	Independent parameter
$\theta_{L1}$	Casing left wall inlet angle	Independent parameter
$\theta_{L1}$	Casing left wall outlet angle	Independent parameter

**Figure 4.3:** Multi-channel casing throat cross-section area

(b) For smoother channel curvature, the casing channel outlet angles are dependent.

$$\theta_{r2} = f_4(\theta_{L2}) \quad (4.3)$$

After considering previous design constraints, Equation 4.1 can be reduced to the form:

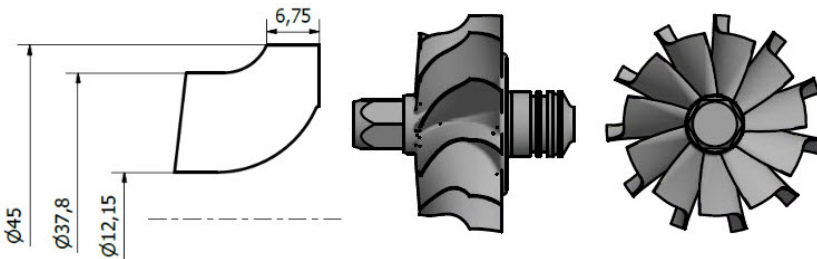
$$A_{th} = f_5(D_1, D_2, D_0, \delta, \theta_{L1}, \theta_{L2}) \quad (4.4)$$

The total casing throat area is considered as follows:

$$A_{th,t} = A_{th} \times N_{ch} = f(N_{ch}, D_1, D_2, D_0, \delta, \theta_{L1}, \theta_{L2}) \quad (4.5)$$

### 4.3 Test case

The turbocharger K03/05 from Borg Warner Turbo Systems (BWTS) is chosen as a test object in this study. The radial turbine of this turbocharger is designed originally with a traditional spiral casing. The performance characteristic of it is chosen as a reference performance to be compared with the MC performance. The main metrics for the turbine rotor are shown in Figure 4.4.



**Figure 4.4:** Turbine rotor

The performance of the turbine featuring spiral casing at different expansion ratios and rotational speeds is tested experimentally to validate the steady with mixing-plane CFD model. After the validation, the spiral casing is replaced by an MC casing in the CFD model to study the effect of different geometrical parameters on the turbine performance. This parametric study is presented in the following section.



## 4.4 Parametric study

The total throat area of flow channels in MC is governed by seven parameters as described in Equation 4.5. This section assesses the effect of these parameters on the turbine performance including mass flow rate and the operating efficiency. This assessment takes place through a parametric study using a CFD model which is explained in chapter 6.

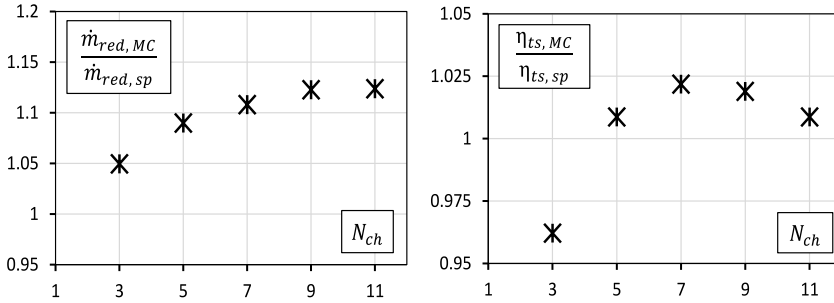
### 4.4.1 Channel Count

Channel count is a key factor in MC design process. Understanding its effect on the turbine performance helps the designer to select an optimum value. Therefore, different cases have been numerically investigated to achieve this target. These cases have the same total throat area which is equal to the throat area of the spiral casing but with different channel count. This investigation takes place at the same operating conditions and the same channel shape.

The performance of a radial turbine featuring an MC with different channel count in comparison with a traditional spiral casing is shown in Figure 4.5. The reduced mass flow rate and the isentropic efficiency for different channel counts are normalized by the reduced mass flow rate and the isentropic efficiency of the spiral casing at the same operating conditions. It shows that the MC has a higher swallowing capacity compared to the spiral casing even with the lowest channel count. Moreover, increasing the channel count leads to an increase of the swallowing capacity of the MC. On the other hand, the isentropic efficiency of MC increases with increasing channel count up to a certain value and then decreases again.

To understand the reasons behind the increase in the turbine swallowing capacity, a flow field investigation is performed. It evaluates the changes in some flow aspects that might have led to this effect, e.g., the operating mass flow rate, absolute velocity angle at the rotor inlet, and the flow behavior at the radial gap between the rotor and the casing.

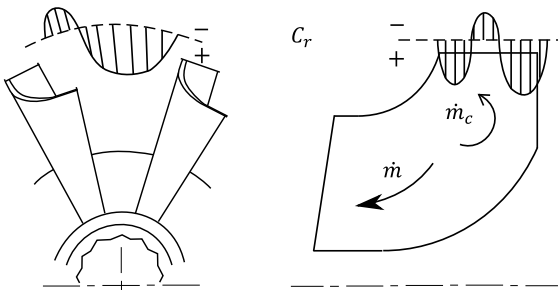
The flow investigation shows that MC with different channel count has a significant effect on the rotor inlet velocity angle. Theoretically, an infinite number of casing channels leads to a homogeneous flow angle without any flow deviation from the designed angle. However, in real design due to the finite number of channels, the flow can deviate from the designed



**Figure 4.5:** Effect of channel count on the turbine performance

angles, which results in flow circulation at the rotor-casing interface which in turn affects the operating mass flow rate and efficiency. To quantify this phenomenon for different channel count, the circulating flow at the turbine rotor inlet is calculated from the numerical results using Equation 4.6 [28] after calculating the radial velocity components for each case as described in Figure 4.6.

$$\dot{m}_c = \frac{1}{2} \rho \left[ \int_A |C_r| dA - \int_A C_r dA \right] \quad (4.6)$$

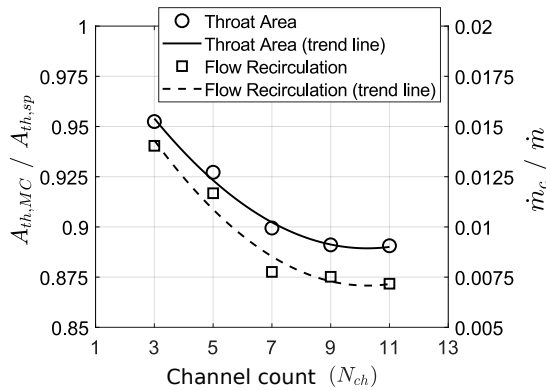


**Figure 4.6:** Radial velocity component at rotor inlet

The MC with different channel count has been designed to operate at a comparable mass flow rate as the reference wastegate spiral casing. This required total throat area adjustment by adjusting different design param-

ters as described in Equation 4.5. The change in throat area compared to the reference case and the mass flow rate of the circulating flow relative to the main mass flow rate for different MC channel count is represented in Figure 4.7.

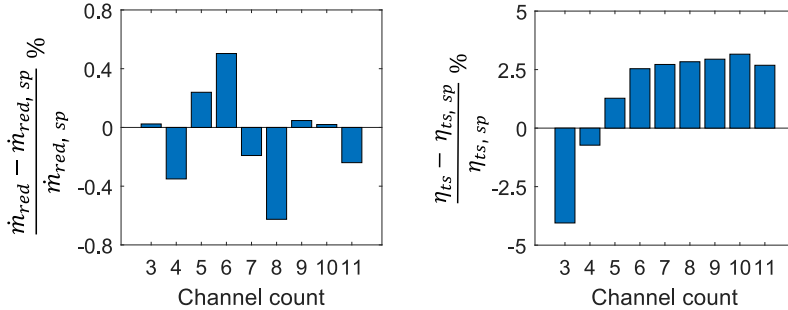
The results show that operating the RT at a comparable mass flow rate requires reducing the MC throat area when increasing the channel count, as described by the throat area trend line in Figure 4.7. Moreover, the mass flow rate of the circulating flow at the rotor-casing interface for different channels count has the same trend as the reduction of throat area. This indicates that the reason behind the high swallowing capacity of the MC is resulting from enhancing the flow guidance by reducing the slip factor of the flow at rotor inlet. The enhancement of flow guidance increases with the MC channels count.



**Figure 4.7:** Relation between throat area and flow circulation for different  $N_{ch}$

Regarding the operating efficiency, increasing the MC channel count reduces the loss produced by the circulating flow at the rotor-casing interface. However, a high number of channels leads to higher friction losses due to the increase of the wetted surfaces. Therefore, there is an optimum channel count and after this number, the efficiency drops again due to the increase of the friction losses. This optimum value is between seven and ten channels, depending on the operating condition as shown in Figure 4.8. It represents the performance deviation between MC and reference case. The deviation in mass flow is lower than 0.5% which allows a reliable efficiency comparison.

Moreover, the MC with 3 and 4 channels shows lower operating efficiency compared to the spiral casing, while MC with 5 channels and more have a higher efficiency compared to the spiral casing.



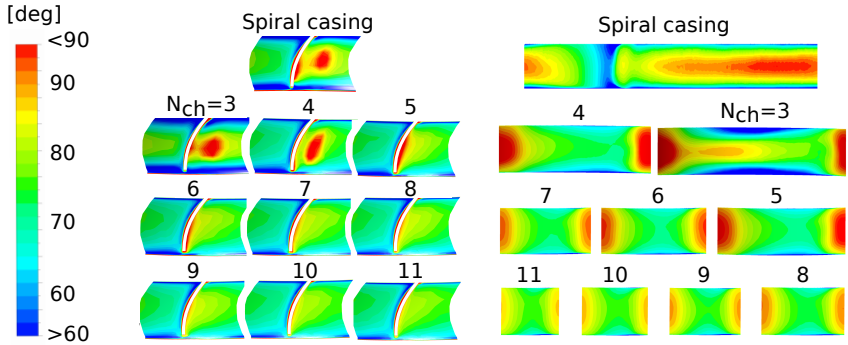
**Figure 4.8:** Turbine performance for different  $N_{ch}$

To illustrate the effect of channel count on the inflow angle at the rotor-casing interface, a contour plot of the absolute velocity angle is shown in Figure 4.9. It represents the angle values at the rotor inlet and the casing outlet. Increasing the channel count leads to more homogeneous inflow angle and reduces the backflow at the rotor inlet. Lower channel count leads to highly deviated inflow angles compared the optimum one which is defined around 72 degree as described before in Figure 2.2. The highest deviation can be found at the space between two adjacent channel flows in the casing outlet and immediately at the rotor inlet near the blade leading edge from the pressure side, hub and shroud.

#### 4.4.2 Channel Outlet Diameter

Channel outlet diameter ( $D_2$ ) represents the diameter at the casing nozzle end as described in Figure 4.2. In this study, it is defined as a dimensionless parameter by normalizing it using the rotor inlet diameter ( $D_{2r}$ ). This dimensionless parameter represents the radial gap between the casing outlet and the rotor inlet.

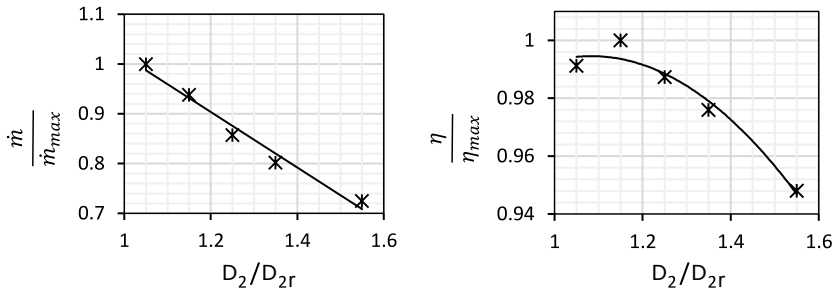
This section investigates the effect of the channel outlet diameter on the performance of a radial turbine featuring MC. Five MC cases with different radial gaps are modeled for this purpose starting from narrow radial gap ( $D_2/D_{2r} = 1.05$ ) to a wide gap ( $D_2/D_{2r} = 1.55$ ). All other design parameters



**Figure 4.9:** Absolute velocity angle ( $\alpha$ ) contours: (left) rotor inlet, (right) casing outlet

are adjusted to achieve a constant throat area ( $A_{th}$ ) and constant channel outlet area for all these selected cases. This comparison takes place at the same operating conditions.

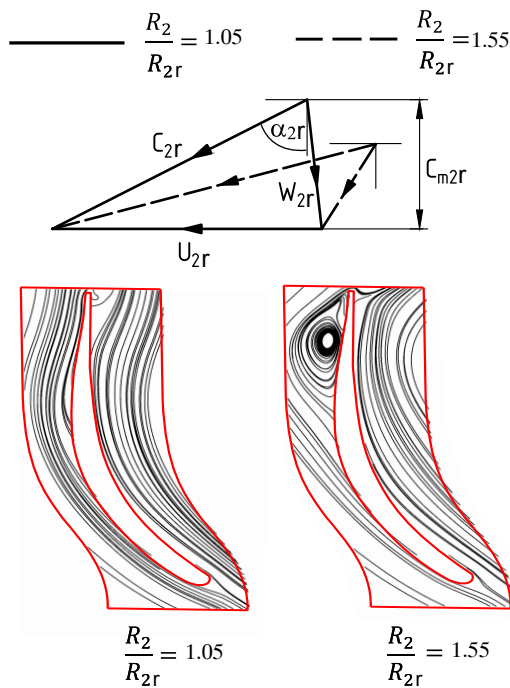
The effect of different radial gaps on the reduced mass flow rate and isentropic total to static efficiency is shown in Figure 4.10. Increasing the gap between the casing and the rotor inlet results in an almost linear reduction of the mass flow rate. Regarding the operating efficiency, it slightly increases with the increase of the radial gap up to certain critical value where  $R_2/R_{2r} = 1.15$  and then deteriorates after it.



**Figure 4.10:** Effect of the channel outlet diameter on the turbine performance

To understand the effect of the radial gap on the turbine mass flow rate, the velocity triangle for the different radial gap cases is calculated. Increasing the radial gap deviates the velocity triangle at the rotor inlet from its ideal form at the best efficiency point. An increase in radial gap increases the absolute velocity inlet angle ( $\alpha$ ) and the relative inlet velocity angle ( $\beta$ ). This leads to a high positive inflow angle as described in Figure 4.11.

This deviation in the velocity triangle reduces the radial velocity component at the rotor inlet resulting in a lower mass flow rate. It has also an effect on the operating efficiency. High inflow incidence produces flow vortex as described by the flow streamline at rotor midspan for two different radial gap values in Figure 4.11. This vortex increase energy losses and reduces operating efficiency.

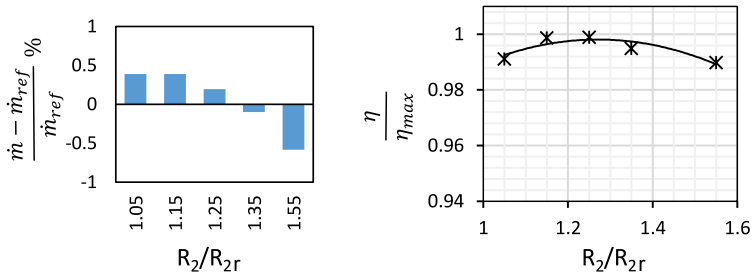


**Figure 4.11:** Effect of the channel outlet diameter on the flow direction, Top: Velocity triangle at rotor inlet. Bottom: Streamlines at rotor mid span.

To compensate the effect of increasing the radial gap and achieve comparable mass flow rate for different radial gaps, the throat area for single channel should be increased linearly according to the following relation.

$$A_{th} = 64.28 \left( \frac{D_2}{D_{2r}} \right) + 6.45 \quad (4.7)$$

After adjusting the channel throat area, the deviation percentage of mass flow rate from the reference value and the operating efficiency is plotted in Figure 4.12. It shows that the linear increase of channel throat area with increasing the radial gap achieves a comparable turbine mass flow rate. Therefore, the variation in efficiency as shown in Figure 4.12 is only because of the change in the radial gap.



**Figure 4.12:** Effect of the channel outlet diameter on the turbine performance, at comparable mass flow rate

In comparison with the movable guide vanes, the radial gap effect on operating efficiency is similar to its trend for the new MC. This could be compared with the trend concluded by Ke et al. [40]. They performed an investigation about the effect of the different radial gaps between the turbine rotor and the guide vanes on the turbine performance.



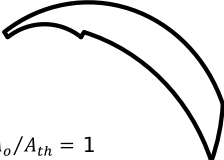



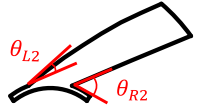


### 4.4.3 Other Geometrical parameters

This section investigates the effect of the remaining geometrical parameters on the turbine performance. These parameters are linked to each other therefore their effect on the performance is presented in combination with each other. Each combination of these parameters includes channel inlet angle

( $\theta_{L1}$ ), channel outlet angle ( $\theta_{L2}$ ), opening angle ( $\delta$ ), and casing inlet diameter ( $D_1$ ) represents a different shape of the flow channel and its inclination relative to the rotor inlet.

The flow in each casing channel can be considered as a flow inside a nozzle. This nozzle is characterized by the area ratio ( $A_0/A_{th}$ ) which represents the inlet tube cross section area divided by the channel throat area and the nozzle inclination angle relative to the rotor. Fifteen cases are generated representing different shapes of the casing channel as shown in Table 4.2 and 4.3.

**Table 4.2:** Geometrical parameters for the first group of selected cases

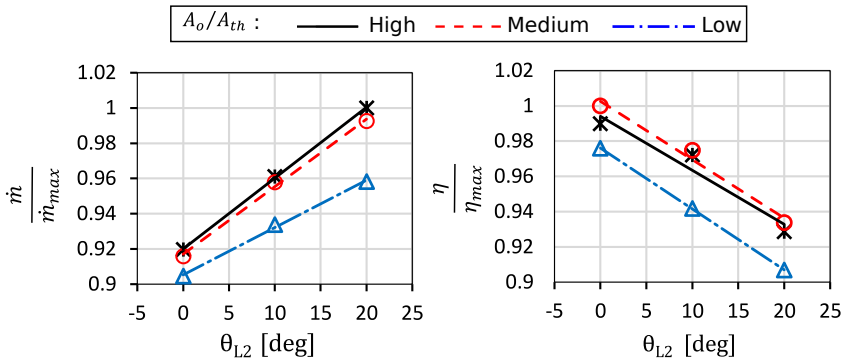
$D_1 = 130\text{mm}$ , $D_2 = 50\text{mm}$ , $N_{ch} = 5$ , $A_{th} = 73\text{ mm}^2$ , $\theta_{R2} = \theta_{L2} + 20\text{ deg}$			
	$A_o/A_{th} \equiv \text{High}$	$A_o/A_{th} \equiv \text{Medium}$	$A_o/A_{th} \equiv \text{Low}$
$\theta_{L2} = 0\text{ deg}$	 $A_o/A_{th} = 3$	 $A_o/A_{th} = 2$	 $A_o/A_{th} = 1$
$\theta_{L2} = 10\text{ deg}$	 $A_o/A_{th} = 2.5$	 $A_o/A_{th} = 1.75$	 $A_o/A_{th} = 1$
$\theta_{L2} = 20\text{ deg}$	 $A_o/A_{th} = 2$	 $A_o/A_{th} = 1.5$	 $A_o/A_{th} = 1$

The first nine cases as shown in Table 4.2 represent a combination between different area ratios and channel outlet angles. A low area ratio produces a channel with high curvature. This curvature reduces with increasing the



outlet angles. All these casings are designed to have a comparable size ( $A_{th} = \text{constant}$ ) in order to have a reasonable comparison.

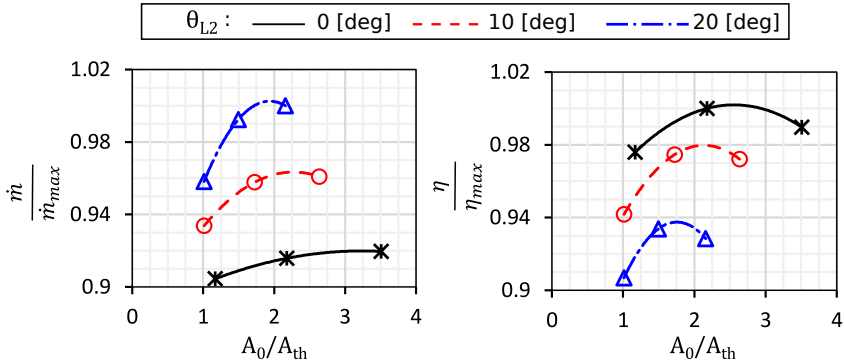
The effect of the channel outlet angle for different area ratios is shown in Figure 4.13. Different area ratios show comparable turbine performance behavior for different outlet angles. The turbine mass flow rate increases linearly with an increasing outlet angle. This behavior is attributed to the reduction in the flow angle ( $\alpha_2$ ) which leads to higher radial component of the absolute velocity at the rotor inlet for the same rotational speed. This figure shows also that the mass flow rate sensitivity towards the outlet angle is dominant compared to the change in area ratio of the channel. The mass flow rate could be affected up to 7% for the mentioned change range of the outlet angle. Moreover, increasing the outlet angle reduces operating efficiency. This is attributed to the change in inflow angles as well as the change in flow velocity due to different operating mass flow rate.



**Figure 4.13:** Effect of the channel outlet angle on the turbine performance for different casing area ratios

Effect of the different area ratio on the turbine performance for different outlet angles appears in Figure 4.14. The change in the area ratio has a minor effect on the mass flow rate except for the low values where the channel has a significant curvature. In this case, the operating mass flow rate reduces within range of 1% to 4% depending on the channel outlet angle.

Regarding the operating efficiency, it is recommended to design the channel with a medium area ratio or slightly higher to achieve maximum efficiency as described in Figure 4.14.



**Figure 4.14:** Effect of the channel area ratio on the turbine performance for different casing outlet angles

All previous cases have shown the turbine performance is sensitive toward change in the casing outlet angles. Therefore it is chosen to be combined with other geometrical parameters to confirm its effect. The next nine cases which are presented in Table 4.3 represent a combination between different outlet angles and different casing inlet diameters.










Turbine performance for different channel outlet angles and different inlet diameters are presented in Figure 4.15. The results show a comparable behavior with the previous cases. The turbine mass flow rate increases linearly by increasing channel outlet angle for all inlet diameters. Whereas the operating efficiency reduces linearly by increasing the outlet angles.

The channel outlet diameter shows a minor effect on the turbine mass flow rate and operating efficiency in comparison with the outlet angle as described in Figure 4.16. It affects the mass flow rate within a range of 1% to 2% depending on the outlet angle. Regarding the operating efficiency, it shows maximum value at  $R_1/R_3$  equal to 2.5.

## 4.5 Spiral casing replacement

After investigating the effect of different geometrical parameters on the performance of the turbine featuring an MC, this section introduces a numerical model that is implemented to replace the spiral casing by an MC

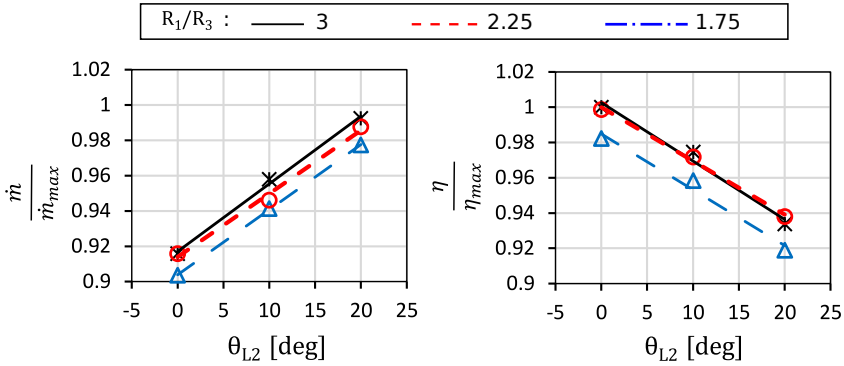
**Table 4.3:** Geometrical parameters for the second group of selected cases

$D_2 = 50\text{mm}$ , $N_{ch} = 5$ , $A_{th} = 73\text{ mm}^2$ , $\theta_{R2} = \theta_{L2} + 20\text{ deg}$ , $A_o/A_{th} \equiv \text{Medium}$			
	$R_1/R_3 = 3$	$R_1/R_3 = 2.25$	$R_1/R_3 = 1.75$
$\theta_{L2} = 0\text{ deg}$			
$\theta_{L2} = 10\text{ deg}$			
$\theta_{L2} = 20\text{ deg}$			

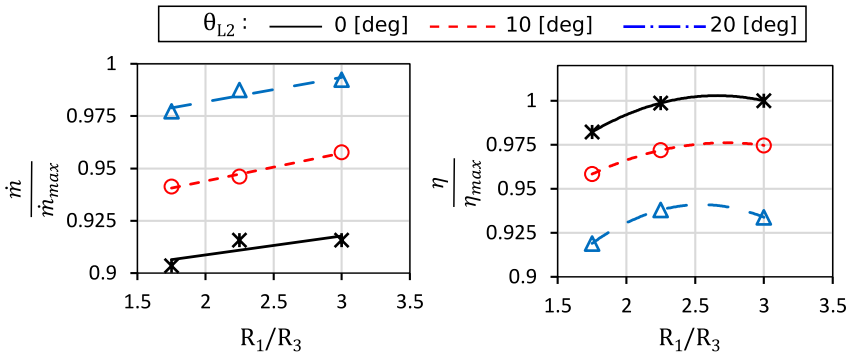
while ensuring a comparable performance. The procedures of this design model are illustrated in the flow chart in Figure 4.17. First, it is initialized with geometrical and performance information of the turbine featuring the original spiral casing as input data. Then, it selects an initial value for the different geometrical parameters to achieve the MC throat area based on the following equation:

$$A_{th, sg}^{MC} = \alpha A_{th}^{sp} / N_{ch} \quad (4.8)$$

where  $\alpha$  is a reduction coefficient equal 0.85 up to 0.97 based on the channel count due to the higher swallowing capacity of the MC compared to the spiral casing as described in Figure 4.7. Then, the design model performs a steady CFD simulation and calculates the turbine performance. The performance of the MC is compared to the spiral casing. Finally, the model updates the design parameters iteratively until achieving the design requirements.

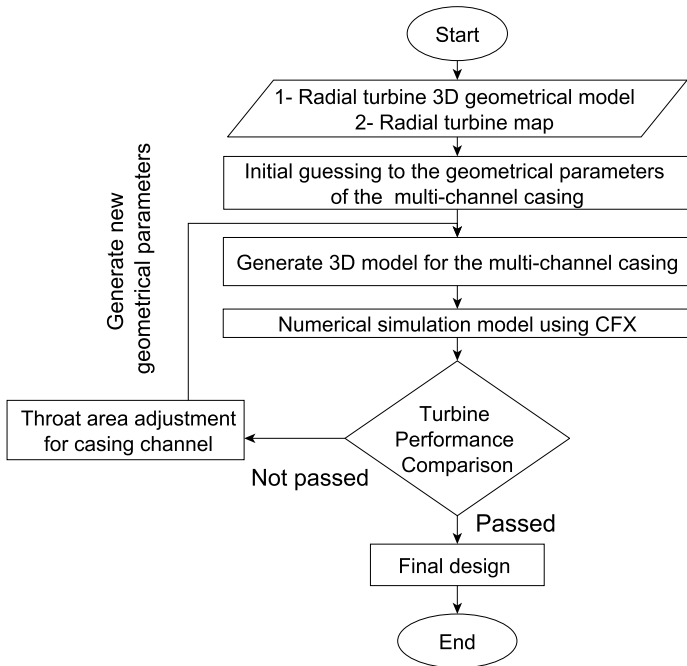


**Figure 4.15:** Effect of the channel outlet angle on the turbine performance, for different casing inlet diameters



**Figure 4.16:** Effect of the channel Inlet diameter on the turbine performance, for different outlet angle

The design procedures and selection of the throat area as control criteria are inspired by the design of the stator vanes in radial turbine applications. Simpson et al. [72] investigated the effect of different stator vanes designs on the turbine performance while ensuring a comparable working capacity by adjusting the throat area of the stator vanes. For MC and stator vanes designs the throat area is adjusted by varying different geometrical parameters which are described in Table 4.1.



**Figure 4.17:** MC casing replacement procedures



# 5 Experimental Work

This chapter presents the experimental tests which were done to examine the turbine performance map and blade vibration for full and partial admission to validate all numerical calculations. All tests took place on the hot gas test stand at the ITSM at the University of Stuttgart.

## 5.1 Test Setup

### 5.1.1 Test Rig

An open-loop hot gas test rig was used to perform the experimental tests. The turbine and the compressor airflow are decoupled, and consequently, the turbine operating range is solely limited to the degree that the compressor operates away from surge. The test rig schematic drawing and its main meters are illustrated in Figure 5.1 and Table 5.1, respectively. Further details about the test rig can be found in Heidinger et al. [32].

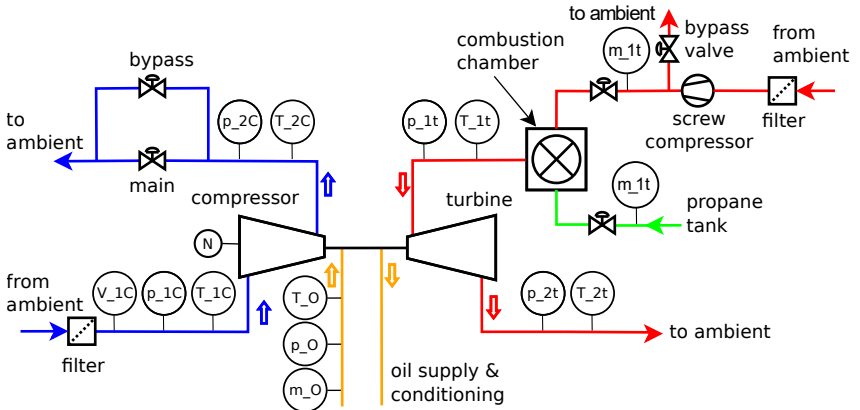


Figure 5.1: Hot gas test rig schematic drawing

**Table 5.1:** Test rig specifications [32]

Property	Quantity			Location
	from	to	Units	
Mass flow rate	0.1	1.2	[kg/s]	
Pressure	1	6	[bar]	CCH outlet
Temperature	300	1473	[K]	CCH outlet
Reproducibility	$\pm 2\%$			For $\dot{m}, T$

### 5.1.2 Turbine casing installation

A five channel casing was designed and manufactured to investigate the performance of the MC experimentally and validate the following numerical studies. The main parts and the dimensions of this casing are illustrated in Figure 5.2.

The casing consists of three main parts: hub cover, shroud cover, and the sealing ring. As an extension to the rotor meridional plane, the hub cover defines the casing hub contour and contains the five channels. The shroud cover defines the shroud contour for both the casing and the rotor besides connecting the inlet pipe to the channels. The sealing ring assembles the previous two parts together by holding the five screw bolts through them. Moreover, two copper gaskets are used to prevent leakage from channel to channel or to ambient.

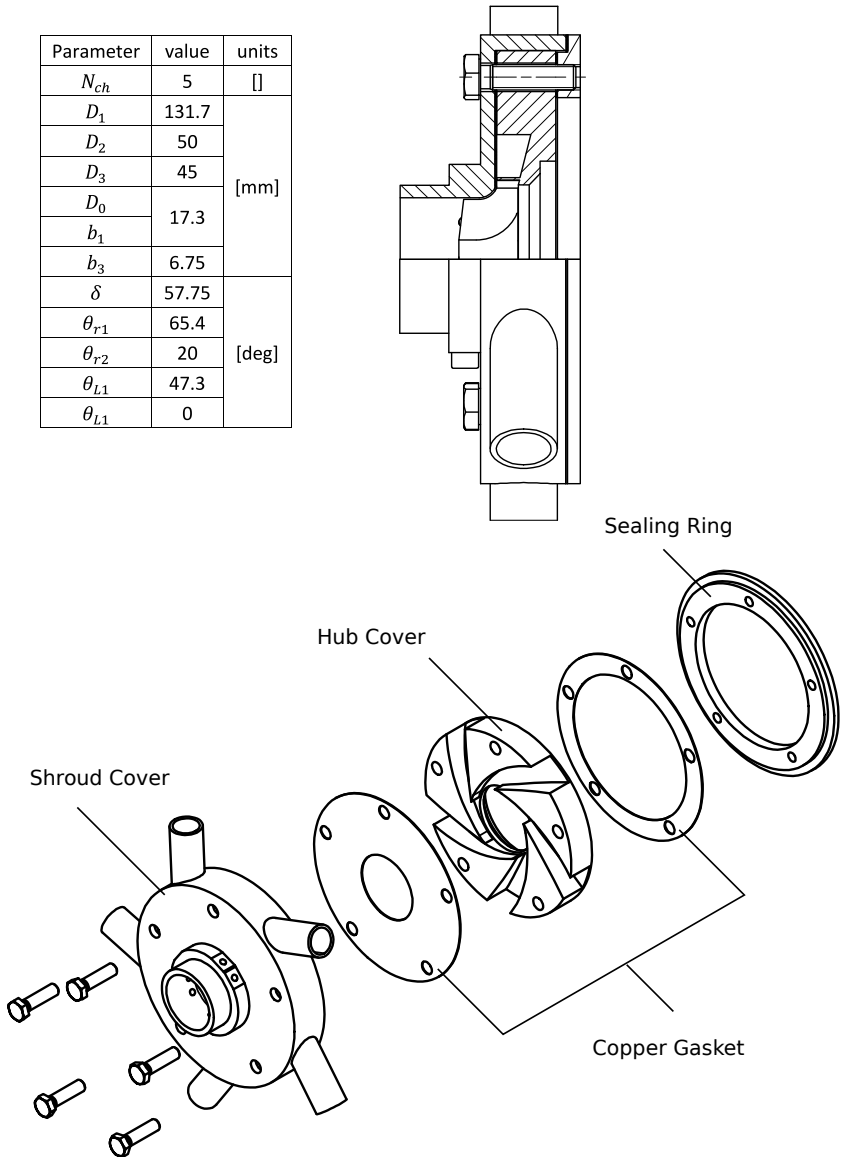
The test rig is modified to test the MC. The combustion chamber (CCH) is coupled with a flow distributor to provide each channel separately with the hot gas. The flow distributor assembly is illustrated in Figure 5.3. This flow distributor contains four wastegate valves to open and close the different flow channels and provide different admission percentages and configurations. One of the distributor channels is kept open for the safety of the test rig.

The flow distributor is connected to the radial turbine of the turbocharger through a set of pipes. The isometric drawing in Figure 5.4 shows the arrangement of these pipes. Four of these pipes are supported with flexible connections while one of them is kept fixed for positioning purposes.

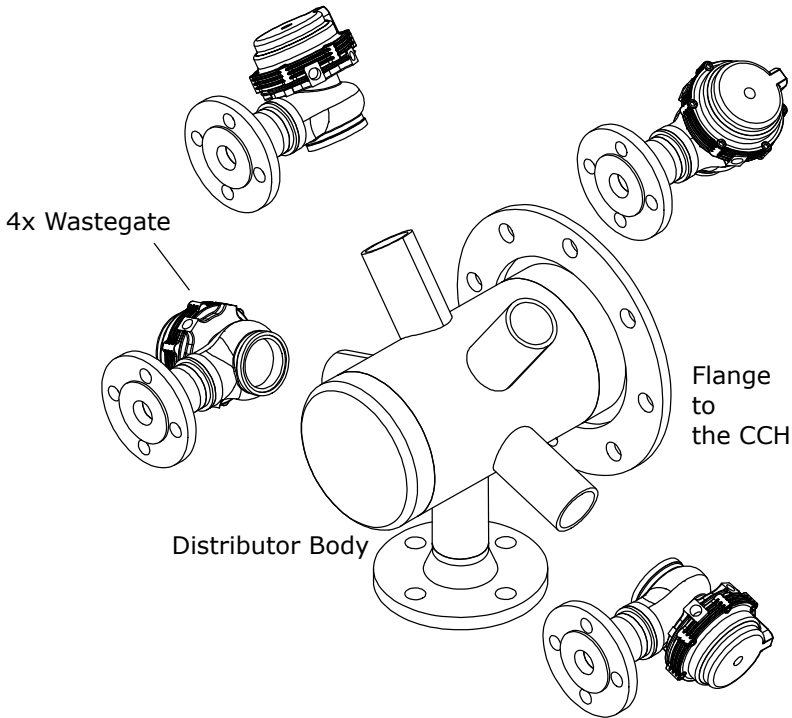
The complete set of detailed drawings of the manufactured components are included in Appendix B.



Parameter	value	units
$N_{ch}$	5	[]
$D_1$	131.7	[mm]
$D_2$	50	
$D_3$	45	
$D_0$	17.3	
$b_1$		
$b_3$	6.75	
$\delta$	57.75	[deg]
$\theta_{r1}$	65.4	
$\theta_{r2}$	20	
$\theta_{L1}$	47.3	
$\theta_{L1}$	0	



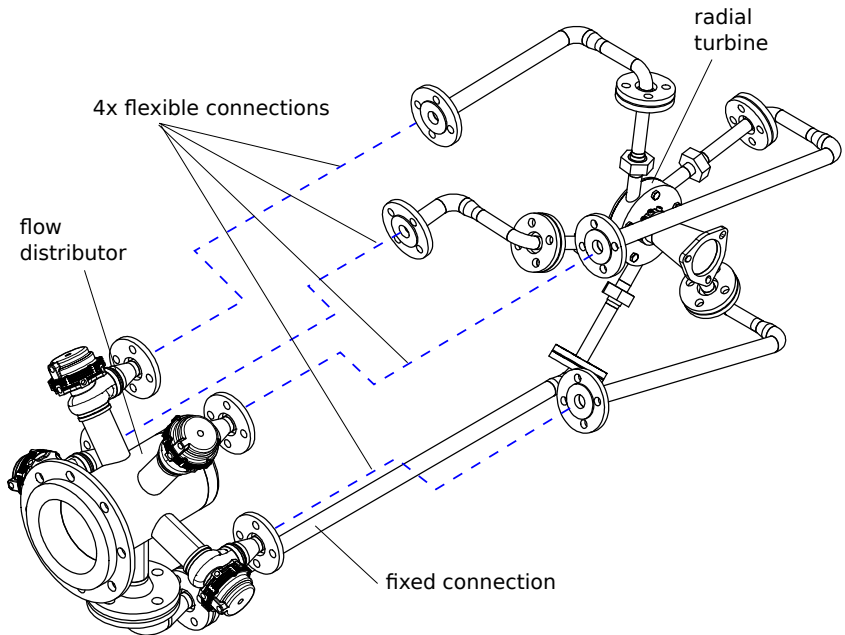
**Figure 5.2:** Turbine MC with 5 channels, Top: half section view - Bottom: Exploded view.



**Figure 5.3:** Flow distributor (Exploded view)

## 5.2 Technical Measurements

This section describes in detail the measurement systems which are used during this study. Two different measurement systems are used to evaluate both the turbocharger performance and the turbine blade vibration. The first system is based on pressure sensors, thermocouples, flow meters, and tachometer. The distribution of these sensors within the test rig is outlined in Figure 5.1. The second system is based on the Blade Tip Timing (BTT) sensors. Both systems are connected to separate Data Acquisition Systems (DAQ) to acquire and store the measured data.



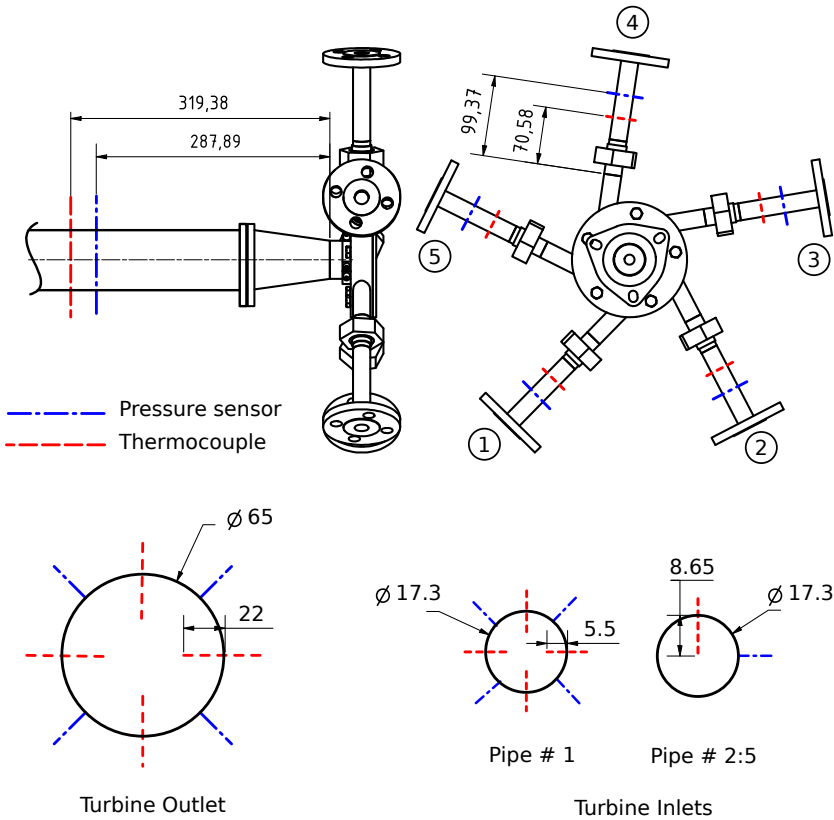
**Figure 5.4:** Radial turbine installation in test rig

### 5.2.1 Turbine performance measurements

This section focuses on the radial turbine stage performance measurements. However, it should not be neglected that the turbine is coupled to the compressor via rotor shaft and that the performance of both components depends on each other. Therefore, the performance of the compressor is monitored with 3 thermocouples and 4 pressure transducers. Moreover, temperatures, pressures, and mass flow of the lubricating oil in the bearing are monitored during the measurements. The oil pressure at the inlet is constantly regulated at 3 bar.

The turbine performance is measured using 12 thermocouples, and 6 pressure sensors. The installation arrangement of these sensors on the turbine inlet and outlet is depicted in Figure 5.5.

To avoid any influence of temperature measurement on the pressure measurement, the pressure measurement location is always arranged upstream



**Figure 5.5:** Pressure and temperature sensors locations

of the temperature measurement location. Conversely, the influences of pressure measurement on temperature measurement are neglected.

All temperatures are measured with type K thermocouples, whereby 1.5 and 3 mm diameters thermocouples are used in the turbine inlet and outlet, respectively. The deviation limits of type K thermocouples according to the manufacture and DIN EN 60 584-2 is  $\pm 1.5$  K for temperatures between  $-40$  °C and  $1000$  °C. The air mass flows at the inlet of the radial turbine stage are measured using Coriolis mass flow meters from “Endress + Hauser Messtechnik GmbH”. These mass flow meters have an inaccuracy of  $\pm 0.35\%$  over

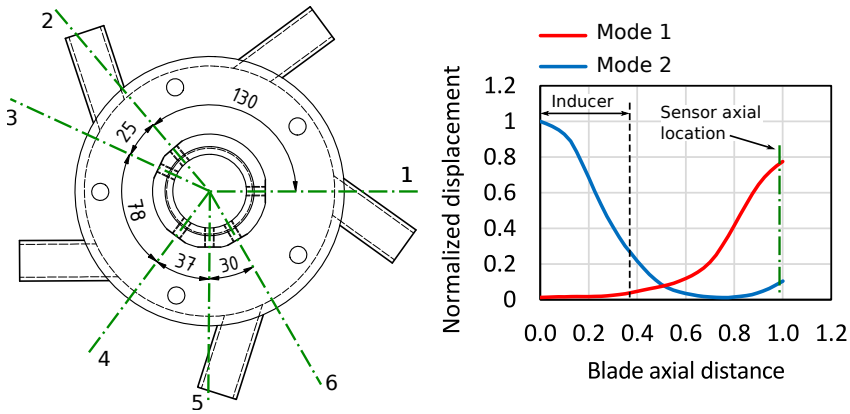
the measuring range. In order to prevent leakage, a leak test was carried out at all connection points in the measuring system of the turbocharger before each series of measurements. The Sitrans P DS III pressure transmitters from Siemens AG are used for the pressure measurement with a measurement error of 0.075%. All pressures are recorded with the same type of pressure transmitters, which differ in their calibrated measuring range.

### 5.2.2 Blade vibration measurements

Blade vibration is measured in this study by means of Blade Tip Timing (BTT). It calculates the blade vibration based on monitoring the time difference between the theoretical and real blade arrival using a special fiber optics sensor. First, this technique was presented in 1974 by Zablotkii [83]. Since this time, many other studies investigated and developed this technique [23, 25, 31, 39, 43, 51, 62, 66, 79, 80].

The BTT sensors are installed in the turbine housing. Each sensor transmits a laser beam towards the turbine rotor. The passing blade reflects the laser beam again towards the sensor which receives and generates an electric pulse by a photo-detector. The electric pulses are generated regularly as the blade passes the sensors and is sent to an Analog-to-digital converter. This converter uses a digital clock to calculate the blade's real arrival time. Deviation from the theoretical arrival time of a blade determines a time delay which is proportional to the blade deflection. The resonance frequency, the order of excitation, and the blade response amplitude are identified by a least-squares sine wave curve fit.

Selecting the count and both axial and circumferential positions of the sensors is done using the sensor placement software [46] by Hood Technology. This software determines the optimum locations for the sensor to distinguish between different orders of excitation and nodal diameters. This selection is based on the mode shape, order of excitation, and the unavailable position on the casing to install the sensor. In the current case, six sensors are placed on the same selected axial position and different circumferential positions in order to accurately measure the first bending mode as plotted in Figure 5.6.



**Figure 5.6:** BTT sensor position, left: Circumferential - Right: Axial

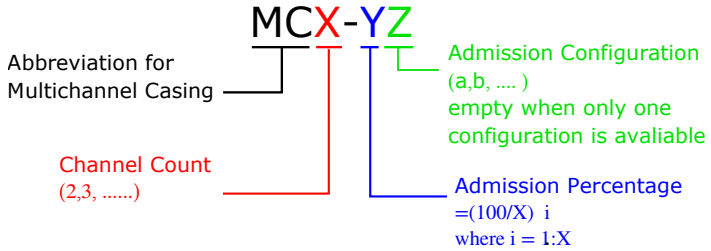
### 5.3 Turbine Performance

The first set of tests aims to measure the turbocharger performance focusing on the radial turbine side. The turbine performance is evaluated through plotting the turbine reduced mass flow characteristics and its operating efficiency for different admission configurations and different operating temperatures. The performance of the turbine featuring a five-channel casing is also compared to the previously tested spiral and four-channel casing.

To present the multi-channel casing operating conditions, a unified code is used. It represents the casing channel count, admission percentage, and admission configuration as describe in Figure 5.7.

The arrangement of the closed and opened channels is called the admission configuration, and the ratio between the counts of the open channels to the total number of channels is called the admission percentage. For instance, MC5-60a is a five-channel casing operated at 60 percent admission by closing two channels for the first admission configuration. The admission percentages and configurations for different are described in Table 5.2 for five and four channels casing.

The performance of the radial turbine featuring the five-channel casing is tested at full admission for different turbine inlet temperatures and rota-



**Figure 5.7:** Multi-channel casing unified symbol

**Table 5.2:** MC different admission percentage and configuration

$N_{ch} = 5$							
Case	Inlet					Admission	
	1	2	3	4	5	Percentage	Configuration
1	o	o	o	o	o	100	MC5-100
2	o	x	o	o	o	80	MC5-80
3	o	x	x	o	o	60	MC5-60a
4	o	x	o	x	o		MC5-60b
5	o	x	x	x	o	40	MC5-40a
6	o	x	x	o	x		MC5-40b
7	o	x	x	x	x	20	MC5-20
$N_{ch} = 4$							
Case	Inlet					Admission	
	1	2	3	4		Percentage	Configuration
1	o	o	o	o		100	MC4-100
2	o	x	o	o		75	MC4-75
3	o	x	x	o		50	MC4-50a
4	o	x	o	x			MC4-50b
5	o	x	x	x		25	MC4-25

o ..... inflow condition  
x ..... wall condition

tional speeds. It is assessed based on plotting the reduced mass flow rate and the operating efficiency versus the total to static expansion ratio.

The total to static expansion ratio is defined as the ratio between total pressure at the turbine inlet to static pressure at the turbine outlet. The total pressure at the turbine inlet is calculated as [77]:

$$p_{t1}^t = p_1^t \left(1 + \frac{v^2}{2c_p^t T_1^t}\right)^{\left(\frac{\gamma}{\gamma-1}\right)} \quad (5.1)$$

where  $p_1^t$  is the measured static pressure at the turbine inlet,  $T_1^t$  is the averaged measured total temperature at the turbine inlets, and  $v$  is the flow velocity at the turbine inlet which is calculated as:

$$v = \dot{m}^t \frac{RT_1^t}{p_1^t} \quad (5.2)$$

The turbine efficiency is evaluated by calculating the Thermo-mechanical efficiency using the following definition:

$$\eta^t \eta^m = \frac{\eta^{tc}}{\eta^c} \quad (5.3)$$

where,  $\eta^{tc}$  and  $\eta^c$  are turbocharger and compressor efficiency, respectively and calculated as [77]:

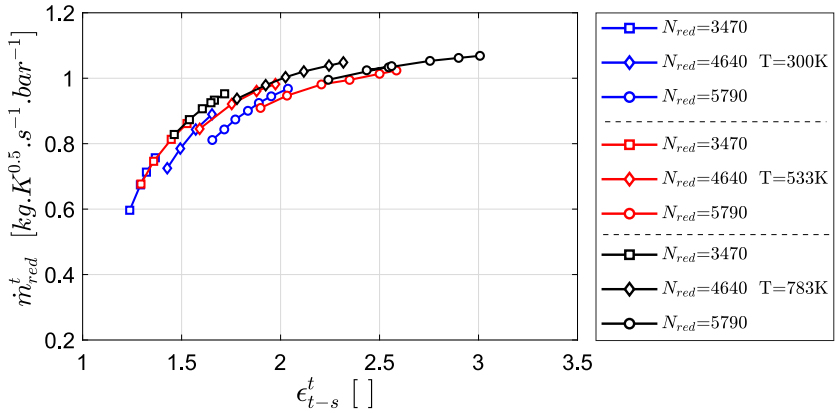
$$\eta^{tc} = \frac{\dot{m}^c c_p^c T_{in}^c \pi^c \left(\frac{\gamma^c-1}{\gamma^c}\right) - 1}{\dot{m}^t c_p^t T_{in}^t \pi^t \left(\frac{\gamma^t-1}{\gamma^t}\right) - 1} \quad (5.4)$$

$$\eta^c = \frac{\pi^c \left(\frac{\gamma^c-1}{\gamma^c}\right) - 1}{\frac{T_{out}^c}{T_{in}^c} - 1} \quad (5.5)$$

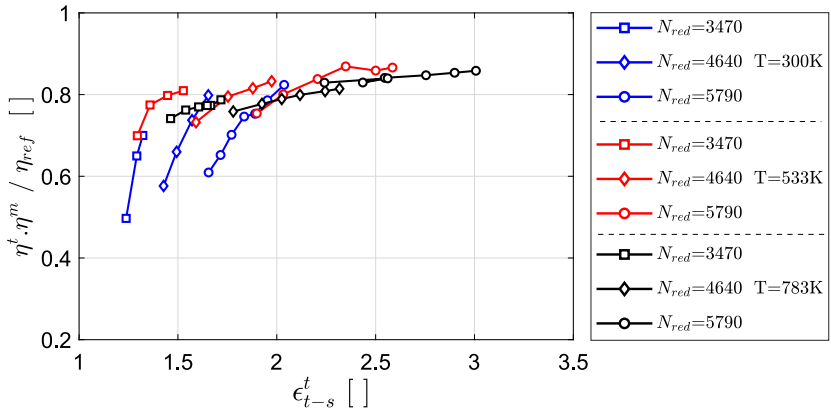
where,  $\pi^c$  and  $\pi^t$  are compressor and turbine pressure ratios, respectively. The thermo-mechanical efficiency definition is used to avoid using the temperature at the turbine outlet which is difficult to be measured accurately. This is due to the heat transfer from upstream the turbine when operating in the hot conditions and the complex flow field downstream the turbine [85]. Turbine reduced mass flow and operating efficiency are plotted in Figures 5.8 and 5.9, respectively.

After testing the turbine at full admission, different admission percentages are tested for cold and hot operation. Turbine reduced mass flow rate and efficiency for the cold operation (at T=300K) are shown in Figures 5.10 and





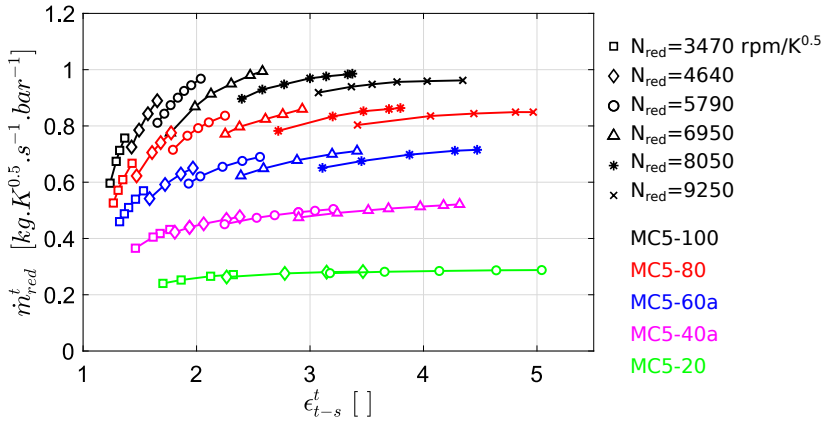
**Figure 5.8:** Turbine reduced mass flow rate at different inlet temperature, MC5-100



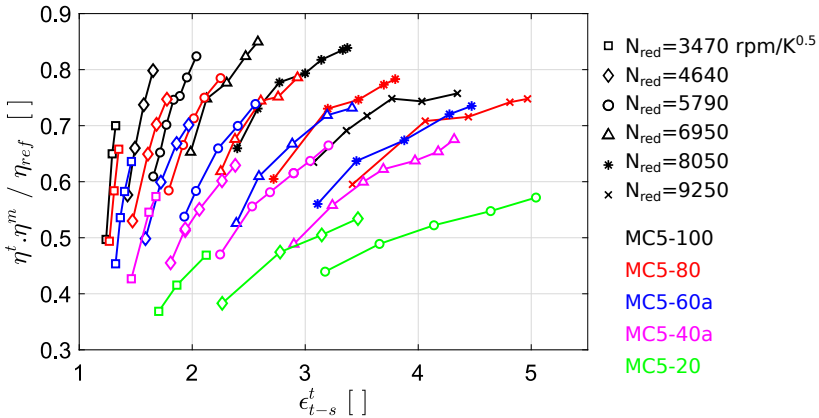
**Figure 5.9:** Turbine efficiency at different inlet temperature, MC5-100

5.11, respectively. Results for the hot operation (at T=783K) are shown in Figures 5.12 and 5.13, respectively.

The compressor mass flow characteristics and operating efficiency are plotted in Figures 5.14 and 5.15, respectively, for three different admission percentages. The compressor performance is plotted for a rotational speed range between 60.000 rpm and 160.000 rpm using six speed lines. The compressor performances are identical for all admission percentages,



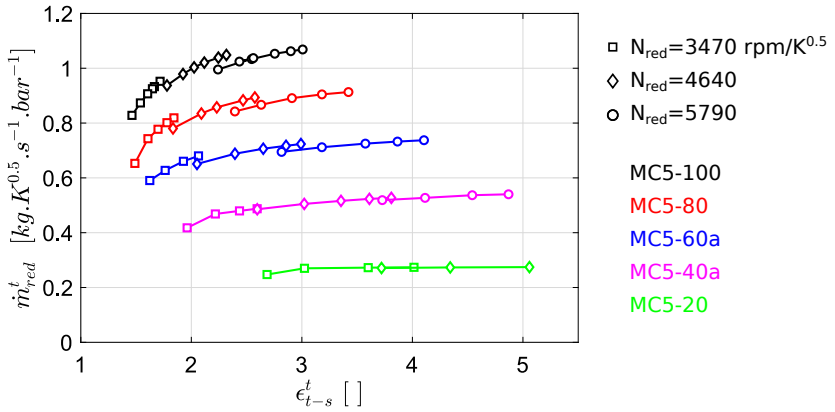
**Figure 5.10:** Turbine reduced mass flow rate at different admission percentage,  $T=300K$



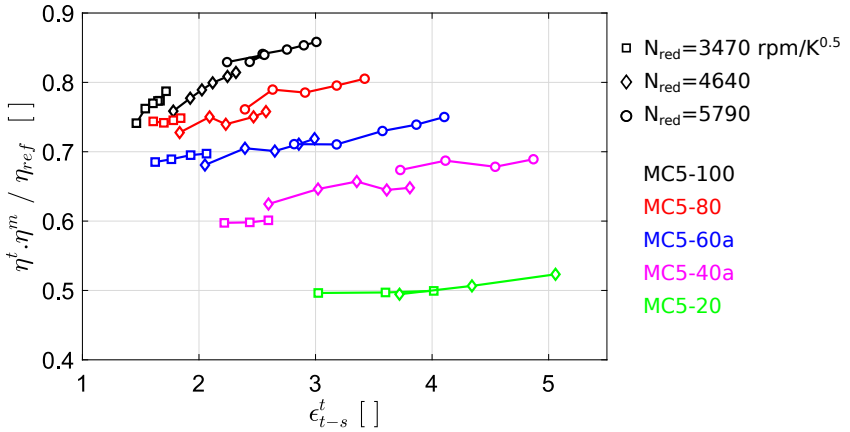
**Figure 5.11:** Turbine efficiency at different admission percentage,  $T=300K$

which shows that the turbine concept and different admission ratios have no influence on the compressor performance.

To ensure the reproducibility of the measurement, the turbine performance test is repeated for selected admission configurations and rotational speeds. These sets of measurements were done on three different days and by three



**Figure 5.12:** Turbine reduced mass flow rate at different admission percentage, T=783K



**Figure 5.13:** Turbine efficiency at different admission percentage, T=783K

different operators. The results of these repeated tests are shown in Figures 5.16 and 5.17, respectively.

The results demonstrate reliable mass flow rate measurements with an average deviation lower than 1% for different operating speeds and admissions. Regarding the turbine efficiency, the results show acceptable repeatability

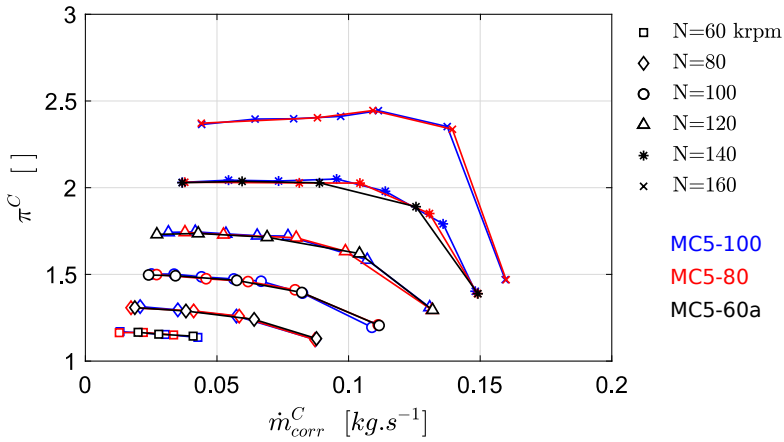


Figure 5.14: Turbocharger compressor map

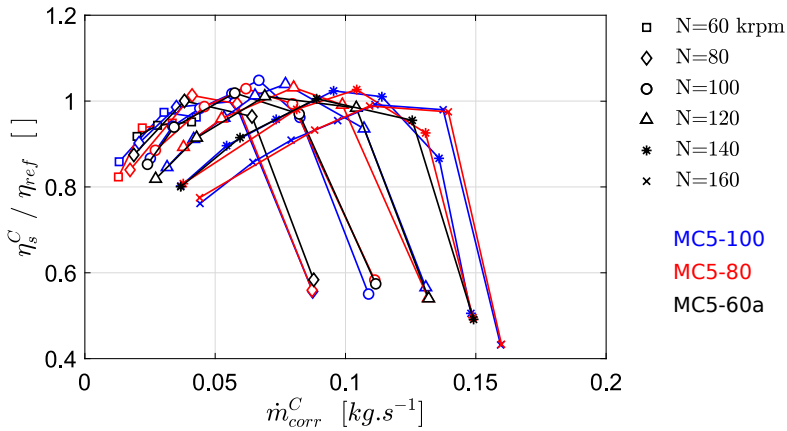
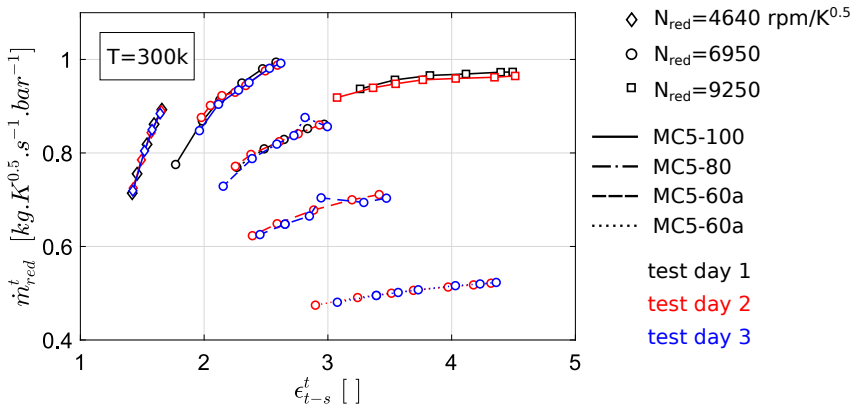
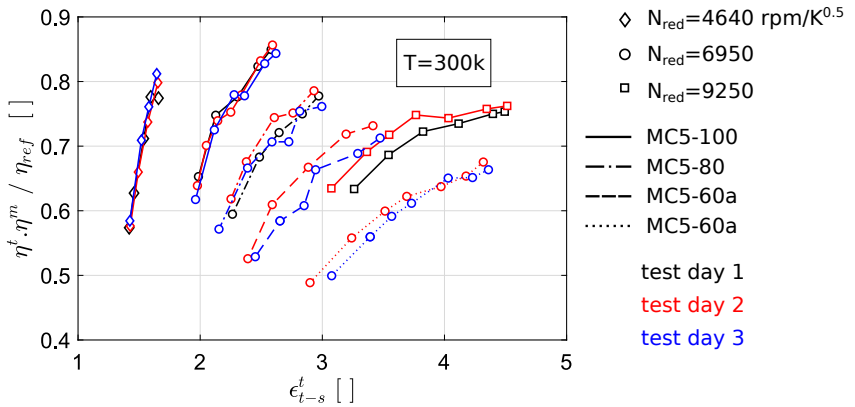


Figure 5.15: Turbocharger compressor isentropic efficiency

with an average deviation of 3%. Knowing that, the accuracy of the efficiency measurements lies in the difficulty to accurately measure the temperatures in such highly non-uniform flow fields as present here. Therefore these test data can be used for the CFD validation.



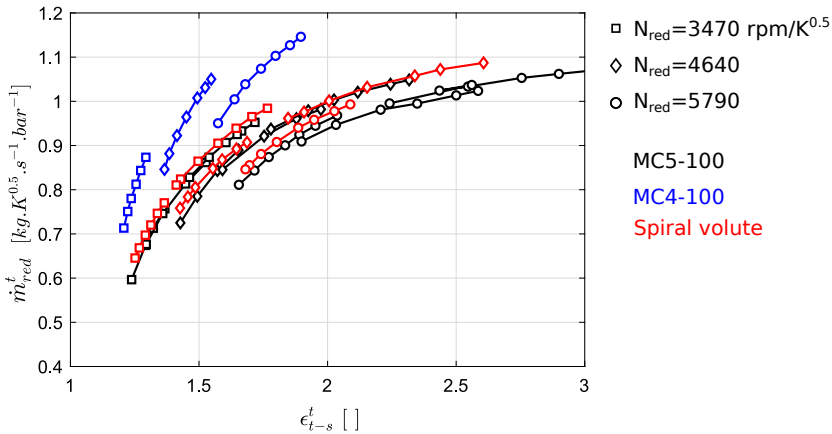
**Figure 5.16:** Mass flow measurement repeatability for selected rotational speed and admission percentage



**Figure 5.17:** Efficiency measurement repeatability for selected rotational speed and admission percentage

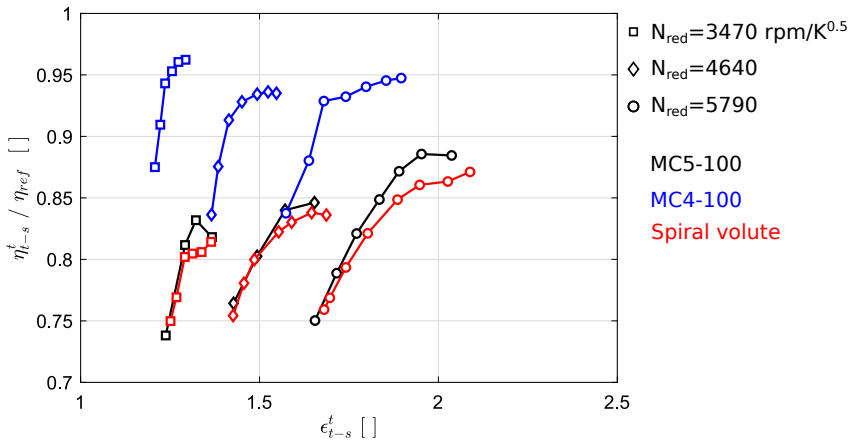
The tested mass flow and efficiency of the turbine featuring five-channel casing are compared to the same turbine but featuring a traditional spiral casing. Besides, they are compared to the first MC prototype which featured a four-channel casing and was tested by Ilievski in 2017 [36].

Figure 5.18 presents the reduced mass flow rate of the investigated turbine for different casing: the original spiral casing with a completely closed wastegate, MC5-100, and MC4-100. It confirms that the four-channel casing has higher mass flow characteristics compared to the original spiral casing. This difference is considered in designing the second MC prototype (with five channels). A new design model is used to achieve a comparable mass flow characteristics as described in Chapter 4. The turbine featuring five-channel (MC second prototype) shows comparable mass flow rate characteristics with an average deviation lower than 1% as shown in the same figure. This proves that the developed design model is able to replace the spiral casing by an MC and keeps a comparable turbine mass flow characteristics.



**Figure 5.18:** Turbine reduced mass flow rate for different casing types, Full admission

The turbine operating isentropic efficiency for the three different cases is shown in Figure 5.19. Although MC4-100 shows a higher efficiency compared to the original spiral casing, no conclusion can be drawn because of the high difference in the operating mass flow rate. In contrast, the efficiency of the spiral volute and the MC5-100 can be compared. It shows that the MC5-100 has a slight increase in efficiency at the BEP which can reach 1.5 % at a high rotational speed. This observation totally agrees with the numerical study which was discussed in Chapter 4 about the effect of different channel count on the turbine efficiency as shown in Figure 4.8.



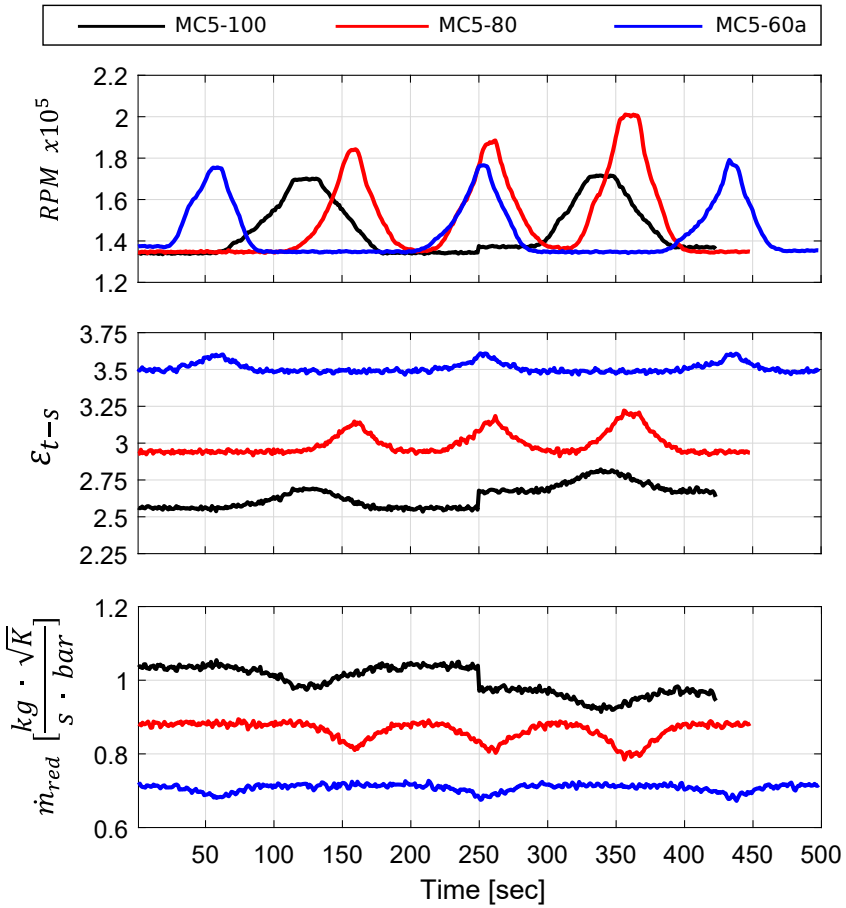
**Figure 5.19:** Turbine isentropic efficiency for different casing types, Full admission

## 5.4 Blade Vibration

Six optical sensors are circumferentially placed on the turbine casing to measure the blade vibration as described in Figure 5.6. Within the turbine operating range, the turbine rotor is expected to be at resonance at 118k, 136k, and 159k rpm according to EO8, EO7, and EO6, respectively as described in Figure 6.16. In order to test the vibration amplitude at these positions, the turbine is operated at different speed ramps to excite the blade at the mentioned rotational speeds. These speed ramps are achieved by controlling the compressor inlet area at a specific operating point. A samples of these speed ramps at EO6 for different admission configurations are shown in Figure 5.20 including the change in the expansion ratio and mass flow rate during increasing and decreasing the rotational speed.

The vibration amplitude for the eleven blades is measured during each speed ramp to ensure the measurement repeatability. A sample for the measured data for the first speed ramp is plotted in Figures 5.21, 5.22, and 5.23 for EO6, EO7, and EO8 respectively for three different admission configurations.

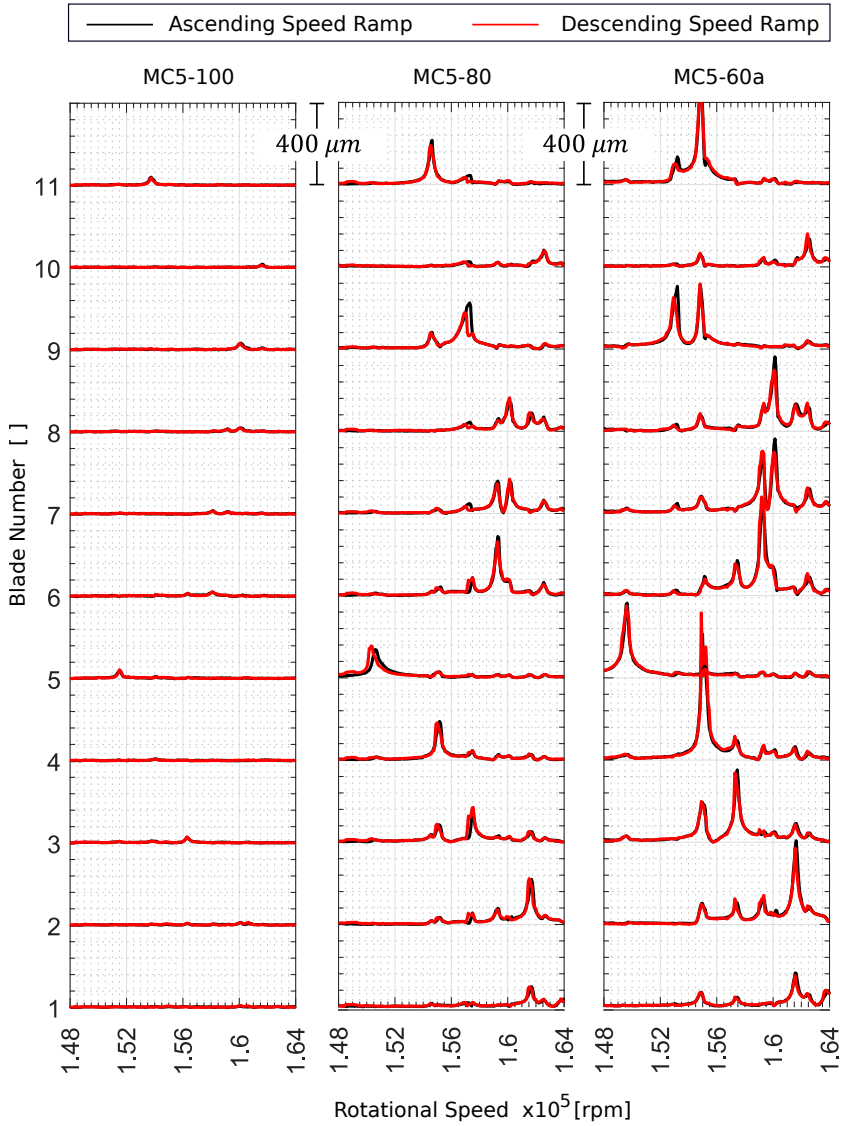
The median value of the vibration amplitude, damping ratio, and critical speed is calculated for different blades and different speed ramps to present

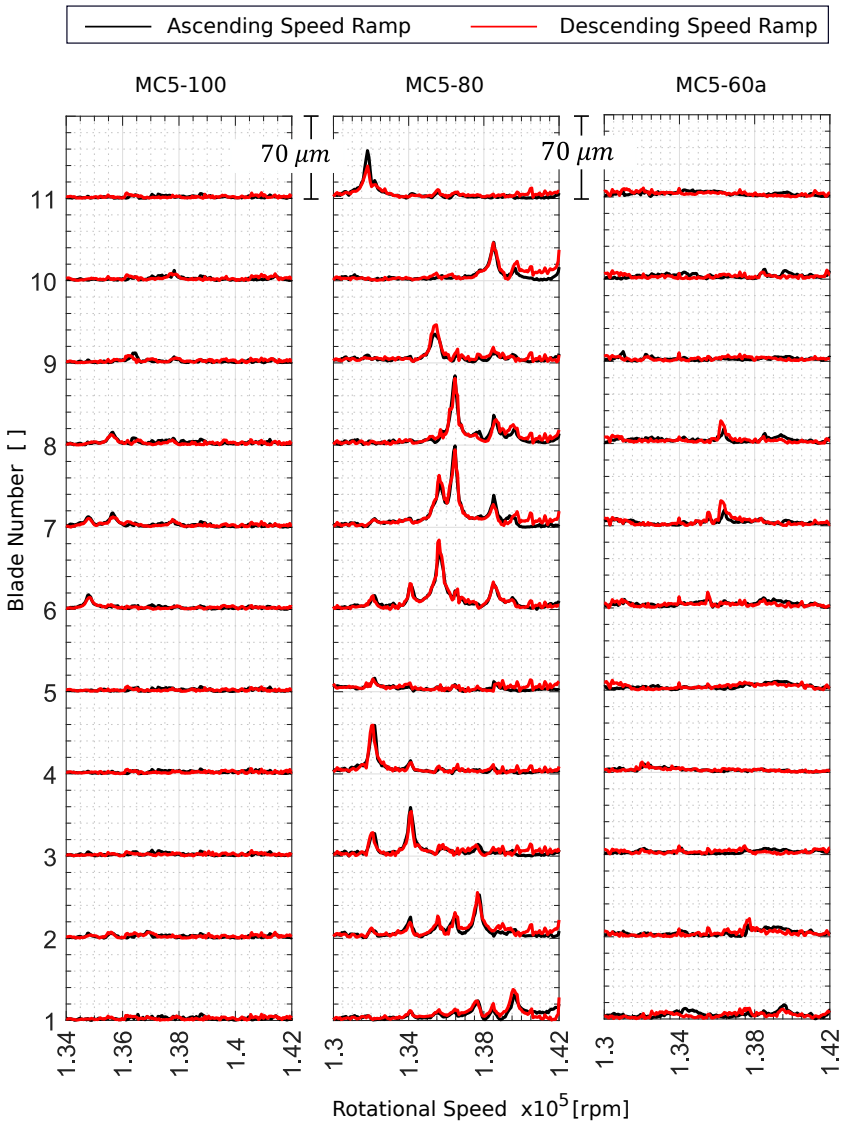


**Figure 5.20:** Speed ramp for different admission configurations, EO6

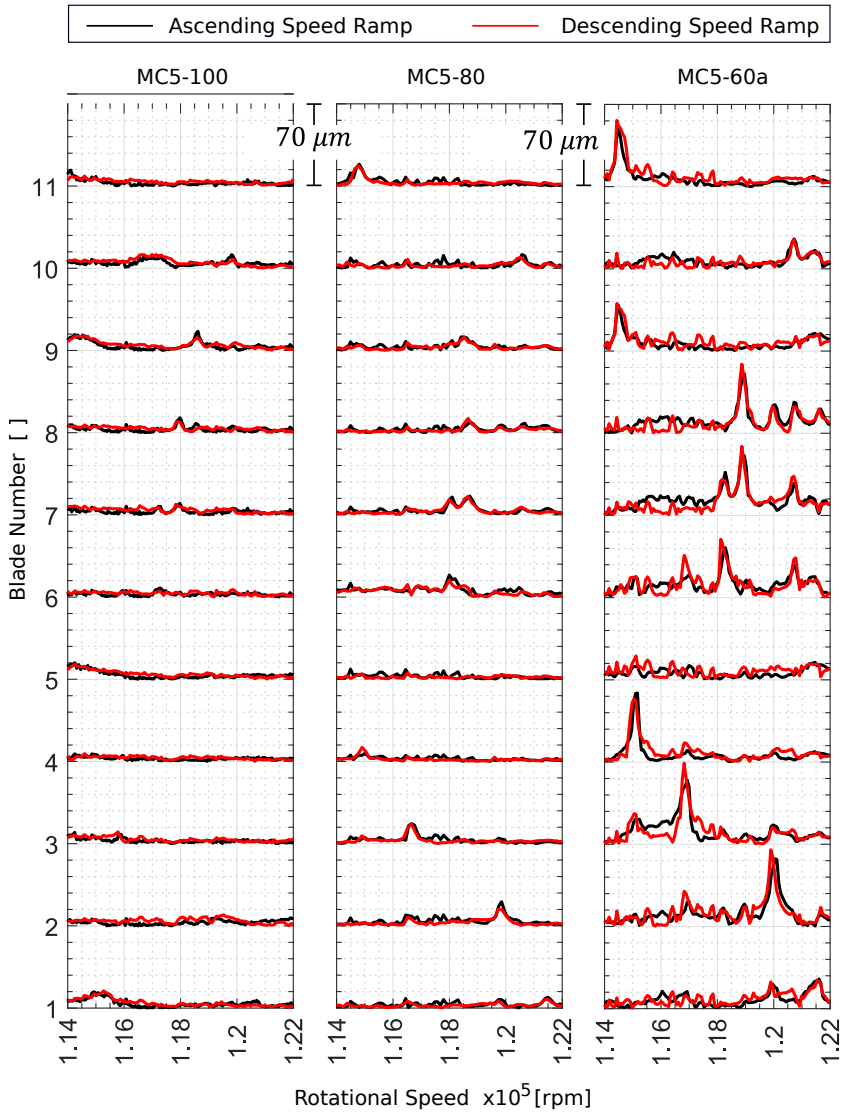
the vibration amplitude for different admission configurations as shown in Figure 5.24 and Table 5.3.



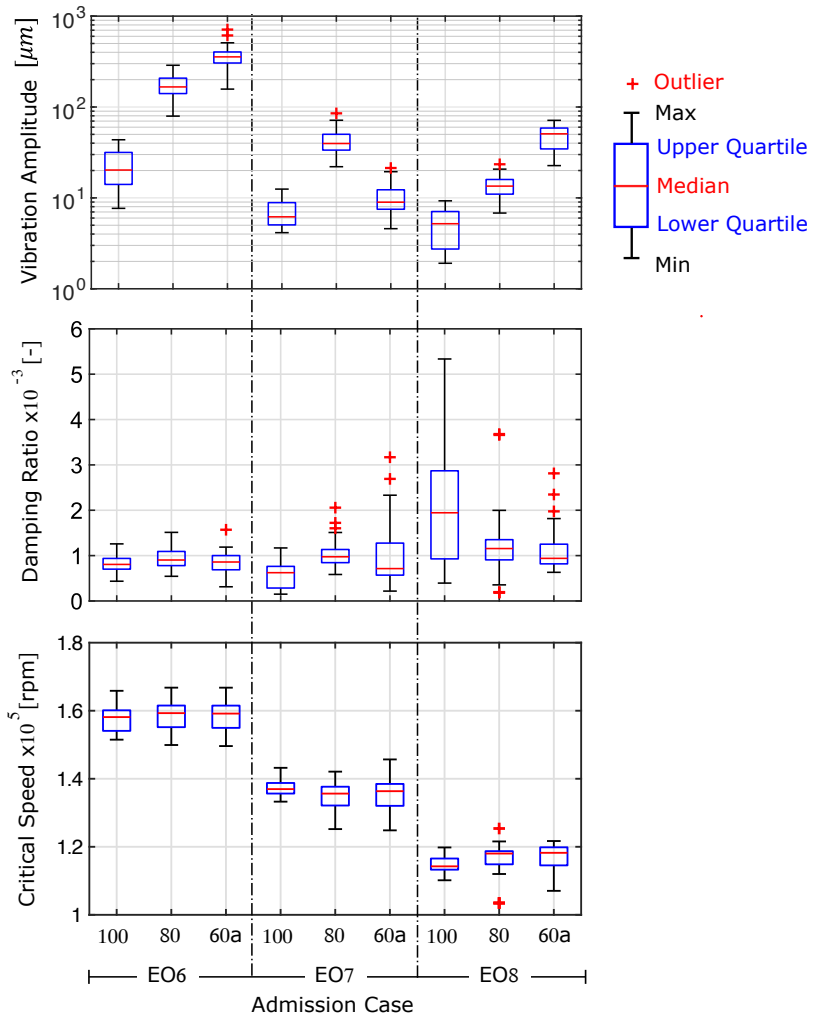
**Figure 5.21:** Blade vibration amplitude, EO6



**Figure 5.22:** Blade vibration amplitude, EO7



**Figure 5.23:** Blade vibration amplitude, EO8



**Figure 5.24:** Blade vibration data for different EOs and admission configurations

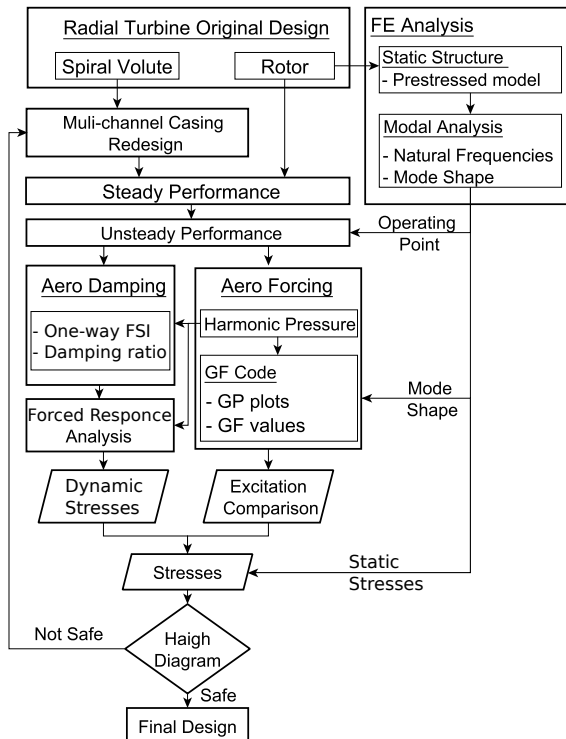
**Table 5.3:** Blade vibration data (Median values)

Quantity		EO6			EO7			EO8		
		Admission Configurations								
		100	80	60a	100	80	60a	100	80	60a
Vibration Amplitude	$[\mu m]$	20.3	166.3	356.3	6.2	39.6	9.0	5.2	13.5	50.7
Damping Ratio $\times 10^{-4}$	$[-]$	8.06	9.03	8.59	6.23	9.74	7.14	19.4	11.6	9.39
Critical Speed	$[krpm]$	158	159	159	137	136	136	114	118	118



## 6 Numerical Study

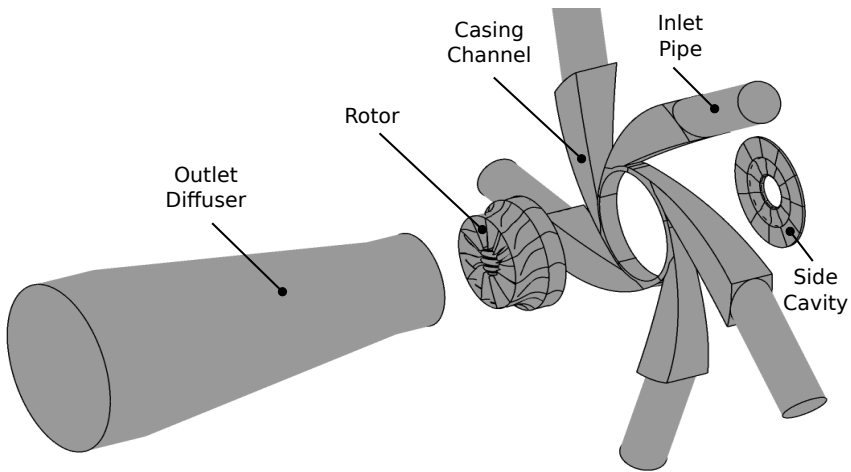
To design an MC and assess its performance and reliability, different numerical models are implemented including fluid, structure and fluid-structure interaction models. The integration between these models is represented in the flowchart in Figure 6.1. This chapter discusses in detail all these models and how their results are processed and combined to achieve the goals of this study.



**Figure 6.1:** MC casing design and assessment process

## 6.1 Fluid Model

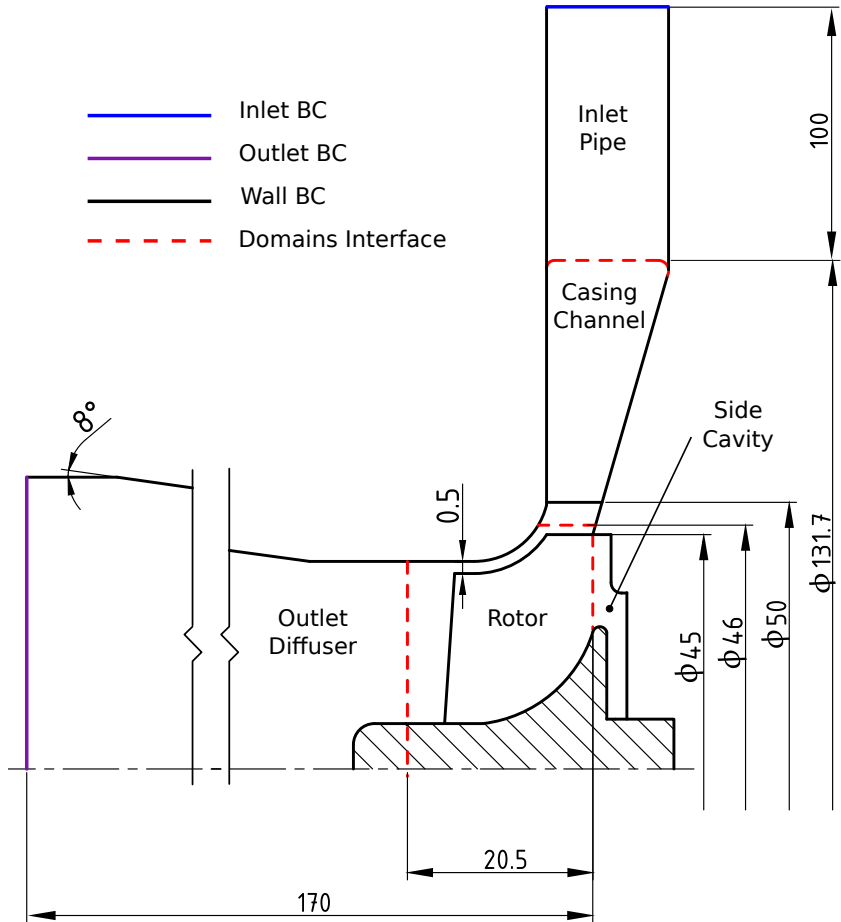
Computational Fluid Dynamic (CFD) model is implemented to solve the flow inside the radial turbine. The entire turbine domains are considered including inlet pipe, casing channel, rotor, side cavity, and outlet diffuser as shown in Figure 6.2. The side cavity is considered to have a noticeable effect on both steady and unsteady performance especially in case of a deeply scalloped rotor as reported by He et al. [30]. Therefore it is considered in the numerical simulation although it increases the model complexity and the computational time. These domains are spatially discretized and the RANS equations are solved through each control volume in these domains using ANSYS CFX 19.2.



**Figure 6.2:** Radial turbine featuring five channel casing CFD domains

The main metrics of the computational domains are presented in Figure 6.3. The rotor is simulated in a rotating frame of reference, while all other domains are simulated in a stationary frame. The interface between the rotating side and the fixed side is chosen as a mixing plan with an average velocity in case of steady simulation and sliding mesh in case of unsteady simulation. Moreover, the interface between any fixed domain is chosen as a general connection with the wall overlap condition.





**Figure 6.3:** CFD domains main metrics

The  $k-\omega$  SST turbulence model with scalable wall functions is used in this study. The use of this turbulence model has proven to be adequate, as in the related research by [6, 11, 12]. The equations for turbulence modeling were discretized in the first order. Air was used as the flow medium with modeled specific heat constant  $C_p$  as a function of the pressure and temperature.

### 6.1.1 Boundary Condition

For steady and unsteady simulations, total temperature and total pressure at the inlets of the casing channels with 5% turbulence intensity and averaged static pressure at the turbine outlet is chosen as boundary conditions. Different operating expansion ratios are achieved by varying the total pressure value at the inlet while keeping the outlet static pressure constant at 100 kPa. To apply partial admission conditions, the flow condition at some of the casing inlet are changed from inflow to wall to achieve the required admission percentage and configuration. The boundary conditions at casing inlet are described in Table 5.2 for five and four channels casing.

Admission percentage is the ratio between the counts of the open channels to the total number of channels while the admission configuration is the arrangement of the closed and opened channel.

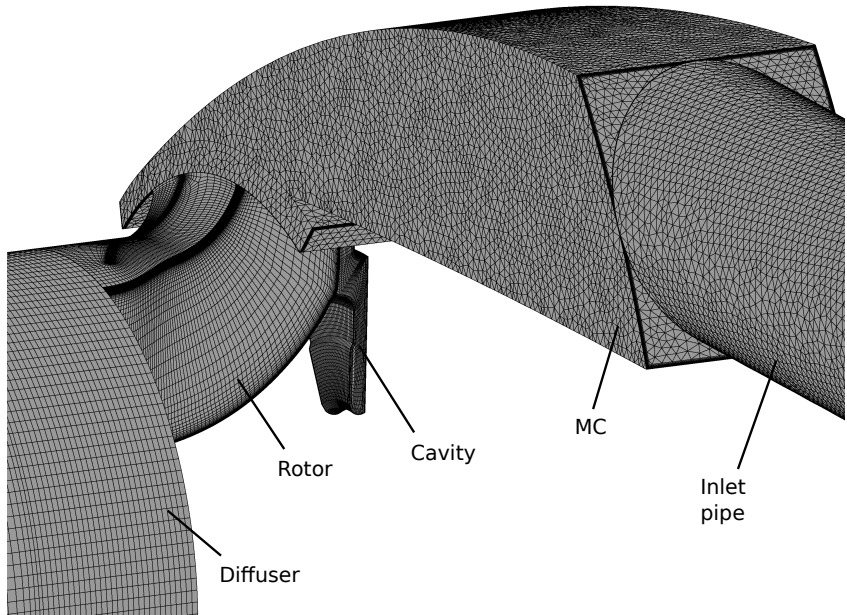
### 6.1.2 Domains Grid and Sensitivity Study

All turbine domains except the MC domains are meshed in a structured manner using TurboGrid for the rotor domain and ICEM for the other domains. The MC domains (casing, and inlet pipe) are meshed in an unstructured manner to facilitate the model automation. The CFD domains meshes are shown in Figure 6.4 and the mesh topology at the meridional surface and its transition between different domains are presented in Figure 6.5.

To minimize the discretization error, a mesh sensitivity study is performed to determine the effect of the grid size on the computational accuracy and cost. The grid sizes of different test cases are listed in Table 6.1. For all test cases, the first element distance from the wall is kept constant for different grid sizes to achieve a  $y^+$  value around 1. Whereas, a finer mesh is achieved by increasing the element count between different walls surfaces.

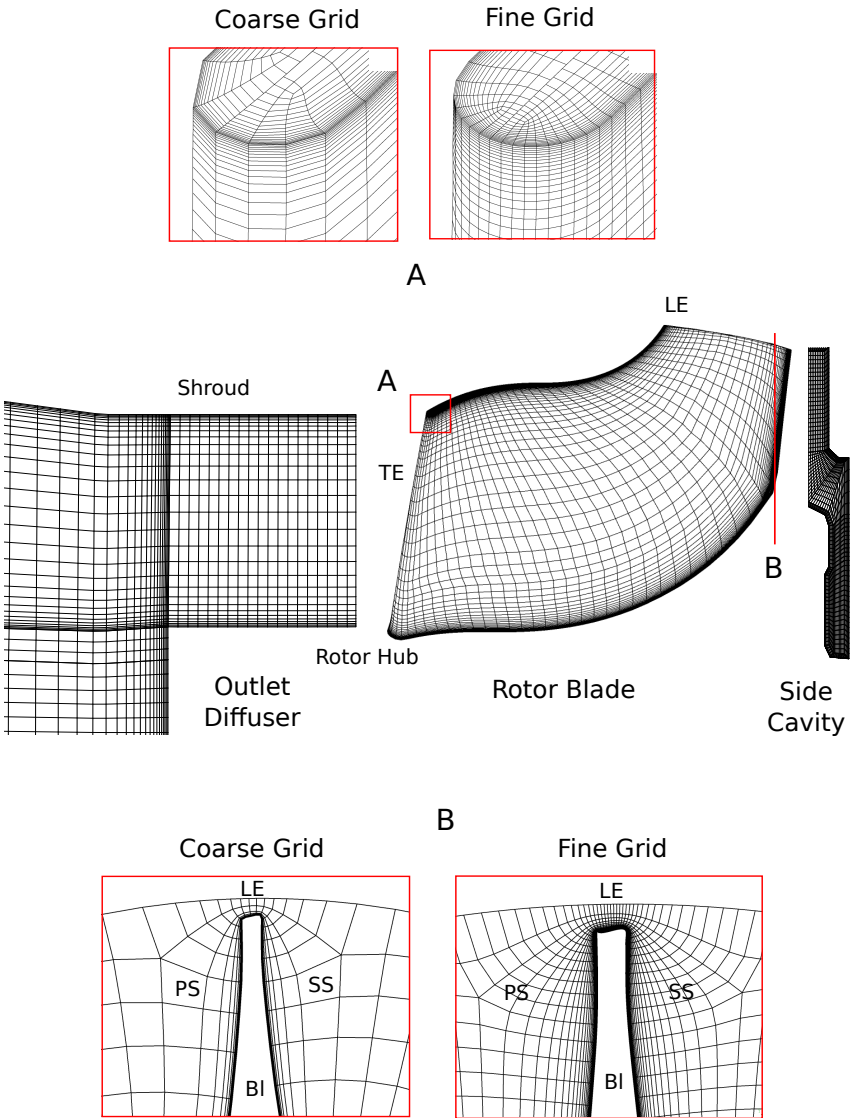
**Table 6.1:** MC mesh element count

Size	Element Count in Million					Total	
	Inlet pipe	Casing channel	Rotor	Side cavity	Outlet diffuser	sector	Full
Coarse	0.08	0.16	0.18	0.03	0.12	0.57	3.48
Medium	0.15	0.25	0.37	0.05	0.3	1.12	6.92
Fine	0.3	0.6	0.62	0.1	0.66	2.64	13.1
Very fine	1.25	2.45	3.1	0.5	1.8	9.1	59.9

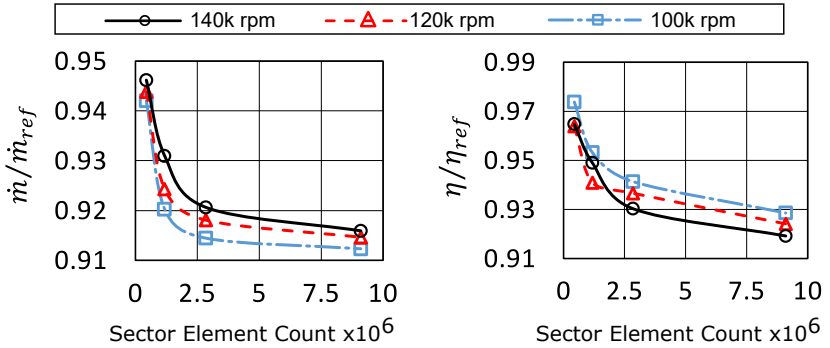


**Figure 6.4:** CFD domains mesh, one-sector model

The turbine operating mass flow rate and efficiency at BEP for different rotational speeds are plotted versus the grid sizes in Figure 6.6. For cases with element count lower than 2.5 million elements in one-sector model, the mass flow rate and efficiency are highly affected by the element count with an average percentage of 2.5% and 4% respectively. The very fine mesh model shows a low change in mass flow rate and efficiency compared to the fine model with an average of 0.5% and 0.9% respectively, while the computational time increases approximately 4 times. Therefore, this study will be conducted by the fine scheme with approximately 2.5 M elements for a one-sector model and 13 M elements for the full model. In total, 75 cell layers are imposed in the span-wise direction, including 20 layers to model the tip clearance. These layers count in the tip clearance region is enough to capture the leakage flow as was discussed by Müller et al. [55]. The maximum cell expansion ratio is limited to 1.2 for all wall surfaces.



**Figure 6.5:** MC CFD domains mesh topology at meridional plan



**Figure 6.6:** Mass flow rate and efficiency for different mesh size, CFD steady

### 6.1.3 Unsteady simulation

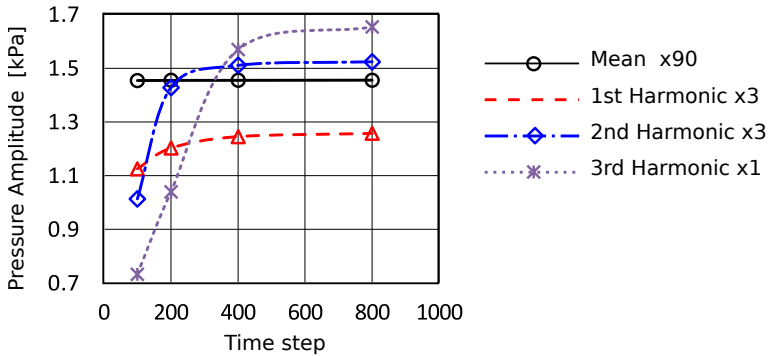
Turbine unsteady flow simulation is crucial to explain the effect of replacing the spiral casing by a MC on many radial turbine design requirements including the performance at full and partial admission and the dynamic loads. The unsteady simulation considers the same computational domains which were mentioned in the steady simulation but expands it to a full 3D model. The interface between the rotating and the fixed frame of references is changed to be sliding mesh with 360 timesteps per complete rotor cycle.

#### Time Step Sensitivity Study

The number of time steps per complete rotor cycle is chosen based on a time step sensitivity study. This study examines the effect of different time step widths on the harmonic component of the pressure at the rotor blade as shown in Figure 6.7. This figure shows that the amplitude of the third harmonic pressure component (E012) is stabilized when the time step reaches 360-time steps per one complete rotor cycle. Therefore, the time step is chosen to be 360 for the unsteady simulation.

### 6.1.4 CFD Model Results and Validation

The mass flow characteristics for a turbine featuring a five-channel MC at cold and hot operation and for different admission configuration is plotted

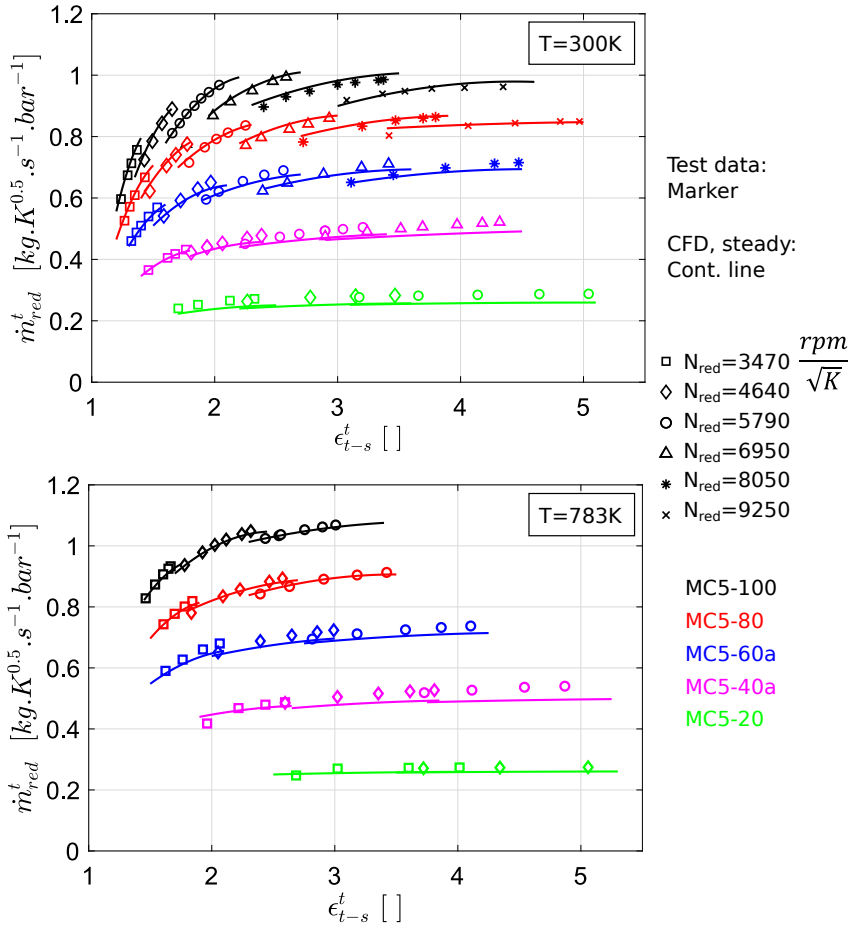


**Figure 6.7:** pressure amplitude for different time step, CFD unsteady

in Figure 6.8. This figure compares the steady CFD results with the test data in order to validate the CFD model. The average deviation of the reduced mass flow between the CFD and test data is lower than 1% for the full admission cases. By decreasing the admission percentage the average deviation slightly increases especially at high expansion ratio. This is due to the flow unsteadiness at the partial admission operation. In general, the CFD model is representative of the tested cases.

After validating the MC CFD model using a five-channel casing, the internal flow field for different casings of the same size is investigated. The static pressure at the turbine stage mid-span and the same operating point ( $N_{red} = 5790 \text{ rpm}/K^{-0.5}$ ) are plotted for different casings as shown in Figure 6.9. The internal flow structure is affected by the casing shape and channel count in the case of MC. At the radial gap region, the static pressure has one local maximum position near the spiral casing tongue, while it has multiple local maximum positions in the case of an MC equal to the channel counts. This change in the internal flow structure affects many RT design aspects such as the operating efficiency and the blade aerodynamic excitation and damping, especially when applying the a partial admission in case of MC design.

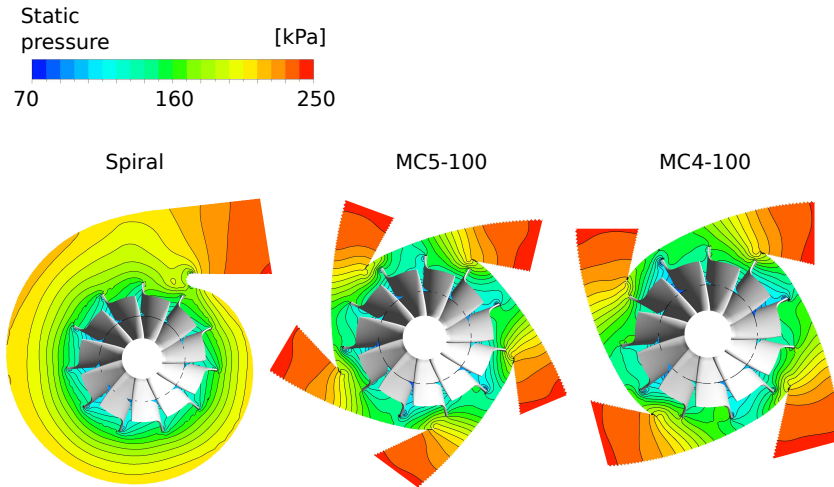
The effect of replacing the spiral casing with an MC on the mentioned RT design aspect is considered in detail in the following chapters. To ensure a comparable operating condition for all studied models for meaningful comparison, the time-averaged pressure at different locations is compared for different casing types after achieving a comparable mass flow conditions.



**Figure 6.8:** Turbine mass flow characteristics for different admission configuration, CFD steady and test data, five-channels casing

Figure 6.10 represents the time-averaged static pressure at one rotor blade at the same operating conditions. It shows a comparable pressure field is for different RT casing for both pressure and suction sides of the blade.

In addition, the time-averaged blade loading at blade mid-span is plotted for different casings as shown in Figure 6.11. It shows in general comparable



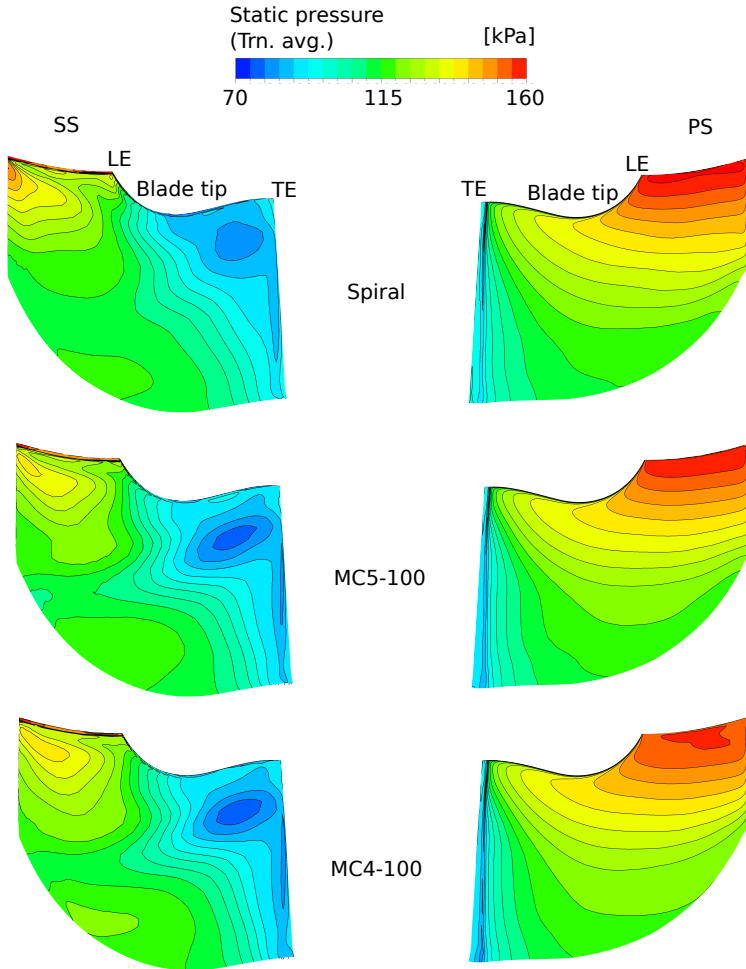
**Figure 6.9:** Static pressure at turbine stage mid-span for different casing types, transient simulation

blade loading except at one position at the 50% stream-wise direction for the blade suction side. However, on average the deviation in the time-averaged blade loading is lower than 1.5 % which proves comparable operating conditions.

The effect of different RT casings on the unsteady pressure is illustrated in Figure 6.12. It represents the static pressure during one rotor revolution at different monitoring points at a 90% span of the rotor blade. It shows that the MC is characterized by a repeated pressure pattern during the full admission condition in contrast with the spiral casing.

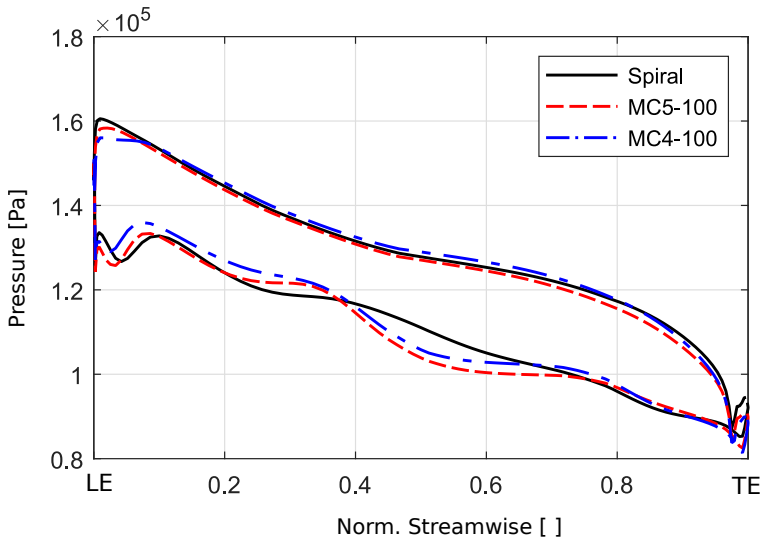
This symmetrical repeated pattern results in a different harmonic pressure depending on the channel count. To explain this behavior, the unsteady pressure at one operating point is plotted for different cases as shown on top of Figure 6.13. Then, the harmonic pressure components are calculated by performing a Fourier Transformation (FT) for the unsteady pressure as presented at the bottom of the same figure for the first ten Engine Orders (EO). It is clear that the MC casing with 5 channels has a harmonic pressure component at the 5th and 10th EOs while the 4 channel casing has at the 4th and





**Figure 6.10:** Time-averaged static pressure at blade surface for different casing types

8th EOs. In contrast, the spiral casing shows harmonic pressure components at all EOs due to the asymmetric pressure pattern.



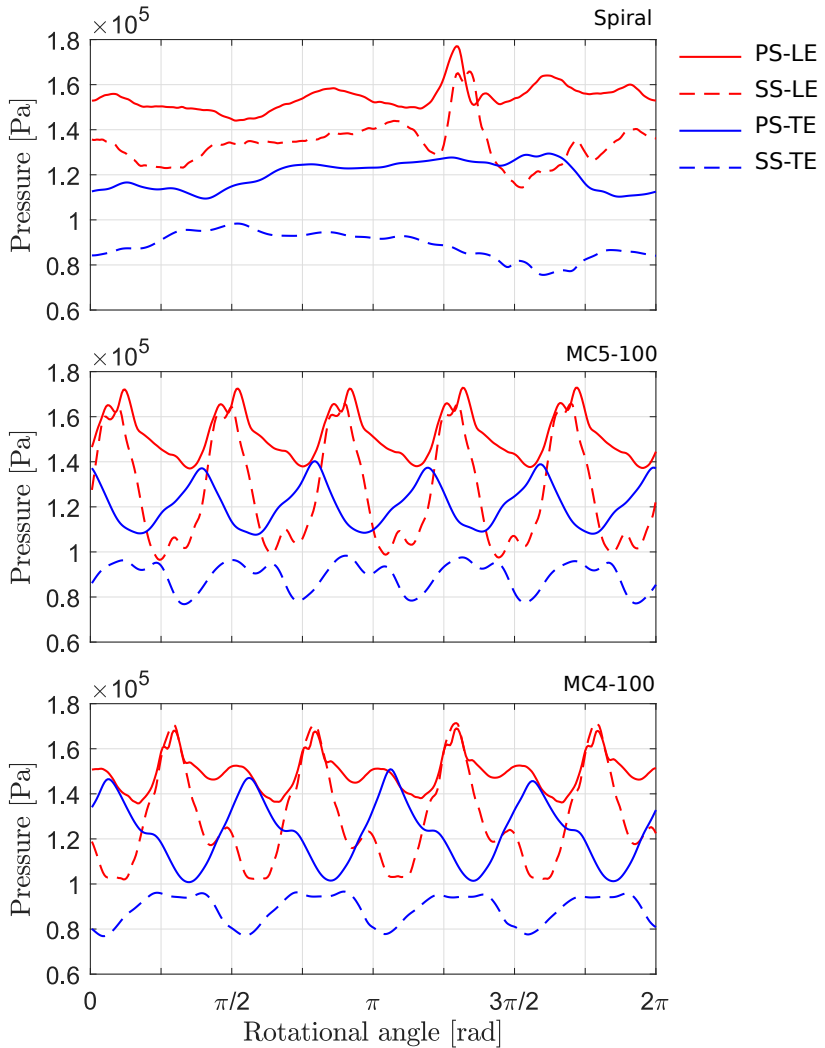
**Figure 6.11:** Time-averaged blade loading for different casing types, mid-span

## 6.2 Structural Model

In order to identify the mechanical vibration behavior of the turbine, an FE numerical model is carried out. This model calculates the natural frequency and the mode shape of the turbine rotor. A rotor material is Inconel-713lc and its main metrics are described in Figure 6.14.

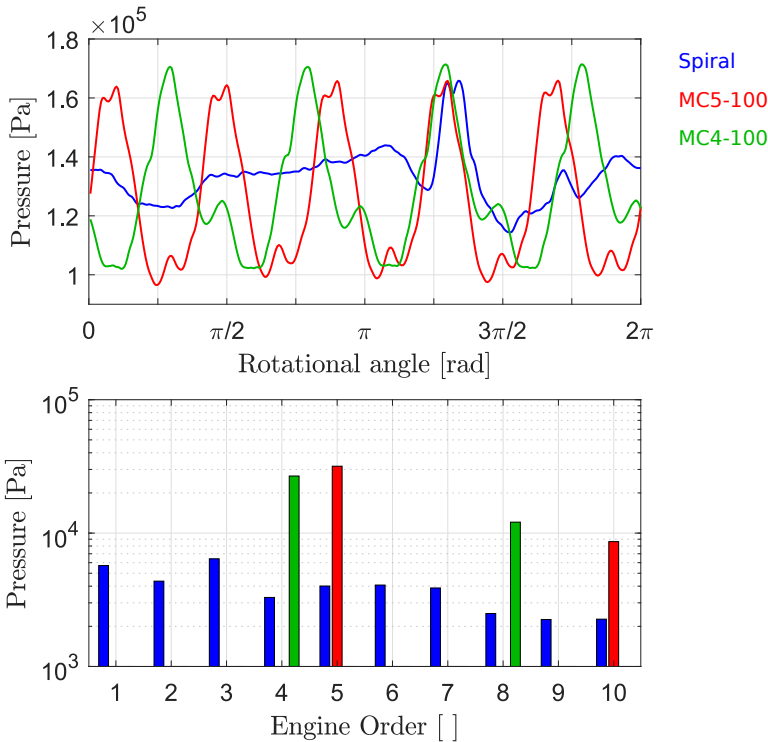
For the structural model, the cyclic periodicity of the turbine wheel geometry is used to create a sector model. This sector model is meshed and the full turbine model is then created by simply copy and rotating the sector model. In this way, an identical mesh can be guaranteed for all eleven blade segments and mistuning due to different mesh can be excluded.

The hexagonal-shaped of the rotor hub-end was simplified by a cylinder extension to achieve a high-quality mesh topology. The FEM simulations were performed using the software ANSYS Mechanical in version 19.2. The blade sector model is meshed in a structured manner with 16750 hexahedral elements using ICM software as shown in Figure 6.15. This grid size is chosen



**Figure 6.12:** Unsteady pressure at different monitor points for different casings, 90% span

after a mesh independency study to ensure an independent modal displace-

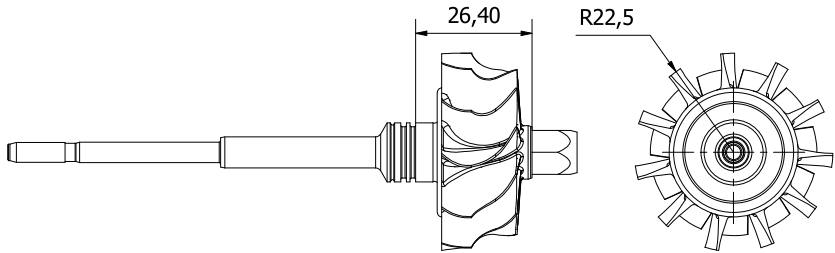


**Figure 6.13:** Unsteady pressure and its harmonic spectrum for different casings

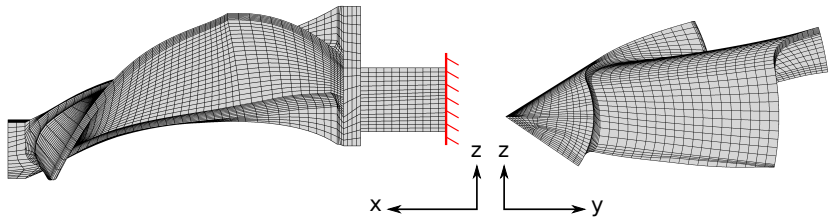
ment field. This also matches with the conclusions from similar studies for a comparable rotor geometry [41, 69].

For the static and modal structural analysis, the shaft is shortened to the level of the bearing position on the turbine side, which has a negligible influence on the natural vibration behavior of the blades. This is based on the findings from another project performed at the ITSM [78], in which this type of model extent was found to be best suited. The axial cut surface of the shortened shaft is only fixed in the axial direction. A cyclic symmetry prestressed model analysis is performed with different temperatures and rotational speeds as a thermal and centrifugal structure loads, respectively.

The result of the modal analysis is presented by the Campbell diagram in Figure 6.16. It represents the natural frequencies for the first bending mo-



**Figure 6.14:** Investigated turbine rotor



**Figure 6.15:** FE model of a turbine wheel

de through the operating range of the turbine rotational speed for three different operating temperatures.

The numerical result agrees with the experimental result represented in Chapter 5 with a limited deviation due to the difference between the real and CAD geometry and the geometrical simplifications. In this study, the resonance crossing at the first bending mode for EO 5, 6, 7, and 8 are considered for different casing comparison. The operating speeds for each crossing are represented in Figure 6.16.

The rotor natural frequencies for the first two modes as a function of the nodal diameter are shown in the ZZENF diagram (Zig Zag shaped Excitation line in Nodal diameter versus Frequency), Figure 6.17. The relevant resonance rotational speeds are plotted by the black zig-zag lines and have a crossing with the first bending mode for different EO and ND. Different nodal diameters for the first bending mode are presented in Figure 6.18.

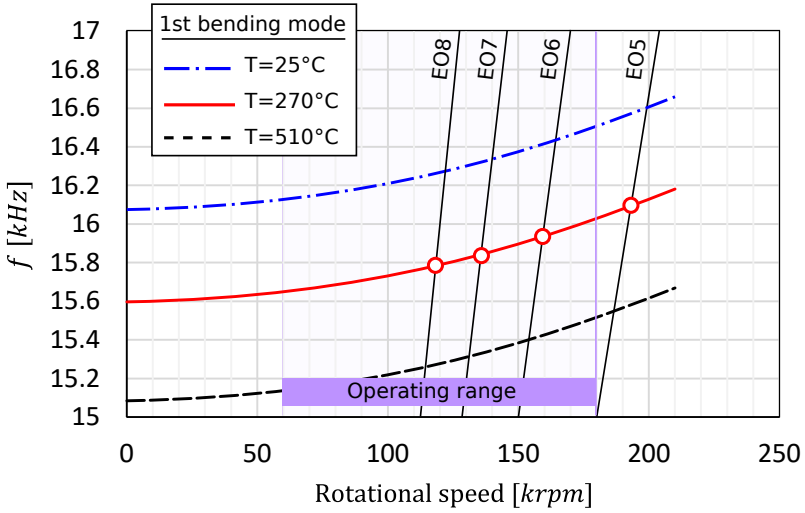


Figure 6.16: Turbine rotor Campbell diagram

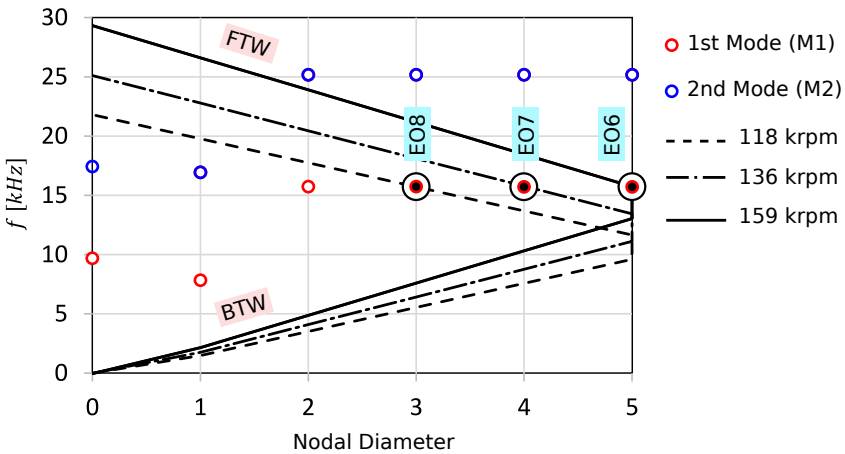
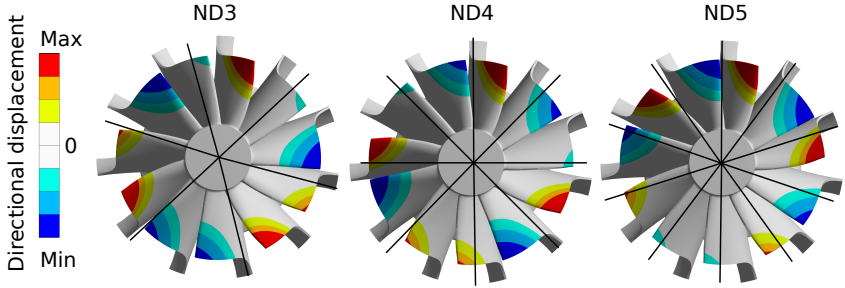


Figure 6.17: ZZENF diagram



**Figure 6.18:** Different nodal diameter for resonance crossing, first bending mode

## 6.3 Fluid Structure Interaction

A one-way Fluid-Structure Interaction (FSI) model is used in this study to investigate the aerodynamically excited vibrations. This approach solves the CFD and the FE model separately then combines both results using different FSI models to calculate both the aerodynamic forcing and damping and performing a forced response analysis. Compared to the two-way FSI model, It shows accurate results in noticeably shorter calculation time as reported by Mayorca et al. [48–50] and Netzhammer et al. [58, 59] in comparable studies.

### 6.3.1 Aerodynamic Excitation

The Generalized Force (GF) approach is used to calculate the aerodynamic excitation by projecting the harmonic forces onto the modal displacement at a specific resonance point [5, 22, 29]. Starting from the unsteady CFD results, a Fourier decomposition of the fluctuating pressure signal on the blade surface was performed in order to obtain the harmonic components as follows:

$$\tilde{p}_n = A_n + B_n i \quad (6.1)$$

$$A_n = \frac{2}{spp} \sum_{x=atstep-spp}^{atstep} p(x) \cos\left(-2\pi n \frac{x}{spp}\right) \quad (6.2)$$

$$B_n = \frac{2}{spp} \sum_{x=atstep-spp}^{atstep} p(x) \sin\left(-2\pi n \frac{x}{spp}\right) \quad (6.3)$$

Following this, a GF code is used to project the mode shape onto the harmonic pressure field at specific resonance states and compute the GP using the following relation:

$$p_{gen,i} = \vec{\Phi}_i \cdot \vec{n}_i \tilde{p}_n \quad (6.4)$$

Finally, the total GF is calculated by summing the GP components multiplied by the corresponding area as follows:

$$F_{gen,tot} = \sum p_{gen} \Delta A \quad (6.5)$$

### 6.3.2 Aerodynamic Damping

Aerodynamic damping coefficient can be calculated after combining the CFD and FE results in other FSI models using Equations 2.26 and 2.27. The mode shape of the resonance crossing of interest is defined on the CFD solver as a blade motion using a dynamic mesh technique. The mesh displacement is applied over CFX Expression Language (CEL), which calculates the coordinates for each blade mesh point as a function of time. Firstly, the complex mode shape of interest is exported from the FE solver. Secondly, the real and imaginary components of the mode shape are superimposed according to the direction of the traveling wave to define the coordinates of the nodes as a function of time for the rotor blades as shown in Equation 6.6 according to the forward traveling wave as presented in Figure 6.17.

$$\begin{bmatrix} x \\ y \\ z \end{bmatrix} = Sf \cdot \left[ \begin{bmatrix} x \\ y \\ z \end{bmatrix}_r \cos(\omega t) + \begin{bmatrix} x \\ y \\ z \end{bmatrix}_i \sin(\omega t) \right] \quad (6.6)$$

The Scaling Factor (SF) is set such as to scale the maximum total displacement to an experienced-based suitable value, which in this case is  $70 \mu m$ . Excessive scaling factors should be avoided as they may cause problems in the CFD solver while applying the mesh displacement.

The pressure perturbation due to the blade vibration can be calculated by subtracting the pressure field resulting from the fixed blade simulation from the vibrating blade simulation. This subtraction suppresses any effect of the rotor-stator interaction and ensures that the pressure perturbation is only



attributed to the blade vibration. This approach is based mainly on the assumption of the linear superposition of the pressure perturbation due to rotor-stator interaction and blade vibration which was validated by Müller [57].

### **6.3.3 Forced response analysis**

After calculating aerodynamic loads and damping coefficient, a forced response analysis can be performed to calculate the dynamic stresses and vibration amplitude. The forced response analysis is performed using the same FE model neglecting the structural mistuning effect.

The numerical results of all FSI models is presented in details and is compared with the available test data in Chapter 8



## **7 Effect of Multi-channel Casing on Turbine Performance**

To ensure the best performance of the MC at different admission configuration percentages, it becomes crucial to investigate the effect of replacing the spiral volute with an MC and applying different admission percentages on the turbine performance. This investigation focuses mainly on the internal flow field and the generated loss mechanisms and helps in operating the turbine at the most efficient design in different admission configurations, especially at low admission percentages.

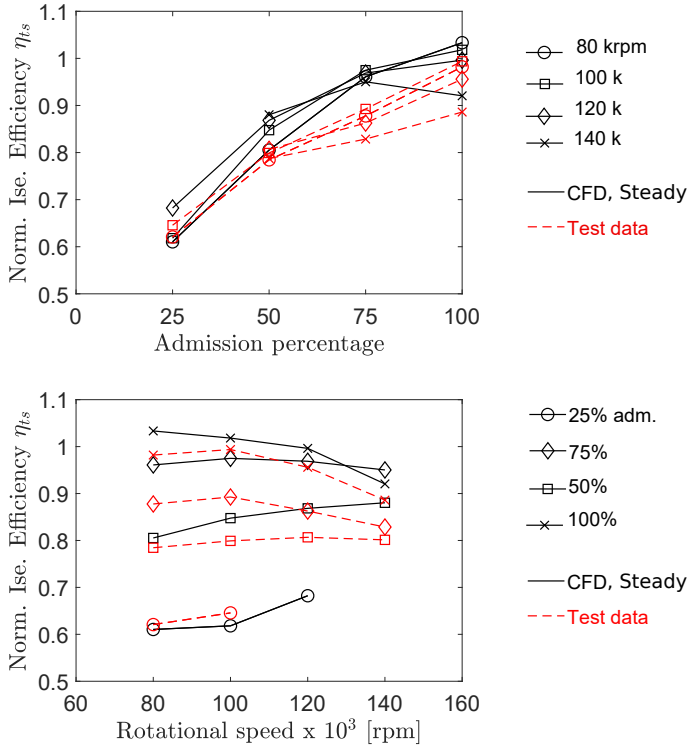
Therefore this chapter focuses mainly on the loss generation mechanisms of the radial turbine featuring MC at full and partial admission. Test data and CFD results are combined to conduct this investigation. The test data shows a reduction in performance by reducing the admission percentage. A full 3D Computational Fluid Dynamic (CFD) model has been created. Steady and unsteady simulations for this model at full and partial admission at different operating conditions have been performed. The CFD results have been analyzed to detect the reason behind the performance reduction.

### **7.1 Performance and Flow Analysis**

The efficiency values at the Best Efficiency Points (BEP) for different speed lines and admission configurations have been plotted in two different ways as shown in Figure 7.1. This figure presents the effect of some specific parameters such as the admission percentage and rotational speed on the turbine performance. It shows in general that the efficiency value at the BEP decreases with reducing the admission percentage for all rotational speeds. Moreover, it decreases with increasing rotational speed for the admission percentage of more than 50% and vice versa for lower admission.

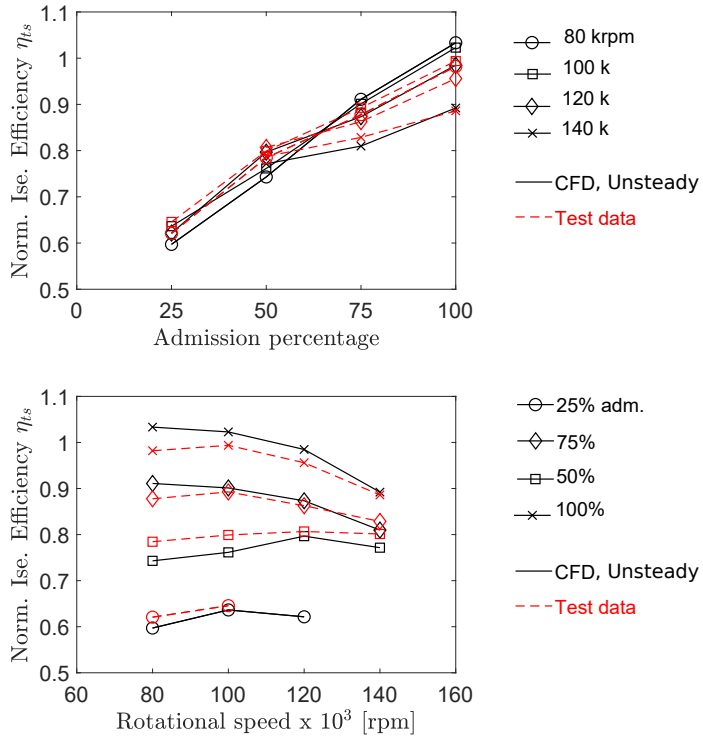
Unsteady simulations have been performed as a trial to achieve better prediction of the turbine operating efficiency. Performing such simulations for a

complete turbine map is time-consuming. Therefore the unsteady simulation is performed at the BEP of each speed line for full and partial admission. The result of the unsteady simulations in comparison with the test data is presented in Figure 7.2. Besides confirming the same tendency described by the steady simulation results, the unsteady results also reduce the error in the efficiency prediction compared to the steady simulations.



**Figure 7.1:** Effect of the admission percentage (top) and rotational speed (bottom) on the turbine efficiency at BEP, four-channel casing, steady simulation

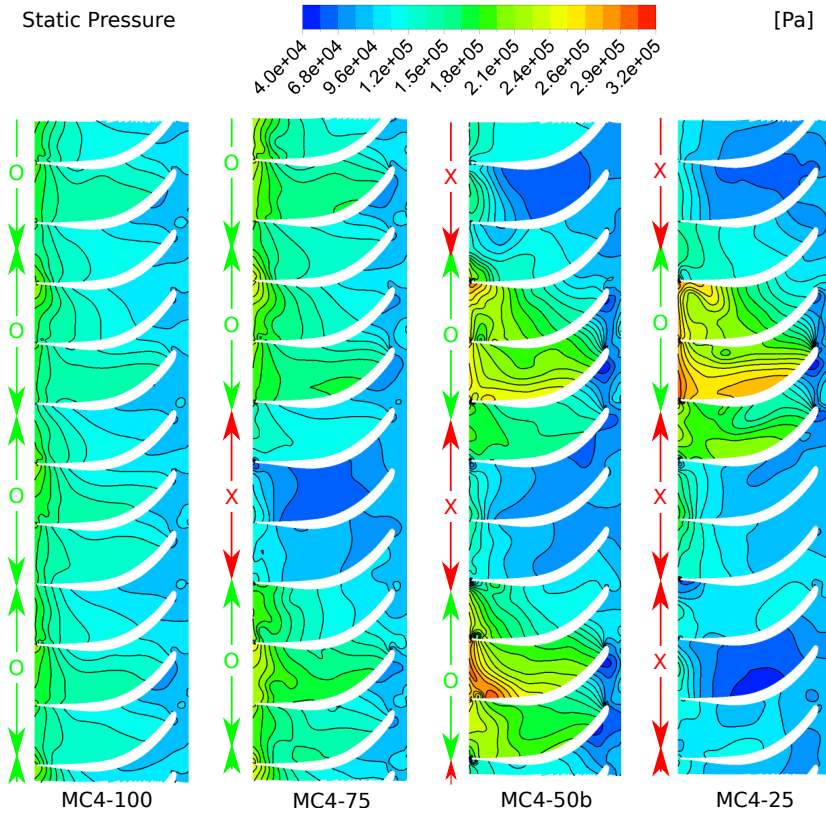
The results show the capability of the unsteady simulation in predicting the operating efficiency of the turbine featuring an MC. Therefore this result will be investigated in depth for a better understanding of the flow field at different admission configurations in order to explain the efficiency reduction in the partial admission cases compared to full admission.



**Figure 7.2:** Effect of the admission percentage (top) and rotational speed (bottom) on the turbine efficiency at BEP, four-channel casing, unsteady simulation

The static pressure contour has been plotted at a fixed position of the rotor mid-span for all different admission configurations, as shown in Figure 7.3. It describes how the static pressure in the rotor is affected by changing the admission configuration. The closed channel causes a static pressure reduction within the rotor passages facing it, inflicting a flow disturbance at this position. At a specific rotor position, the blade suction side faces a static pressure higher than the pressure side. The duration of this situation increases with decreasing admission percentage.

Undoubtedly, this abrupt change in the static pressure during the turbine operation affects the blade torque in an unsteady manner. For further explanation, the computed blade torque has been plotted during one complete

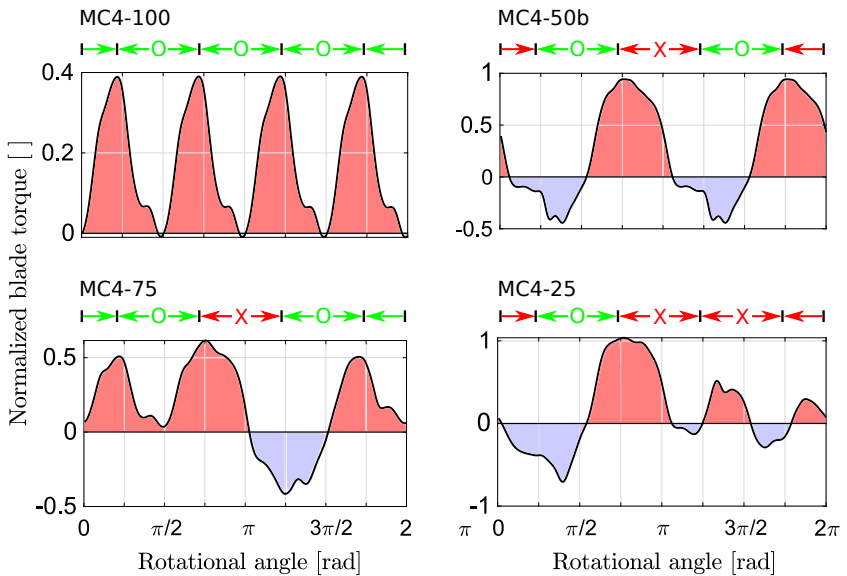


**Figure 7.3:** Static pressure contour at rotor mid-span at a specific instance for different admission percentage

revolution for different admission configurations, as shown in Figure 7.4. At full admission (MC4-100), the blade torque peaks when the blade is facing an end of a stator channel. Then it decreases when the blade passes through the inter-space between two channels until it starts increasing again in the middle of the next channel. This process is repeated with a number equal to the channel count, four times in this case.

After closing one channel (MC4-75), the torque pattern changes to an asymmetric pattern. The torque decreases after passing through the inter-space of two channels and continues decreasing through the closed channel with

a negative peak (i.e. it brakes the rotor) before it starts increasing again through the next open channel. At MC4-50b configuration, the blade torque pattern is symmetric again but with two positive and two negative regions due to the two closed channels. At the lowest admission case MC4-25 with only one open channel, the blade torque rises to its peak value when the blade faces the sector end of the open channel, and then it decays gradually through the three closed channels. This decay is characterized by three negative regions that expand gradually in the direction of the blade rotation.



**Figure 7.4:** Blade torque for different admission configurations

## 7.2 Loss Mechanisms

In order to investigate how different admission configurations increase the turbine losses, the sources of the losses are evaluated by analyzing the Entropy Generation Rate (EGR) in the simulated domains. Recent works [7, 34, 35, 70] have developed this method to obtain the volumetric entropy generati-

on rate by viscous dissipation ( $\dot{S}_v$ ) and by thermal diffusion ( $\dot{S}_t$ ) as shown in Equations 7.1 and 7.2, respectively.

$$\dot{S}_v = \frac{\mu_{eff}}{T} \{2[(\frac{\delta u}{\delta x})^2 + (\frac{\delta v}{\delta y})^2 + (\frac{\delta w}{\delta z})^2] + [(\frac{\delta u}{\delta y} + \frac{\delta v}{\delta x})^2 + (\frac{\delta u}{\delta z} + \frac{\delta w}{\delta x})^2 + (\frac{\delta v}{\delta z} + \frac{\delta w}{\delta y})^2]\} \quad (7.1)$$

$$\dot{S}_t = \frac{\lambda_{eff}}{T^2} [(\frac{\delta T}{\delta x})^2 + (\frac{\delta T}{\delta y})^2 + (\frac{\delta T}{\delta z})^2] \quad (7.2)$$

In the case of radial turbine flow, the EGR from the thermal diffusion term was considered to be minor compared to viscous dissipation and could be neglected [16, 60]. Based on the idea of Reynolds decomposition the EGR could be decomposed into time-averaged EGR ( $\dot{S}_{\bar{v}}$ ) and fluctuating EGR ( $\dot{S}_{\tilde{v}}$ ) parts as shown in Equations 7.3 and 7.4, respectively.

$$\dot{S}_{\bar{v}} = \frac{\mu_{eff}}{T} \{2[(\frac{\delta \bar{u}}{\delta x})^2 + (\frac{\delta \bar{v}}{\delta y})^2 + (\frac{\delta \bar{w}}{\delta z})^2] + [(\frac{\delta \bar{u}}{\delta y} + \frac{\delta \bar{v}}{\delta x})^2 + (\frac{\delta \bar{u}}{\delta z} + \frac{\delta \bar{w}}{\delta x})^2 + (\frac{\delta \bar{v}}{\delta z} + \frac{\delta \bar{w}}{\delta y})^2]\} \quad (7.3)$$

$$\dot{S}_{\tilde{v}} = \frac{\mu_{eff}}{T} \{2[(\frac{\delta \tilde{u}}{\delta x})^2 + (\frac{\delta \tilde{v}}{\delta y})^2 + (\frac{\delta \tilde{w}}{\delta z})^2] + [(\frac{\delta \tilde{u}}{\delta y} + \frac{\delta \tilde{v}}{\delta x})^2 + (\frac{\delta \tilde{u}}{\delta z} + \frac{\delta \tilde{w}}{\delta x})^2 + (\frac{\delta \tilde{v}}{\delta z} + \frac{\delta \tilde{w}}{\delta y})^2]\} \quad (7.4)$$

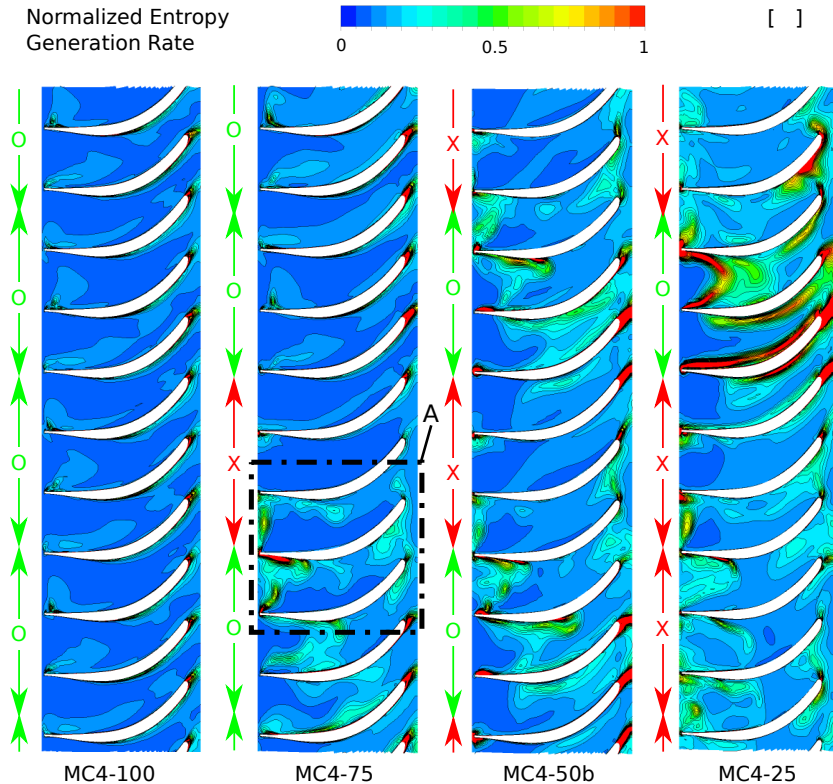
The time-averaged part ( $\dot{S}_{\bar{v}}$ ) of the EGR can be evaluated directly through any CFD solver after calculating the time-averaged value of the velocity gradient. The fluctuating part of the EGR ( $\dot{S}_{\tilde{v}}$ ) can be approximated as in Equation 7.5 [42, 45]. Here,  $k$  and  $\omega$  are the turbulence kinetic energy and characteristic frequency in the Shear-Stress Transport  $k$ - $\omega$  model, respectively. The empirical constant  $\alpha$  is chosen as 0.09, as recommended by the mentioned studies.

$$\dot{S}_{\tilde{v}} = \alpha \frac{\rho \omega k}{T} \quad (7.5)$$

The EGR is plotted for four different admission configurations at the rotor mid-span in Figure 7.5. This plot has been normalized using the maximum EGR value that has been recorded at the 25% admission case. MC4-100



shows the same sources of loss that occur in the radial turbine featuring traditional spiral casing, such as the incidence and separation losses in rotor blades.

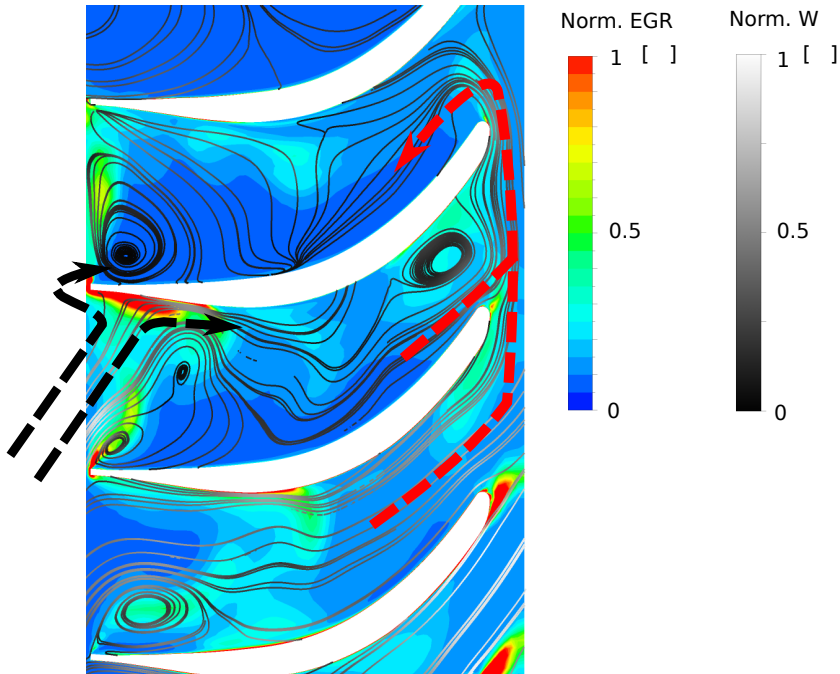


**Figure 7.5:** Entropy generation rate contour at rotor mid-span for different admission percentage

All the partial admission cases starting from the 75% up to 25% admission are characterized by a different loss type. This loss could be recognized by comparing the EGR at the full admission case with the partial admission cases. Based on this comparison, a higher EGR area is recognized at the MC4-75 case as shown in zone (A) in Figure 7.5. This increase of the EGR starts on the blade leading edge at the suction side after passing a closed

channel. To fully understand the reasons behind this sharp increase of the EGR in this specific region, the EGR and the normalized relative velocity streamlines have been superimposed at zone (A), as shown in Figure 7.6.

Due to the static pressure difference between the opened and closed channel, the relative inflow angle changes dramatically and deviates from its design value at design condition. This change causes high incidence of the flow, which hits the blade and causes this increase of the EGR as indicated by the black arrows. This loss mechanism behavior is similar to the incidence or the shock losses mechanism that occurs when operating the turbine at the overload condition. Therefore it will be defined as partial admission shock loss.



**Figure 7.6:** EGR contour and normalized relative velocity at zone (A)

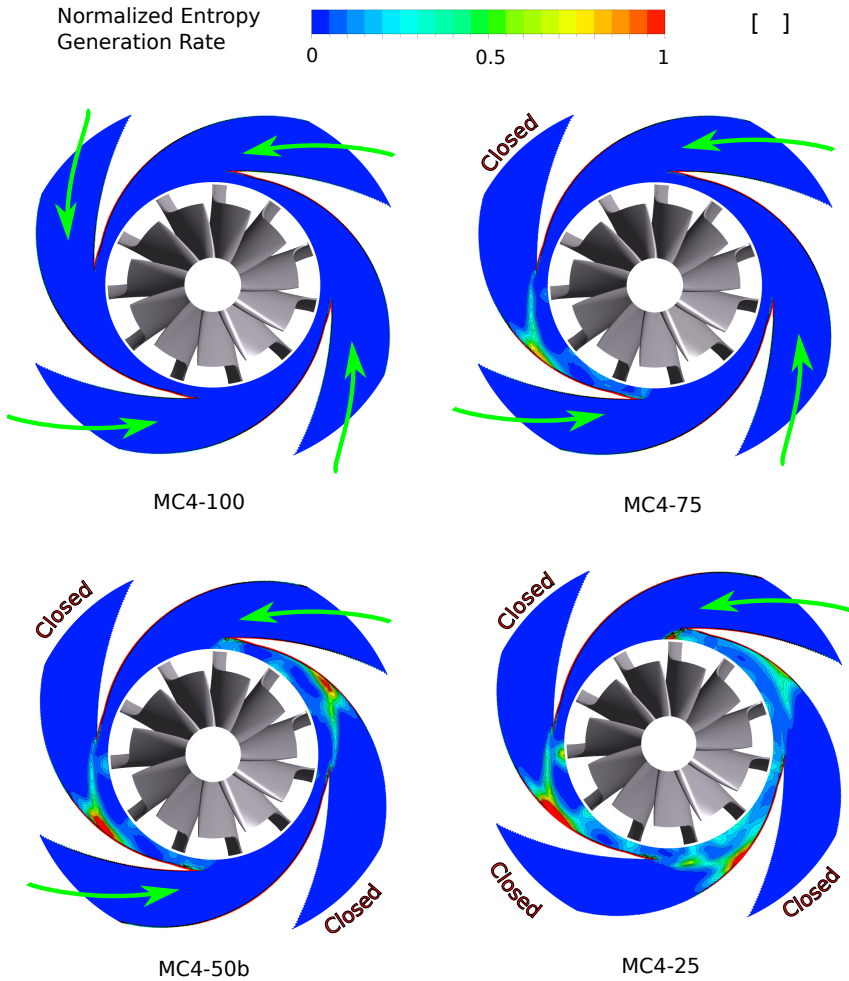
One of the main factors that affect the change in the inflow angle is the pressure difference between the open and closed channels. The higher the

difference in static pressure, the higher the deviation between the actual inflow angle and its designed value. The static pressure difference between two different blade passages is also responsible for the backflow, which can be noticed at the blade trailing edge. Part of the flow after exiting the rotor reenters the rotor again but in a different passage that is characterized by lower static pressure as described by the red arrow. For the lower admission configurations such as 50% and 25% admission, the same loss mechanisms have been identified but in multiple positions based on the number of closed channels.

Moreover, the EGR has been investigated for the flow at the casing domain. It has been plotted on the casing mid-span, as shown in Figure 7.7. This figure shows the places where the EGR increases for different partial admission configurations compared to the full admission case. The EGR and the streamline of the relative velocity are superimposed, as shown in Figure 7.8 to understand the reasons behind the EGR increases. The rotor flow deviation can also be observed in the casing. Due to the static pressure difference between open and closed channel the flow deviates, and instead of entering the rotor it stagnates at the casing wall and causes an increase of the EGR.

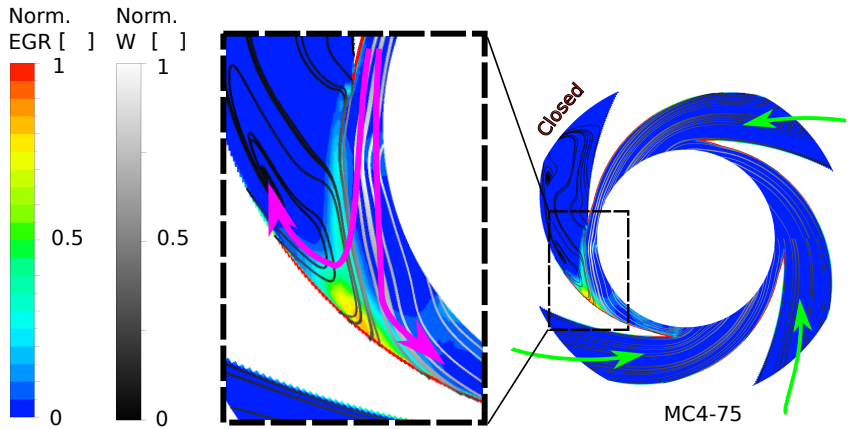
After detecting the highest EGR locations in the rotor and the casing domains for different admission configurations, Figure 7.9 sums up and quantifies the entropy increase in each of the turbine domains and compares it for different admission configurations. In general, the entropy increases at all turbine domains when reducing the admission percentage. Moreover, the entropy increase is highest in the rotor domain for all admission configurations. The relation between the entropy increase and the admission percentage is approximately linearly proportional.

In order to investigate the ability to enhance operating efficiency, a geometrical parameter has been selected and varied to monitor its effect on the efficiency reduction caused by the partial admission. As has been discussed, the secondary flow, which takes place due to the differences in static pressure between opened and closed channels, is responsible for the efficiency reduction at partial admission cases. Therefore, the radial gap between the casing and the rotor is assumed to be a decisive factor in controlling this secondary flow. Based on that, it was selected as the investigated geometrical parameter. A ratio between the casing outlet radius to the rotor inlet radius is defined to represent the radial gap. Three cases with different radial gaps are investigated in this study. The datum case has a radius ratio of 1.15, while the other cases have a ratio of 1.05 and 1.25.

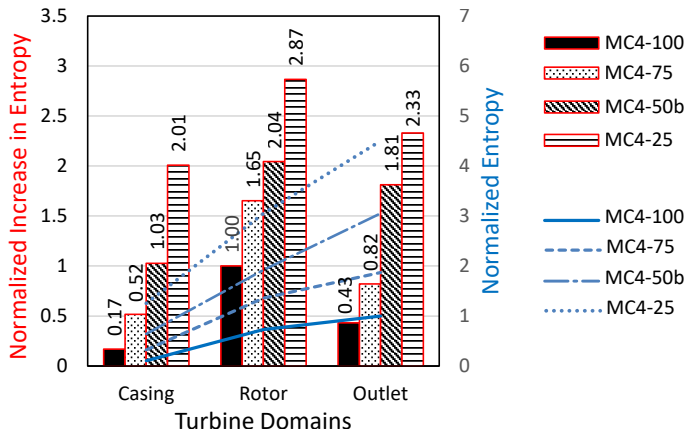


**Figure 7.7:** EGR contour at casing mid-span for different admission percentage

The EGR for the 50% admission case for different radial gaps has been plotted, as shown in Figure 7.10. It is noticeable that the EGR slightly increases at the highest radial gap. The entropy increase in different turbine domain for different radial gaps is presented in Figure 7.11 after normalizing the

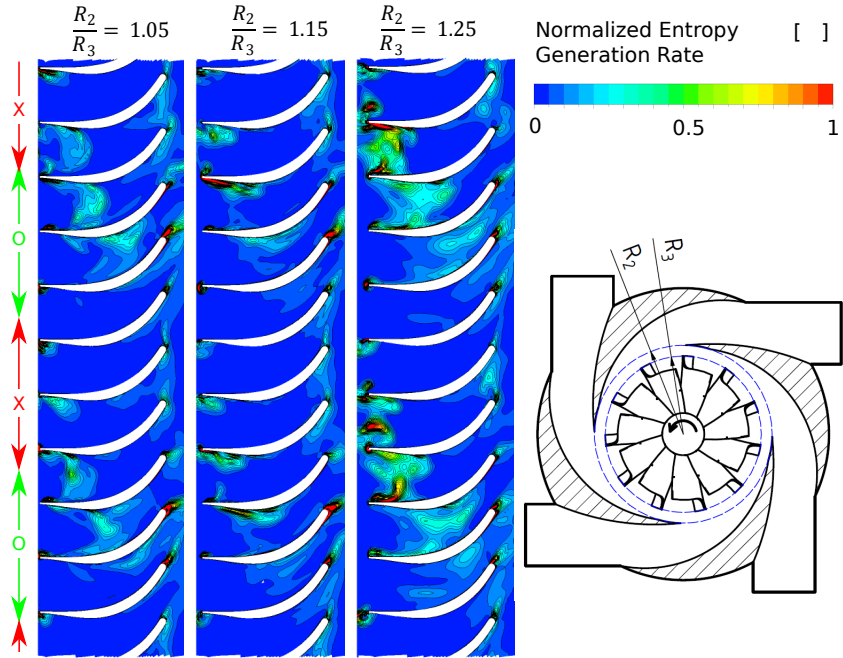


**Figure 7.8:** EGR contour and normalized relative velocity at casing mid-span, MC4-75

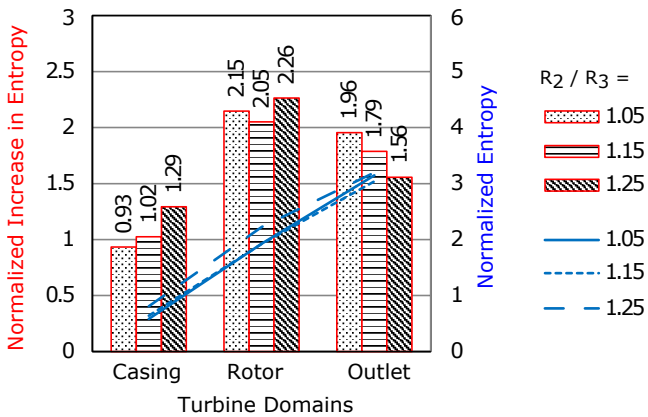


**Figure 7.9:** Entropy increase in different turbine domains, for different admission configurations

values with the same normalization factor, which has been used in Figure 7.10. This chart proves that the change in the operating efficiency due to the geometrical change is minor compared to the efficiency reduction due to the partial admission operation.



**Figure 7.10:** EGR contour and normalized relative velocity for different radial gap, MC4-50b



**Figure 7.11:** Entropy increase for different radial gap, MC4-50b

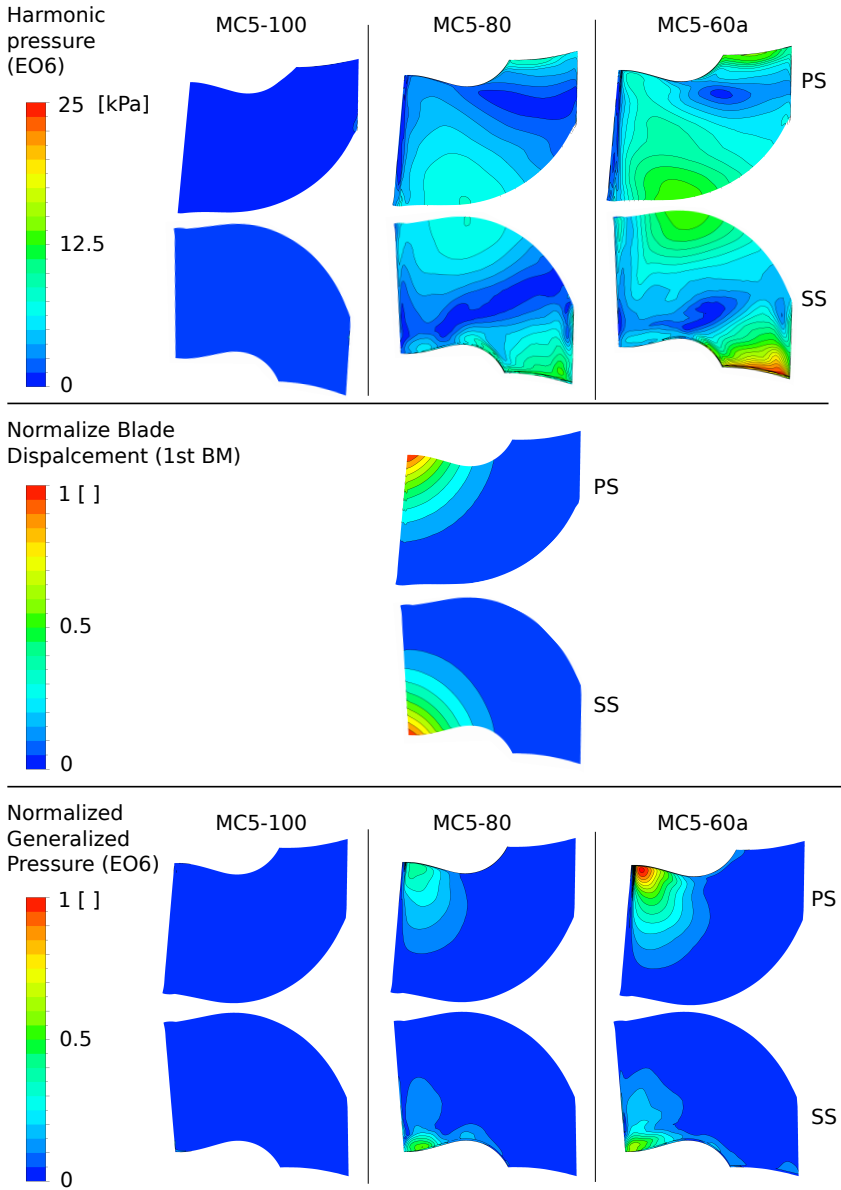
## **8 Effect of Multi-channel casing on Blade Vibration**

This chapter focuses on the effect of using an MC and applying different admission configurations on the RT blade vibration. The investigation is divided into three main sections. The first two parts study the effect on the aerodynamic excitation and damping, while, the last part performs a blade forced response analysis to calculate the blade vibration amplitude and the dynamic stresses.

### **8.1 Aerodynamic Excitation**

This section studies the effect of replacing the spiral casing with an MC casing and applying different admission configurations on the aerodynamic excitation in a radial turbine. The generalized force approach is used to represent the aerodynamic excitation by projecting the harmonic load onto the mode shape of interest as explained in Section 6.3.1. The generalized force is calculated for nine different cases which are tested experimentally as shown in Section 5.4. These nine cases represent three different admission configurations MC5-100, MC5-80, and MC5-60a and three different resonance crossing EO6, EO7, and EO8.

Firstly, unsteady CFD simulations for these nine cases are performed using CFX with the unsteady setup as represented in Section 6.1.3. Secondly, the harmonic pressure at each engine order is calculated using Equation 6.1. A sample of the harmonic pressure for different admission configurations for EO6 is presented at top of Figure 8.1 for the blade pressure and suction side. The comparison of the harmonic pressure for different admission configurations shows that at the same EO applying partial admission can increase the harmonic pressure drastically. This is attributed to the change of the frequency spectrum when operating at partial admission and the increase in the expansion ratio with the reduction of the admission percentage.

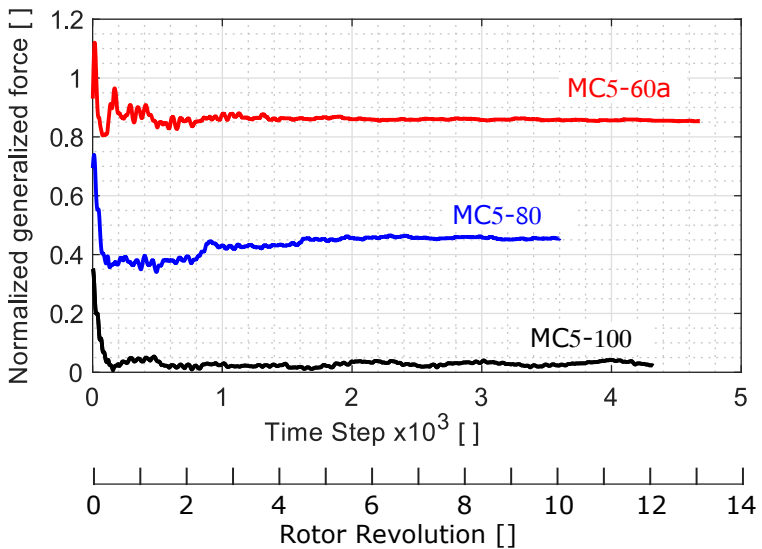


**Figure 8.1:** FSI Simulation Results at EO6, different admission configuration



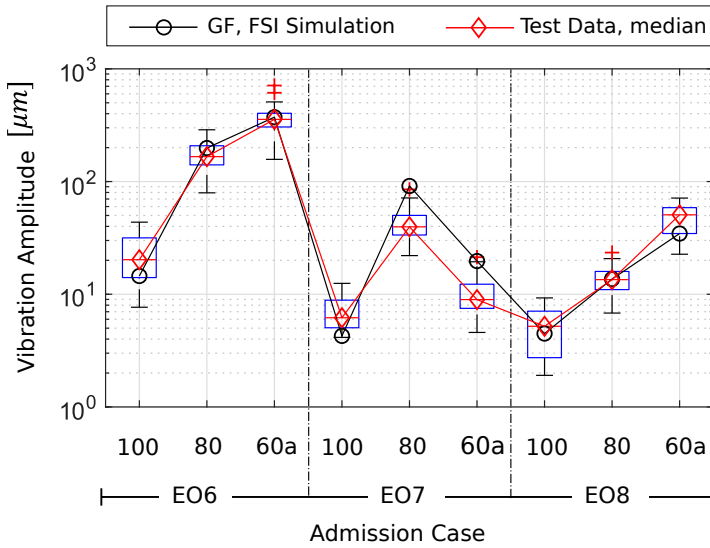
Thirdly, the harmonic pressure is projected onto the mode shape of interest (first bending mode) in order to calculate the generalized pressure as presented in Equation 6.4. The generalized pressure contours for the same cases are represented at bottom of Figure 8.1. Based on the mode shape of interest the maximum generalized pressure is monitored near the blade trailing edge for the MC5-60a case.

Finally, the generalized force which represents the aerodynamic excitation is calculated using Equation 6.5. The convergence of the generalized force is monitored by plotting its value every time step as shown in Figure 8.2. all the nine cases are converged after around 1420 to 1800 time steps i.e., after 4 to 5 rotor revolutions for the 360 time-steps per one complete revolution.



**Figure 8.2:** Generalized force convergence, EO6

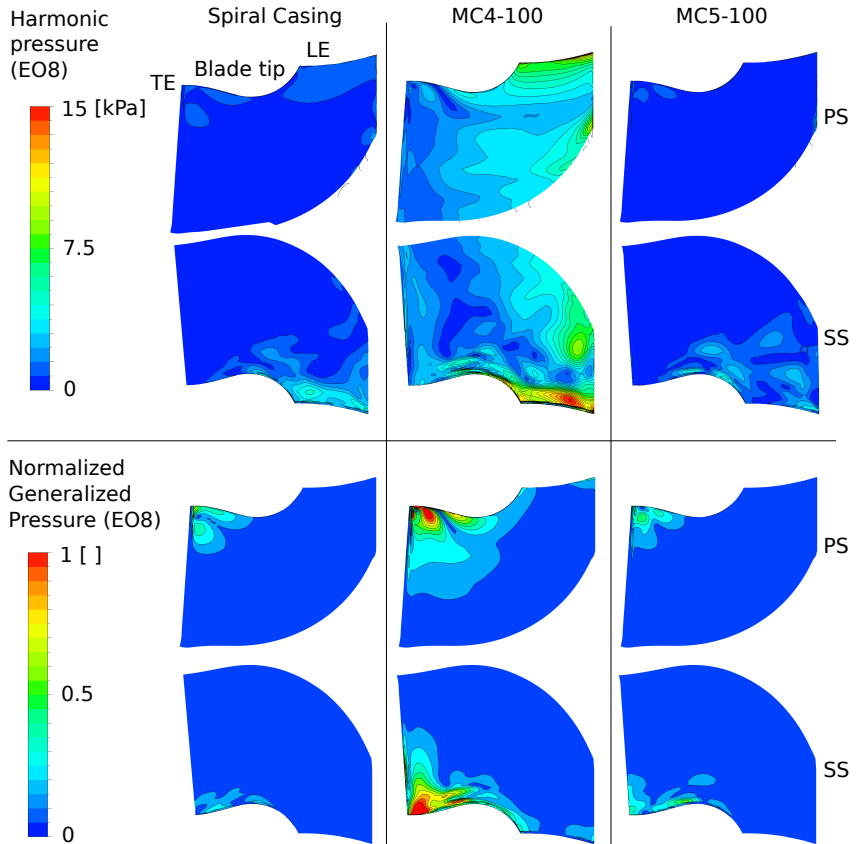
The generalized force for all nine cases is scaled using the same scaling factor to plot it in comparison with the measured vibration amplitude as shown in Figure 8.3. Although the damping effect is not considered in calculating the generalized force, it could represent the measured vibration amplitude. both the measured vibration amplitude and the calculated generalized force follow the same trend for the nine cases with a slight deviation.



**Figure 8.3:** Generalized Force (GF) compared to vibration test data, different admission configuration

After validating the generalized force approach in presenting the aerodynamic excitation using the nine cases which are tested experimentally. It is used to detect the effect of different casing types and different admission percentages and configuration on the aerodynamic excitation. Two different casing types have been investigated the spiral casing and MC. The MC casing with four and five channels and different admission percentages are considered. These different casings are investigated at the EO8 resonance crossing. This EO is selected specifically because it could show high excitation when using MC with four channels.

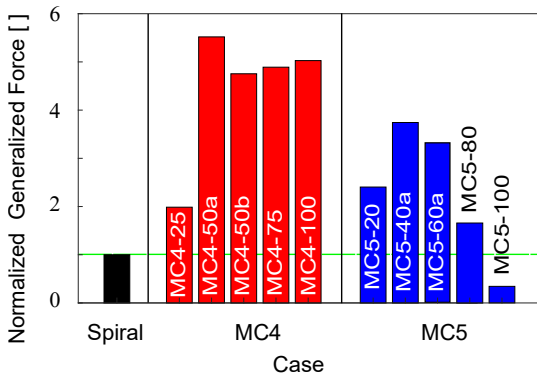
The same procedure and convergence criteria have been followed in calculating the generalized force for different casings type. the harmonic pressure and generalized pressure at the rotor blade according to EO8 for both pressure and suction side at full admission are shown in Figure 8.4. For full admission, The MC with four-channel casing shows the highest generalized pressure compared to the spiral casing and MC with five channels.



**Figure 8.4:** FSI Simulation Results at EO8 for different casing type, Full admission

After ensuring the convergence of the simulations, the generalized force values for different casing types and different admission percentages are plotted in Figure 8.5. The generalized force for the spiral casing is chosen to be the reference value for all different cases.

The results show that the MC5 at full admission reduces the aerodynamic excitation level by approximately one third compared to the spiral casing. Whereas operating the same casing at partial admission could increase the excitation level up to three times comparing also to the spiral casing as



**Figure 8.5:** Generalized force for different casing types and admission configurations, EO8

achieved by case MC5-40a. In contrast, MC4 increases the excitation level up to five times when operating at both full and partial admission compared to the spiral casing except for the case MC4-25 which increases it only two times.

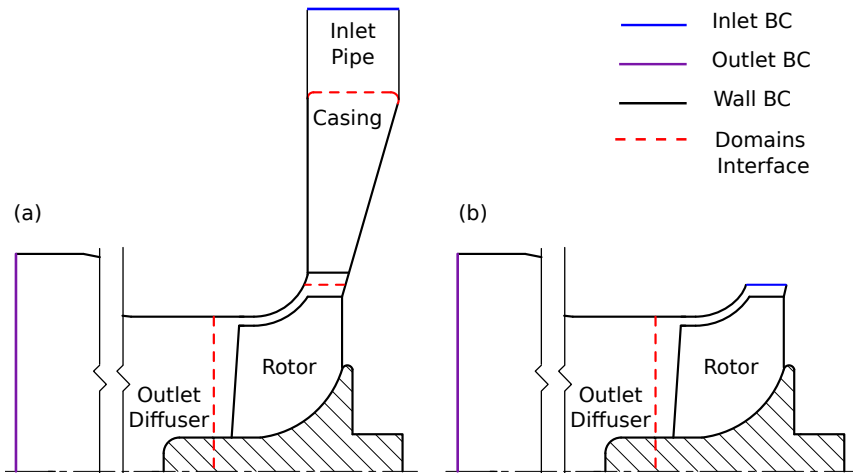
## 8.2 Aerodynamic Damping

The current section investigates the effect of different MC admission configurations on the blade aerodynamic damping as a part of an aeromechanical investigation for a radial turbine featuring an MC casing. The aerodynamic damping simulations are performed on a 3D model of a radial turbine featuring various MC configurations. An isolated and full CFD models are performed to predict the aerodynamic damping coefficient. The CFD domains for each model are shown in Figure 8.6

The isolated rotor approach is based on building a numerical model consisting of the rotor domain alone while imposing the blade motion according to the investigated mode shape. To achieve the same flow in the isolated rotor as when operated in the stage, the unsteady flow condition at the casing-rotor interface has been time-averaged and used as inlet Boundary Condition (BC) for the isolated rotor. This method eliminates the forcing effect from

the adjacent blade row that affects the damping evaluation. Thanks to its simplicity, this approach is frequently used [19, 47, 53, 75].

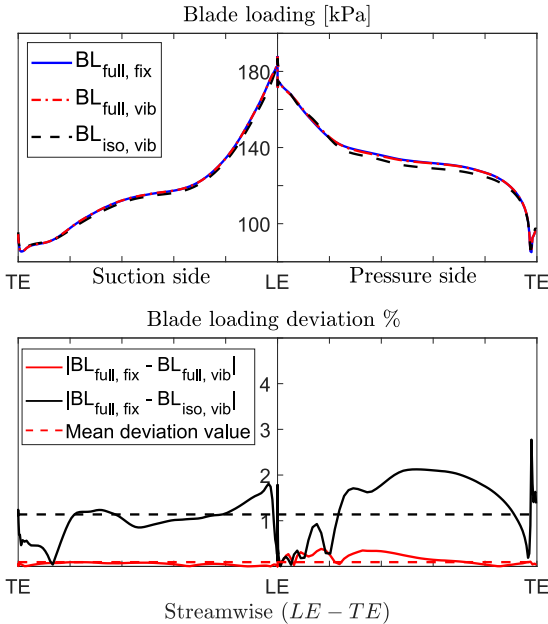
The full model approach includes the casing domain in the aerodynamic damping simulation. However, when performing this type of simulation, it is crucial to subtract the forcing effect of the casing before evaluating the aerodynamic damping. Therefore, the full model is simulated twice, once with a fixed blade to determine the forcing effect of the casing on the rotor (rotor-stator interaction) and once with vibrating blades to simulate combined forcing and damping. The forcing effect from the casing can then be eliminated after subtracting the respective flow field. This subtraction is based mainly on the assumption of the linear superposition of the pressure perturbation due to rotor-stator interaction and blade vibration [57].



**Figure 8.6:** CFD domains for aerodynamic damping calculation: (a) Full model (b) Isolated rotor model

An MC with four channels is chosen as a case study for this investigation. The MC4-100 configuration, which represents the full admission operation, has been chosen for the comparison between the isolated rotor and the full model simulations. Before starting this comparison, it is essential to ensure that all simulated cases have a comparable operating condition. Therefore the transient mean blade loading has been plotted at 50% rotor-span for the full model (with fixed and vibrating blades) and the isolated model to evaluate the change in the operating condition for different simulation cases as

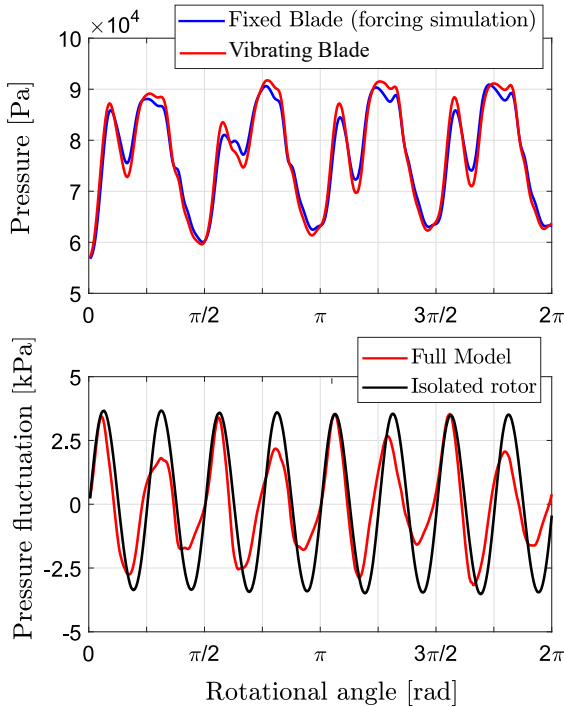
shown in Figure 8.7. The differences of the mean blade loading between the full model (fixed blade) and the isolated model are lower than 1.5%, while between the two full models with fixed and vibrating blades is lower than 0.2%. These deviation percentages are sufficient for a reliable pressure perturbation comparison.



**Figure 8.7:** Transient averaged blade loading at 50% span

After comparing the blade loading and ensuring a comparable operating conditions, the next step is to compare the pressure perturbation due to the blade motion for both models. Therefore, a monitor point has been selected on the blade trailing edge near the blade tip, where the maximum displacement takes place according to the investigated resonating mode shape (M1 ND3 EO8), as described in Figure 6.18. The pressure on this monitor point for both fixed blade and vibrating blades full model is shown at the top of Figure 8.8. The pressure perturbation due to the blade vibration is calculated using Equation 8.1 for both isolated rotor and full model and are plotted at the bottom of Figure 8.8.

$$\tilde{p} = \begin{cases} p_{iso, vib} - \bar{p}_{iso, vib} & \text{Isolated rotor model} \\ p_{full, vib} - p_{full, fix} & \text{Full model} \end{cases} \quad (8.1)$$

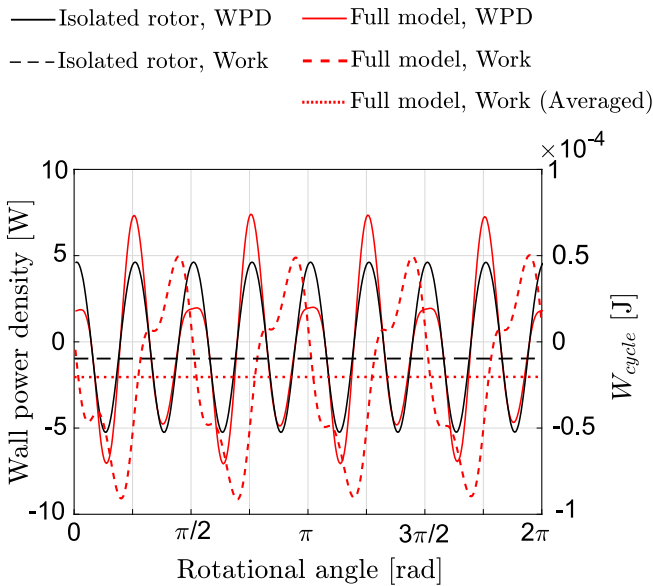


**Figure 8.8:** Top: Blade pressure for a complete revolution. Bottom: Pressure perturbation due to the blade vibration, MC4-100 at the blade tip

It is found that the pressure perturbation at the mentioned operating point for the two different models has a comparable pattern with slight differences. The one obtained from the isolated rotor model has constant amplitude and frequency equal to the vibration frequency. In the full model in contrary, it has a periodically varying amplitude representing the applied admission configuration. In this case, it changed periodically four times, which indicates the effect from the MC featuring four channels.

Although one monitor point is sufficient to explain the effect of the blade motion on the surrounding fluid, it is not sufficient for the overall assess-

ment. Therefore, the wall power density, which is represented by the area integral in Equation 2.27 is calculated for the isolated rotor and the full model. The calculated values for one blade revolution are shown in Figure 8.9. The wall power density for the isolated rotor is represented by a harmonic signal with only one frequency component (EO8), while for the full model, it is represented by harmonic signal consists of more than one frequency component (EO4, EO8, EO12). This variation is attributed to the casing shape and the operating admission configuration.



**Figure 8.9:** Wall power density and the work per cycle for a rotor blade, MC4-100

Based on the comparison in Figure 8.9, it is clear that the isolated rotor model cannot predict the effect of the casing on the pressure perturbation due to the blade vibration and consequently on the wall power density. On the other hand, the full model succeeds in capturing this effect. This comparison also shows that the assumption of the linear superposition is acceptable in this type of investigation because all of the compared aspects show a comparable behavior except a slight deviation, which is attributed to the casing effect on it as it has been shown in the pressure and wall power density comparison.



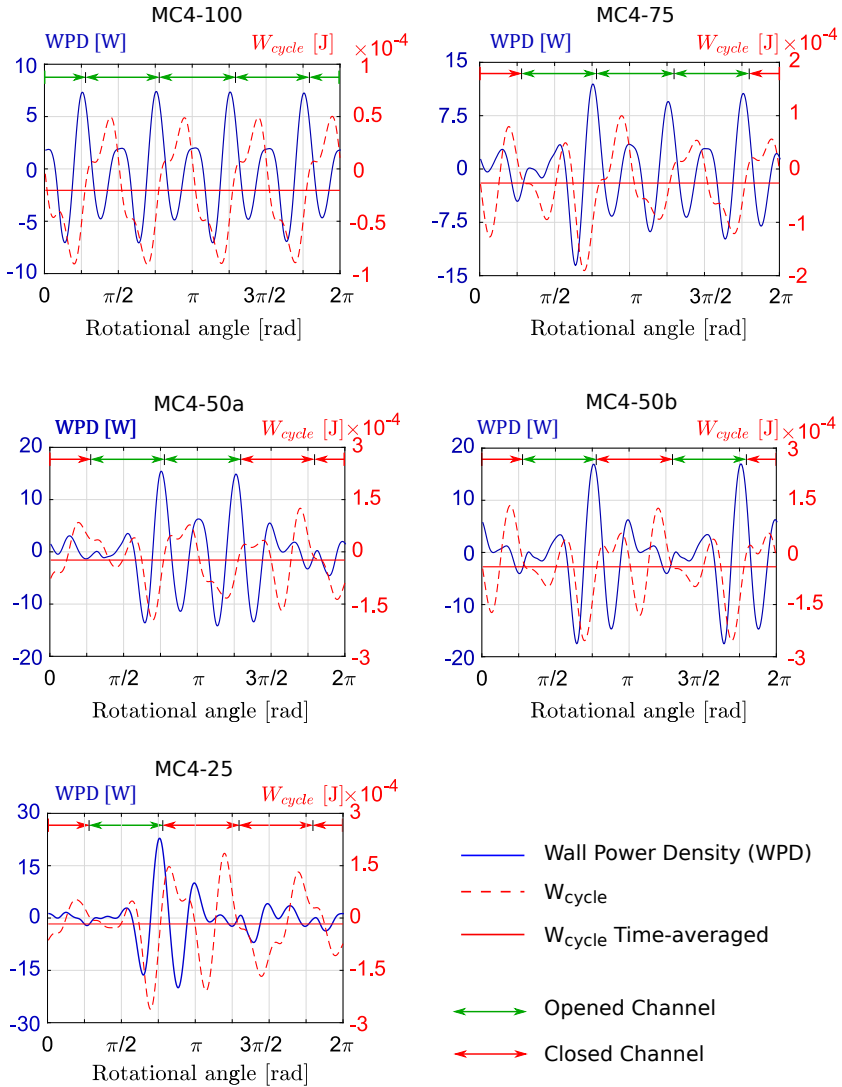
A moving window with a width of one blade vibration cycle is created, and the wall power density is integrated over this moving window to calculate the work done by the blade on the surrounding fluid. This integration results in a constant negative work in the case of the isolated rotor, while it shows a time-dependent work with a negative time-averaged value in the case of the full model. The transfer of work from the blade to the fluid is affected by the pressure of the casing.

After the comparison and result evaluation for the two different calculation models, the full model is chosen to calculate and evaluate the aerodynamic damping coefficient for different MC admission configurations. This choice is based on two reasons. First, it is recognized that the casing effect is not negligible. Second, the rotor operates at the correct conditions without the need to artificially readjust the boundary condition in the isolated analysis, which can be challenging. An evaluation of the wall power density and the aerodynamic work for different admission configurations is presented in Figure 8.10.

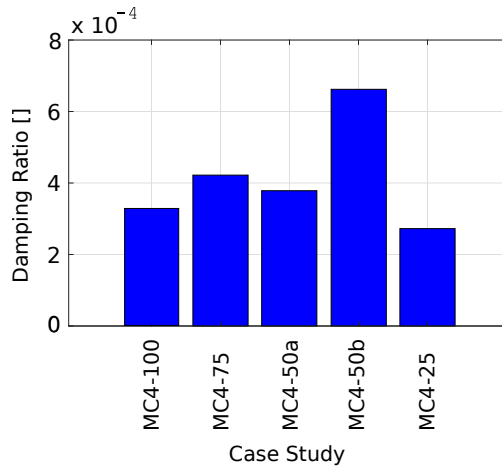
It is apparent that the pattern of the wall power density during one complete revolution is affected by the admission configuration. For instance, the wall power density in the case of MC4-100 has four repeated patterns, while in the case of MC4-50 has only two repeated patterns. For all admission configurations, the aerodynamic work changes massively over one revolution. The mean aerodynamic work is negative indicating that in total the blade loses energy, and its motion is damped. The mean aerodynamic work and hence the damping ratio is found to be significantly affected by the MC configuration.

Admission configuration MC4-50b has higher aerodynamic work, while MC4-25 has the lowest value. Although the cases MC4-50a and MC4-50b have the same operating pressure ratio and the same admission percentage, they show a noticeable difference in the aerodynamic work with configuration MC4-50b featuring almost twice as high aerodynamic work compared to MC4-50a. This observation indicates that the admission configurations have a significant effect on the energy exchange between the blade and surrounding fluid and hence the aerodynamic damping.

Figure 8.11 depicts the simulated damping ratio for all MC configuration. All configuration features a positive damping ratio. The value, however, varies significantly from  $2.55 \times 10^{-4}$  for MC4-25 to  $6.5 \times 10^{-4}$  for MC4-50b. The observation that MC4-50a and MC4-50b vary by 71% already indicates that the MC configuration has a substantial influence on the aerodynamic damping.



**Figure 8.10:** Wall power density and work per cycle for MC different admission configuration, full model



**Figure 8.11:** Damping ratios for different MC admission configurations.

### 8.3 Forced Response Analysis

In this section, a forced response analysis is performed using the mode superposition method to calculate the vibration amplitude and the dynamic stresses for different admission configurations. The harmonic loads are imported from the unsteady CFD simulation according to the EO of interest while the aerodynamic damping coefficients are taken from the test data as shown in Table 5.3.

The forced response analysis is performed for nine different cases which are tested experimentally as shown in Section 5.4. These nine cases represent three different admission configurations MC5-100, MC5-80, and MC5-60a and three different resonance crossing EO6, EO7, and EO8.

The tangential displacement of the blade tip for three different admission percentages at EO6 is shown in Figure 8.12. The Tangential Vibration Amplitude (TVA) differs from the Measured Vibration Amplitude (MVA) which is presented in Section 5.4 by the Correction Factor (CF) as represented in Figure 8.13 and Equation 8.2.

$$CF = \frac{TVA}{MVA} = 0.39 \quad (8.2)$$

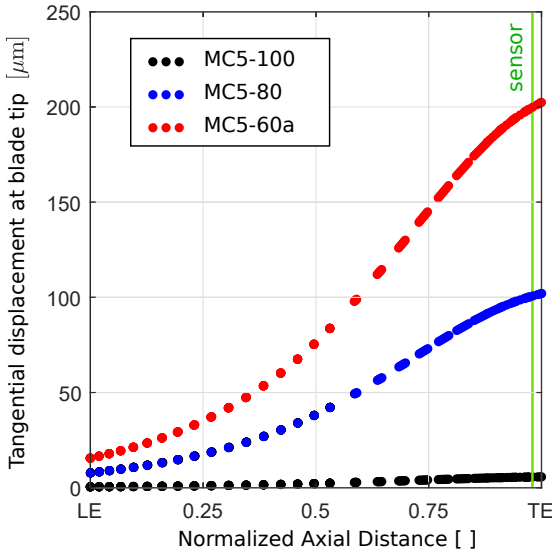


Figure 8.12: Blade tip displacement for different admission configuration, EO6

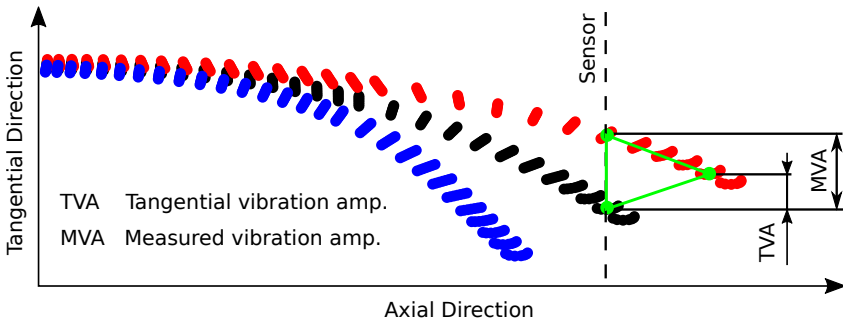
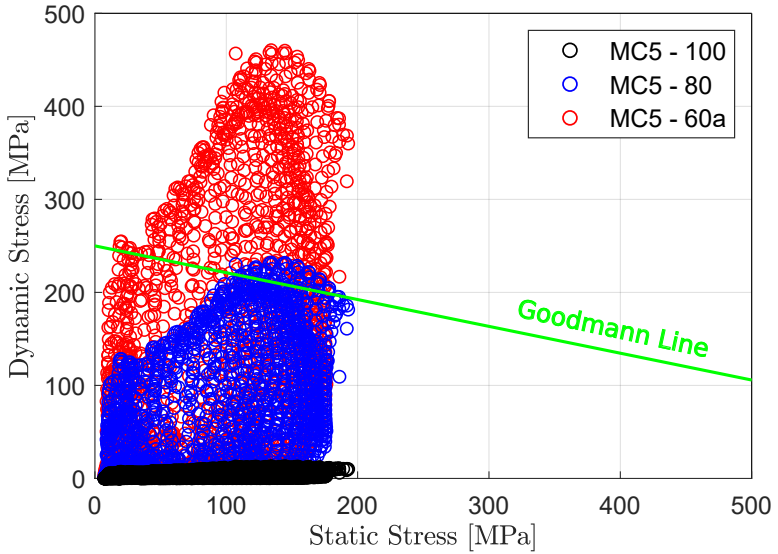


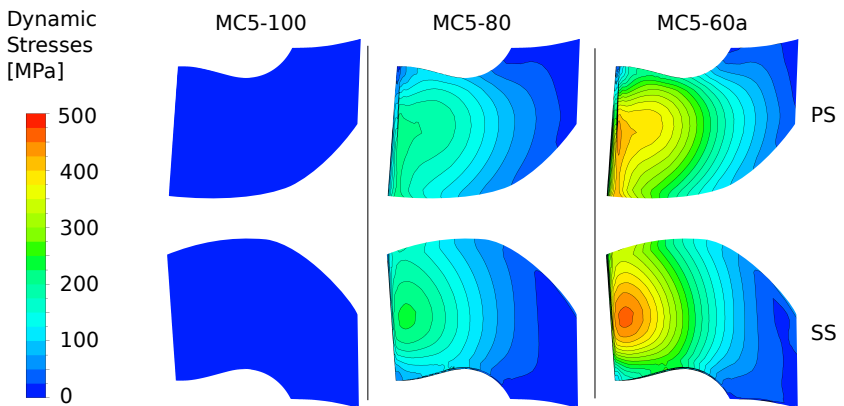
Figure 8.13: First bending mode at blade tip, scale 100:1

For the same three cases, the dynamic stresses at the rotor blade are illustrated by means of an Haigh diagram as shown in Figure 8.14 and by the contour plots as shown in Figure 8.15. This results shows how operating the turbine at a certain admission configuration and operating conditions would lead to HCF. Operating at the MC5-60a admission case leads to dy-

dynamic stresses two times more than the safe range as illustrated by the red circles on the Haigh diagram.

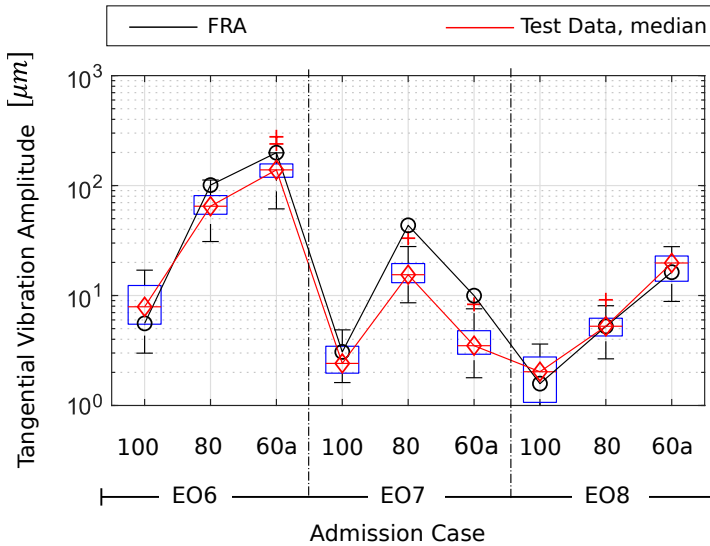


**Figure 8.14:** Haigh diagram for different admission configuration, EO6



**Figure 8.15:** Dynamic stresses contour for different admission configuration, EO6

The resultants TVA for all nine cases are plotted in comparison with the test data in Figure 8.16. The comparison shows that simulation results generally agree well with test data and that the trends are well-captured. It can therefore be concluded that the forced response analysis as conducted herein can be used to assess the aeromechanics behavior of radial turbines featuring a MC casing.



**Figure 8.16:** FRA tangential vibration amplitude validation

## 9 Conclusions and Future Work

This study intends to create and test a multichannel casing design model to replace the traditional spiral casing in a radial turbine. The intention of this replacement is to provide performance controllability using the partial admission idea without the need for neither movable parts nor complicated control mechanisms. Controlling the radial turbine by this new approach allows it to enter new applications such as the turbocharger for gasoline engines. Moreover, this study also highlights the effect of using the multi-channel casing and applying different partial admission configurations and percentages on some of the radial turbine design aspects such as the operating efficiency and blade vibration. This aims to avoid operating the turbine at low efficiency and avoid any high cyclic fatigue. The conclusions of this study are listed in the following sections.

### 9.1 Multi-channel Casing Design

- Seven geometrical parameters (Eqn. 4.5, and Fig. 4.2) are chosen to design the shape of the flow channel to achieve the required channel throat area and comparable mass flow to the original spiral casing while keeping acceptable operating efficiency.
- Channel count (Sec. 4.4.1) is one of the parameters that noticeably affect the performance of multi-channel casing turbines. Increasing it results in more homogeneous flow angles (Fig. 4.9) and reduces the flow recirculation at the rotor inlet (Fig. 4.7). This leads to a higher mass flow rate for the same casing size (Fig. 4.5). It achieves also higher operating efficiency for a comparable mass flow rate. The efficiency increases until reaching a certain channel count where the efficiency remains constant due to higher friction losses (Fig. 4.8). Special attention should be given for the selection of the channel count because

it affects other turbine design aspects such as aerodynamic excitation (Sec. 8.1).

- The ratio between the casing outlet and the rotor inlet diameters ( $D_2/D_3$ ) is used to define the turbine radial gap (Fig. 4.2). For the same turbine casing size, increasing the radial gap reduces the turbine mass flow rate (Fig. 4.10). It increases also the operating efficiency until a certain value where the efficiency drops again (Fig. 4.10).
- All other MC geometrical parameters are discussed together because they control the shape of the fluid channel. These parameters are reduced to three variables: the channel areas ratio ( $A_o/A_{th}$ ), channel diameters ratio ( $D_1/D_2$ ), and the channel inlet inclination angle ( $\theta_{L2}$ ). A combination of these variables generate different shape of the fluid channel (Tables 4.2, and 4.3) and affecting the turbine performance (Fig. 4.13, 4.14, 4.15, and 4.16).
- All these effects are included in a MC design tool to generate an MC 3D CAD model. This numerical tool runs iteratively (Fig. 4.17) until reaching the objective function by achieving a comparable mass flow rate and acceptable operating efficiency compared to the original turbine.

## 9.2 Effect of MC on the Turbine Performance

- The turbine operating efficiency at BEP decreases by decreasing the admission percentage. The unsteady CFD simulation has predicted this trend with sufficient accuracy based on the comparison with the test data (Fig. 7.2).
- Different partial admission configurations cause an unsteady flow disturbance even when operating at steady conditions (Fig. 7.3).
- Operating at partial admission causes shock losses, which depend mainly on the pressure difference between the open and closed channels, and admission percentage (Fig. 7.6).
- The turbine efficiency changes due to the geometrical optimization process are minor compared to the efficiency reduction due to different partial admission percentages (Fig. 7.11).



## 9.3 Effect of MC on the Blade Vibration

- Operating the turbine at a certain admission configurations increases the harmonic pressure load on the rotor blades and leads to higher excitation forces (Fig. 8.1). Therefore, building an excitation map for the turbine featuring an MC at all admission configuration on the operating range is crucial in the preliminary design phase.
- The increase of the excitation forces at certain admission configurations is attributed to two main reasons. Firstly, the change in the frequency spectrum i.e. creates harmonic pressure load at some EOs which featured no loads at the full admission. Secondly, lower admission percentage operated at a high expansion ratio which increases the harmonic pressure amplitude.
- The generalized force approach proved its capability in predicting the excitation forces (Fig. 8.3). Therefore, it's a useful tool to build the excitation map to avoid the turbine operation at high excitation forces.
- The full model approach is recommended to study the effect of the different MC admission configurations on the rotor aerodynamic damping (Fig. 8.9). Although the isolated rotor approach can save computational time, it is unable to predict this effect.
- The MC shape and admission configurations have a influence on the aerodynamic work and damping (Fig. 8.10).
- The change of the excitation forces due to applying certain admission configurations is more significant than the change in aerodynamic damping. Therefore, high excitation admission case results in high vibration amplitude and high dynamic stresses which could lead to HCF failure (Fig. 8.14).

## 9.4 Future Work

- After testing the multi-channel casing turbine on an hot gas test stand and shows a comparable mass flow and better efficiency compared to the original spiral casing turbine, the turbine should be tested in a

internal combustion engine test stand to prove the efficient turbine controllability in turbocharger application.

- Design a connecting mechanism to connect the turbocharger featuring a MC to the internal combustion engine with the minimum possible losses.
- Upgrade the MC design model by adding an optimization routine to generate the best efficient and safe MC geometry automatically.
- Test the MC casing design model on other turbines with different sizes and applications.

## References

- [1] Alfonsi, G.: Reynolds-averaged Navier–Stokes equations for turbulence modeling, *Applied Mechanics Reviews*, Bd. 62(4), 2009
- [2] ANSYS: ANSYS CFX-Pre User’s Guide 18.2, 2017
- [3] ANSYS: ANSYS CFX-Solver Modeling Guide 18.2, 2017
- [4] ANSYS: ANSYS CFX-theory guide 18.2, 2017
- [5] Atassi, H.: Unsteady aerodynamics, aeroacoustics, and aeroelasticity of turbomachines and propellers, Springer Science & Business Media, 2012
- [6] Balasubramanian, R.; Barrows, S.; Chen, J.: Investigation of shear-stress transport turbulence model for turbomachinery applications, in: 46th AIAA aerospace sciences meeting and exhibit, S. 566, 2008
- [7] Bejan, A.; Kestin, J.: Entropy generation through heat and fluid flow, *Journal of Applied Mechanics*, Bd. 50, S. 475, 1983
- [8] Capobianco, M.; Gambarotta, A.: Unsteady flow performance of turbo-charger radial turbines, in: Proceeding of the Institute of Mechanical Engineers, Fourth International Conference of Turbocharging and Turbochargers, S. 123–132, 1990
- [9] Capobianco, M.; Gambarotta, A.: Variable geometry and waste-gated automotive turbochargers: measurements and comparison of turbine performance, *Journal of Engineering for gas Turbines and Power*, Bd. 114(3), S. 553–560, 1992
- [10] Capobianco, M.; Marelli, S.: Experimental analysis of unsteady flow performance in an automotive turbocharger turbine fitted with a waste-gate valve, *Proceedings of the Institution of Mechanical Engineers, Part D: Journal of Automobile Engineering*, Bd. 225(8), S. 1087–1097, 2011
- [11] Cerdoun, M.; Ghenaiet, A.: Analyses of steady and unsteady flows in a turbocharger’s radial turbine, *Proceedings of the Institution of Mechanical Engineers, Part E: Journal of Process Mechanical Engineering*, Bd. 229(2), S. 130–145, 2015

- [12] Cerdoun, M.; Ghenaiet, A.: Unsteady behaviour of a twin entry radial turbine under engine like inlet flow conditions, *Applied Thermal Engineering*, Bd. 130, S. 93–111, 2018
- [13] Challand, S.; Dirschauer, E.: Exhaust Gas System for an Internal Combustion Engine, Patent no. WO2013150092, 2013
- [14] Challand, S.; Dirschauer, E.; Ilievski, M.; Casey, M.; Schatz, M.: A New Partial Admission Method for Turbocharger Turbine Control at Off-Design, in: *ASME Turbo Expo 2013: Turbine Technical Conference and Exposition*, ASME, Paper No. GT2013-95441, 2013
- [15] Clenci, A.; Descombes, G.; Podevin, P.; Hara, V.: Some aspects concerning the combination of downsizing with turbocharging, variable compression ratio, and variable intake valve lift, *Proceedings of the Institution of Mechanical Engineers, Part D: Journal of Automobile Engineering*, Bd. 221(10), S. 1287–1294, 2007
- [16] Copeland, C. D.; Newton, P. J.; Martinez-Botas, R.; Seiler, M.: The effect of unequal admission on the performance and loss generation in a double-entry turbocharger turbine, *Journal of Turbomachinery*, Bd. 134(2), S. 021004, 2012
- [17] Dixon, S. L.; Hall, C.: *Fluid mechanics and thermodynamics of turbomachinery*, Butterworth-Heinemann, 2013
- [18] Ebaid, M.; Bhinder, F.; Khdairi, G.: A unified approach for designing a radial flow gas turbine, *J. Turbomach.*, Bd. 125(3), S. 598–606, 2003
- [19] Elder, R.; Woods, I.; Patil, S.; Holmes, W.; Steed, R.; Hutchinson, B.: Investigation of efficient CFD methods for the prediction of blade damping, in: *ASME Turbo Expo 2013: Turbine Technical Conference and Exposition*, American Society of Mechanical Engineers Digital Collection, 2013
- [20] Feneley, A. J.; Pesiridis, A.; Andwari, A. M.: Variable geometry turbocharger technologies for exhaust energy recovery and Boosting—a review, *Renewable and sustainable energy reviews*, Bd. 71, S. 959–975, 2017
- [21] Flaxington, D.; DT, S.; et al.: Variable area radial-inflow turbine, 1982
- [22] Fransson, T. H.: *Unsteady Aerodynamics and Aeroelasticity of Turbomachines: Proceedings of the 8th International Symposium held in Stockholm, Sweden, 14–18 September 1997*, Springer Science & Business Media, 2012

- [23] Fuehrer, K.; Bloemers, D.; Zuefle, E.; Wuethrich, C.: Optische Überwachung von Turbinenschaufelschwingungen im Betrieb, VGB Kraftwerkstechnik, Bd. 73(1), S. 29–33, 1993
- [24] Fuhrer, C.: Simulation and Validation of an new Stator Design for Radial Turbines of Turbochargers, Master Thesis, Institute of Thermal Turbomachinery and Machine Laboratory, University of Stuttgart, 2014
- [25] Georgiev, V.; Holík, M.; Kraus, V.; Krutina, A.; Kubín, Z.; Liška, J.; Poupa, M.: The blade flutter measurement based on the blade tip timing method, in: Proceedings of the 15th WSEAS international conference on Systems, Corfu Island, Greece, S. 14–16, 2011
- [26] Giersch, T.; Hönisch, P.; Beirow, B.; Kühhorn, A.: Forced response analyses of mistuned radial inflow turbines, Journal of Turbomachinery, Bd. 135(3), 2013
- [27] Glahn, C.; Kluin, M.; Hermann, I.; Königstein, A.: Requirements for the Boosting System of Future Engine Concepts, MTZ worldwide, Bd. 78(4), S. 16–21, 2017
- [28] Güllich, J. F.: Centrifugal pumps, Bd. 2, Springer, 2008
- [29] Hagelstein, D.; Hasemann, H.; Rautenberg, M.: Coupled vibration of unshrouded centrifugal compressor impellers. Part II: computation of vibration behavior, International Journal of Rotating Machinery, Bd. 6, 2000
- [30] He, P.; Sun, Z.; Guo, B.; Chen, H.; Tan, C.: Aerothermal investigation of backface clearance flow in deeply scalloped radial turbines, Journal of turbomachinery, Bd. 135(2), 2013
- [31] Heath, S.; Imregun, M.: A survey of blade tip-timing measurement techniques for turbomachinery vibration, 1998
- [32] Heidinger, F.; Challand, S.; Vogt, D.: Development and commissioning of a new turbocharger test facility, in: The XXII Biannual Symposium on Measuring Techniques in Turbomachinery, Lyon, France, 2014
- [33] Hishikawa, A.; Okazaki, Y.; Busch, P.: Developments of variable area radial turbines for small turbochargers, Techn. Ber., SAE Technical Paper, 1988
- [34] Iandoli, C.: Analysis of the entropy generation fields of a low ns centrifugal compressor, ME Thesis, U. of Roma, Bd. 1, 2000
- [35] Iandoli, C.; Sciubba, E.: Entropy generation maps of a low-specific speed radial compressor rotor, in: Proc. AES/ASME W. Meeting, Orlando, FL, USA, 2000

- [36] Ilievski, M.; Heidinger, F.; Fuhrer, C.; Schatz, M.; Vogt, D. M.; Challand, S.: Experimental and Numerical Investigation of Partial Admission of a Radial Turbocharger Turbine for Improved Off-Design Operation, in: ASME Turbo Expo 2015: Turbine Technical Conference and Exposition, ASME, Paper No. GT2015-43318, 2015
- [37] Jones, W.; Launder, B. E.: The prediction of laminarization with a two-equation model of turbulence, *International journal of heat and mass transfer*, Bd. 15(2), S. 301–314, 1972
- [38] Kammerer, A.; Abhari, R. S.: Experimental study on impeller blade vibration during resonance? Part II: blade damping, *Journal of Engineering for Gas Turbines and Power*, Bd. 131(2), 2009
- [39] Kawashima, T.; Inuma, H.; Wakatsuki, T.; Minagawa, N.: Turbine blade vibration monitoring system, in: Proceedings of the 37th International Gas Turbine and Aeroengine Congress and Exposition, Cologne, Germany, S. 1–4, Citeseer, 1992
- [40] Ke, C.; Xiong, L.; Peng, N.; Dong, B.; Li, K.; Li, J.; Liu, L.: Numerical and experimental study of the performance effects of varying vaneless space in high-speed micro turbine stators, *Cryogenics*, Bd. 88, S. 10–16, 2017
- [41] Klaus, M.: Flow-induced blade vibrations in radial turbines with bladed volute casing, Logos-Verlag, 2007
- [42] Kock, F.; Herwig, H.: Local entropy production in turbulent shear flows: a high-Reynolds number model with wall functions, *International journal of heat and mass transfer*, Bd. 47(10-11), S. 2205–2215, 2004
- [43] Kramer, E.: Optical vibration measuring system for long, freestanding LP rotor blades, *ABB Review*, Bd. 5, 1997
- [44] Launder, B. E.; Sharma, B.: Application of the energy-dissipation model of turbulence to the calculation of flow near a spinning disc, *Letters in heat and mass transfer*, Bd. 1(2), S. 131–137, 1974
- [45] Li, X.; Zhu, Z.; Li, Y.; Chen, X.: Experimental and numerical investigations of head-flow curve instability of a single-stage centrifugal pump with volute casing, *Proceedings of the Institution of Mechanical Engineers, Part A: Journal of Power and Energy*, Bd. 230(7), S. 633–647, 2016
- [46] Losh, D.; Tappert, P.; John, S.; Mercadal, M.; Orlando, B.; Wood, H.: Sensor Placement Utility User Manual, Hood Technology Corp., 2011
- [47] Mayorca, M. A.: Numerical methods for turbomachinery aeromechanical predictions, Dissertation, Royal Institute of Technology, 2011

- [48] Mayorca, M. A.: Numerical Methods for Turbomachinery Aeromechanical Predictions, Dissertation, Königlich Technische Hochschule Stockholm, 2011
- [49] Mayorca, M. A.; Vogt, D. M.; Mårtensson, H.; Andersson, C.; Fransson, T. H.: Uncertainty of forced response numerical predictions of an industrial blisk-comparison with experiments, GT2012-69534, in: Proceedings of ASME Turbo Expo 2012, Copenhagen, Denmark, 11–15 June 2012
- [50] Mayorca, M. A.; Vogt, D. M.; Mårtensson, H.; Fransson, T. H.: Prediction of Turbomachinery Aeroelastic Behavior From a Set of Representative Modes, *Trans. ASME, J. Turbomach.*, Vol. 135(011032), 2013
- [51] McCarty, P. E.; Thompsonk Jr, J.: Development of a Noninterference Technique for Measurement of Turbine Engine Compressor Blade Stress, Tech. Rep., Arnold Engineering Development Center Arnold AFB TN, 1980
- [52] Menter, F. R.: Two-equation eddy-viscosity turbulence models for engineering applications, *AIAA journal*, Vol. 32(8), pp. 1598–1605, 1994
- [53] Monaco, L.: PARAMETRIC STUDY OF THE EFFECT OF BLADE SHAPE ON THE PERFORMANCE OF TURBOMACHINERY CASCADES: PART III A: AERODYNAMIC DAMPING BEHAVIOUR–COMPRESSOR PROFILES, 2010
- [54] Moustapha, H.; Zelesky, M. F.; Baines, N. C.; Japikse, D.: Axial and radial turbines, Vol. 2, Concepts NREC White River Junction, VT, 2003
- [55] Müller, L.; Verstraete, T.: Adjoint-Based Multi-Point and Multi-Objective Optimization of a Turbocharger Radial Turbine, *International Journal of Turbomachinery, Propulsion and Power*, Vol. 4(2), p. 10, 2019
- [56] Müller, T.: Construction of a MEDUSA Engine Arrangement and Its Experimental Examination on the Hot Gas Test Rig, Master Thesis, Institute of Thermal Turbomachinery and Machine Laboratory, University of Stuttgart, 2014
- [57] Müller, T. R.; Vogt, D. M.; Vogel, K.; Phillipsen, B. A.: Influence of Intrarow Interaction on the Aerodynamic Damping of an Axial Turbine Stage, in: *Turbo Expo: Power for Land, Sea, and Air*, Vol. 51159, p. V07CT36A019, American Society of Mechanical Engineers, 2018
- [58] Netzhammer, S.; Vogt, D. M.; Kraetschmer, S.; Leweux, J.; Blackburne, J.: Reducing Blade Force Response in a Radial Turbine by

- Means of Jet Injection, in: Turbo Expo: Power for Land, Sea, and Air, Vol. 58684, p. V07AT36A007, American Society of Mechanical Engineers, 2019
- [59] Netzhammer, S.; Vogt, D. M.; Kraetschmer, S.; Leweux, J.; Koengeter, A.: Aerodynamic excitation analysis of radial turbine blades due to unsteady flow from vaneless turbine housings, in: Turbo Expo: Power for Land, Sea, and Air, Vol. 50930, p. V07BT36A015, American Society of Mechanical Engineers, 2017
- [60] Newton, P.; Copeland, C.; Martinez-Botas, R.; Seiler, M.: An audit of aerodynamic loss in a double entry turbine under full and partial admission, International Journal of Heat and Fluid Flow, Vol. 33(1), pp. 70–80, 2012
- [61] Nguyen-Schäfer, H.: Rotordynamics of automotive turbochargers, Springer, 2015
- [62] Nieberding, W.; Pollack, J.: Optical detection of blade flutter, in: ASME 1977 International Gas Turbine Conference and Products Show, American Society of Mechanical Engineers Digital Collection, 1977
- [63] Pucher, H.; Zinner, K.: Maßnahmen zur Verbesserung von Drehmoment- und Beschleunigungsverhalten bei Abgasturboaufladung, in: Aufladung von Verbrennungsmotoren, pp. 161–213, Springer, 2012
- [64] Reynolds, O.: Iv. on the dynamical theory of incompressible viscous fluids and the determination of the criterion, Philosophical transactions of the royal society of london.(a.), (186), pp. 123–164, 1895
- [65] Rohlik, H. E.: Analytical Determination of Radial Inflow Turbine Design Geometry for Maximum Efficiency, Technical Note D-4384, National Aeronautics and Space Administration, 1968
- [66] Roth, H.: Vibration measurements on turbomachine rotor blades with optical probes, in: Measurement methods in rotating components of turbomachinery, pp. 215–224, 1980
- [67] Schatz, M.; Seeger, F.; Vogt, D. M.; Koch, S.; Notheis, D.; Wagner, U.; Koch, T.: Performance evaluation of an IC-engine with a novel partial admission turbocharger concept, in: 19. Internationales Stuttgarter Symposium, pp. 757–771, Springer, 2019
- [68] Schwinn, Q.: Cut-away view turbocharger, (NASA), 2003
- [69] Schwitzke, M.: Aerodynamic excitation of resonant blade vibrations in radial turbines, Vol. 61, Logos Verlag Berlin GmbH, 2015

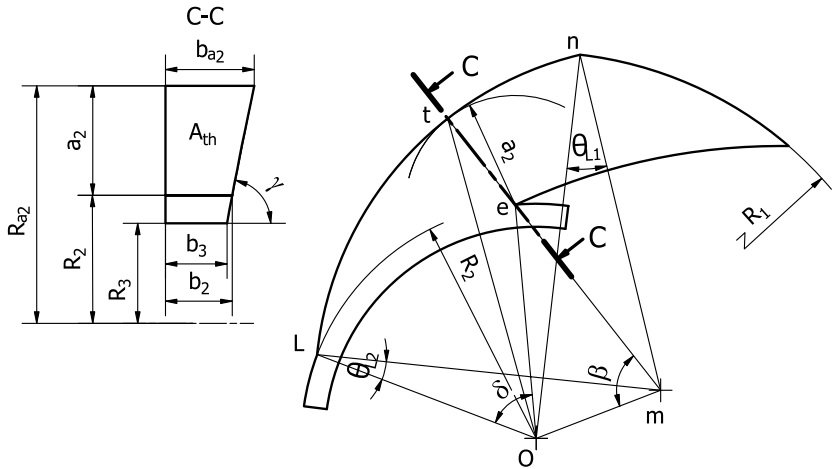


- [70] Sciubba, E.: Computing the Entropy Generation Rate for Turbomachinery Design Applications: Can a Diagnostic Tool Become a Predictive One?, in: ASME 2005 International Mechanical Engineering Congress and Exposition, pp. 179–192, ASME, Paper No. IMECE2005-79063, 2005
- [71] Simon, V.; Oberholz, G.; Mayer, M.: Exhaust Gas Temperature 1050 C, An Engineering Challenge, Borg Warner Turbo Systems Knowledge Library, Vol. 245, 2000
- [72] Simpson, A.; Spence, S.; Watterson, J.: Numerical and experimental study of the performance effects of varying vaneless space and vane solidity in radial turbine stators, *Journal of turbomachinery*, Vol. 135(3), 2013
- [73] Smagorinsky, J.: General circulation experiments with the primitive equations: I. The basic experiment, *Monthly weather review*, Vol. 91(3), pp. 99–164, 1963
- [74] Tang, H.; Pennycott, A.; Akehurst, S.; Brace, C. J.: A review of the application of variable geometry turbines to the downsized gasoline engine, *International Journal of Engine Research*, Vol. 16(6), pp. 810–825, 2015
- [75] Vasanthakumar, P.: Computation of aerodynamic damping for flutter analysis of a transonic fan, in: ASME 2011 Turbo Expo: Turbine Technical Conference and Exposition, pp. 1429–1437, American Society of Mechanical Engineers Digital Collection, 2011
- [76] Vogt, D. M.: Thermische Strömungsmaschinen, Institut für Thermische Strömungsmaschinen und Maschinenlaboratorium, Universität Stuttgart, vorlesungsmanuskript, 2017
- [77] Vogt, D. M.: Turbochargers, Institute of Thermal Turbomachinery and Machinery Laboratory, lecture note, 2017
- [78] Waldherr, C.; Müller, T.: FVV project blade forces, Tech. Rep., ITSM, University of Stuttgart, 2015
- [79] Watkins, W.; Robinson, W.; Chi, R.: Noncontact engine blade vibration measurements and analysis, in: 21st Joint Propulsion Conference, p. 1473, 1985
- [80] Watkins, W. B.; Chi, R. M.: Noninterference blade-vibration measurement system for gas turbine engines, *Journal of Propulsion and Power*, Vol. 5(6), pp. 727–730, 1989
- [81] Wilcox, D. C.: Formulation of the kw turbulence model revisited, *AIAA journal*, Vol. 46(11), pp. 2823–2838, 2008

- 
- [82] Wilcox, D. C.; et al.: Turbulence modeling for CFD, Vol. 2, DCW industries La Canada, CA, 1998
  - [83] Zablotskii, I.; Korostelev, Y. A.; Sviblov, L.: Contactless measuring of vibrations in the rotor blades of turbines, Tech. Rep., Foreign Technology Div Wright-Patterson AFB OH, 1974
  - [84] Zemp, A.; Abhari, R. S.; Ribi, B.: Experimental Investigation of Forced Response Impeller Blade Vibration in a Centrifugal Compressor With Variable Inlet Guide Vanes: Part 1?Blade Damping, in: ASME 2011 Turbo Expo: Turbine Technical Conference and Exposition, pp. 1369–1380, American Society of Mechanical Engineers Digital Collection, 2011
  - [85] Zimmermann, R.; Baar, R.; Biet, C.: Determination of the isentropic turbine efficiency due to adiabatic measurements and the validation of the conditions via a new criterion, Proceedings of the Institution of Mechanical Engineers, Part C: Journal of Mechanical Engineering Science, Vol. 232(24), pp. 4485–4494, 2018

# A Geometrical Relations

## A.1 Throat Area (Equation 4.1)



$\therefore m$  is the center of the left arc with radius  $R_L$

$$\therefore \overline{mL} = \overline{mt} = \overline{mn} = R_L$$

$$\therefore R_L = \overline{mt} = a_2 + \overline{me}$$

$$\therefore a_2 = R_L - \overline{me}$$

(A.1)

In  $\Delta omn$  &  $\Delta oml$

$$\therefore \overline{om}^2 = R_L^2 + R_1^2 - 2 R_L R_1 \cos \theta_{L1}$$

$$\therefore \overline{om}^2 = R_L^2 + R_2^2 - 2 R_L R_2 \cos \theta_{L2}$$

$$\therefore R_L = \frac{R_1^2 - R_2^2}{2(R_1 \cos \theta_{L1} - R_2 \cos \theta_{L2})}$$

(A.2)

In  $\Delta omL$

$$\therefore \overline{om} = \sqrt{R_L^2 + R_2^2 - 2 R_L R_2 \cos \theta_{L2}} \quad (\text{A.3})$$

$$\therefore \frac{R_L}{\sin(L\hat{om})} = \frac{\overline{om}}{\sin \theta_{L2}}$$

$$\therefore (L\hat{om}) = \sin^{-1}\left(\frac{R_L \sin \theta_{L2}}{\overline{om}}\right) \quad (\text{A.4})$$

$$\therefore e\hat{om} = L\hat{om} - \delta \quad (\text{A.5})$$

$$\overline{me} = \sqrt{R_2^2 + \overline{om}^2 - 2 R_2 \overline{om} \cos(e\hat{om})} \quad (\text{A.6})$$

In  $\Delta ome$

$$\therefore \frac{\overline{me}}{\sin(e\hat{om})} = \frac{R_2}{\sin \beta}$$

$$\therefore \beta = \sin^{-1}\left(\frac{\sin(e\hat{om}) R_2}{\overline{me}}\right) \quad (\text{A.7})$$

In  $\Delta omt$

$$R_{a2} = \overline{to} = \sqrt{R_L^2 + \overline{om}^2 - 2 R_L \overline{om} \cos \beta} \quad (\text{A.8})$$

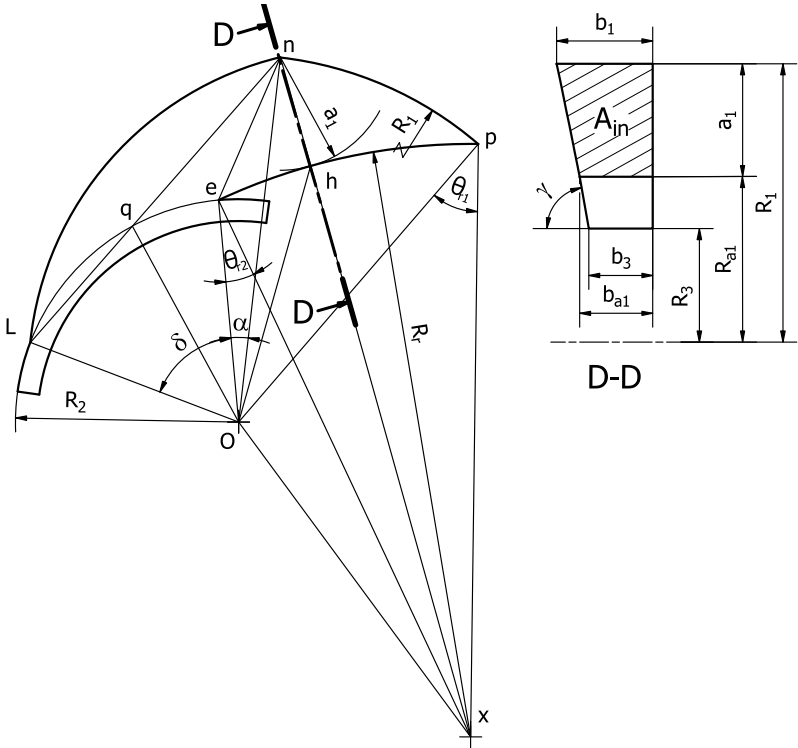
In Section view C-C

$$b_2 = b_3 + \frac{R_2 - R_3}{\tan \gamma} \quad (\text{A.9})$$

$$b_{a2} = b_3 + \frac{R_{a2} - R_3}{\tan \gamma} \quad (\text{A.10})$$

$$A_{th} = \left(\frac{b_2 + b_{a2}}{2}\right) a_2 \quad (\text{A.11})$$

## A.2 Inlet Area



$\therefore x$  is the center of the right arc with radius  $R_r$

$$\therefore R_r = \overline{ex} = \overline{hx} = \overline{nx} - a_2$$

$$a_1 = \overline{nx} - R_r$$

(A.12)

In  $\Delta opx$  &  $\Delta oex$

$$\therefore \overline{ox}^2 = R_r^2 + R_1^2 - 2 R_r R_1 \cos \theta_{r1}$$

$$\therefore \overline{ox}^2 = R_r^2 + R_2^2 - 2 R_r R_2 \cos \theta_{r2}$$

$$\therefore R_r = \frac{R_1^2 - R_2^2}{2(R_1 \cos \theta_{r1} - R_2 \cos \theta_{r2})}$$

(A.13)

$$\overline{ox} = \sqrt{R_r^2 + R_2^2 - 2 R_r R_2 \cos \theta_{r2}} \quad (\text{A.14})$$

In  $\Delta eox$

$$\begin{aligned} \therefore \frac{R_r}{\sin(e\hat{ox})} &= \frac{\overline{ox}}{\sin \theta_{r2}} \\ \therefore (e\hat{ox}) &= \sin^{-1}\left(\frac{R_r \sin \theta_{r2}}{\overline{ox}}\right) \end{aligned} \quad (\text{A.15})$$

In  $\Delta noq$

$$\therefore n\hat{oq} = \theta_{L1} + \theta_{L2} \quad (\text{A.16})$$

$$\begin{aligned} \therefore \overline{nq} &= \sqrt{R_1^2 + R_2^2 - 2 R_1 R_2 \cos(n\hat{oq})} \\ \therefore \overline{nq} &= \sqrt{R_1^2 + R_2^2 - 2 R_1 R_2 \cos(\theta_{L1} + \theta_{L2})} \end{aligned} \quad (\text{A.17})$$

$$\begin{aligned} \therefore \frac{R_2}{\sin(q\hat{no})} &= \frac{\overline{nq}}{\sin n\hat{oq}} \\ \therefore (q\hat{no}) &= (L\hat{no}) = \sin^{-1}\left(\frac{R_2 \sin n\hat{oq}}{\overline{nq}}\right) \end{aligned} \quad (\text{A.18})$$

In  $\Delta nol$

$$\therefore n\hat{oL} = 180 - (\theta_{L1} + \theta_{L2} + 2(L\hat{no})) \quad (\text{A.19})$$

$$\therefore \alpha = n\hat{oL} - \delta \quad (\text{A.20})$$

In  $\Delta nox$

$$\therefore n\hat{ox} = e\hat{ox} - \alpha \quad (\text{A.21})$$

$$\overline{nx} = \sqrt{\overline{ox}^2 + R_1^2 - 2 \overline{ox} R_1 \cos n\hat{ox}} \quad (\text{A.22})$$

In  $\Delta nox$

$$\begin{aligned} \therefore \frac{R_1}{\sin(o\hat{x}h)} &= \frac{\overline{nx}}{\sin(n\hat{ox})} \\ \therefore (o\hat{x}h) &= \sin^{-1}\left(\frac{R_1 \sin(n\hat{ox})}{\overline{nx}}\right) \end{aligned} \quad (\text{A.23})$$

In  $\Delta hox$

$$R_{a1} = \overline{oh} = \sqrt{R_r^2 + \overline{ox}^2 - 2 R_r \overline{ox} \cos(o\hat{x}h)} \quad (\text{A.24})$$

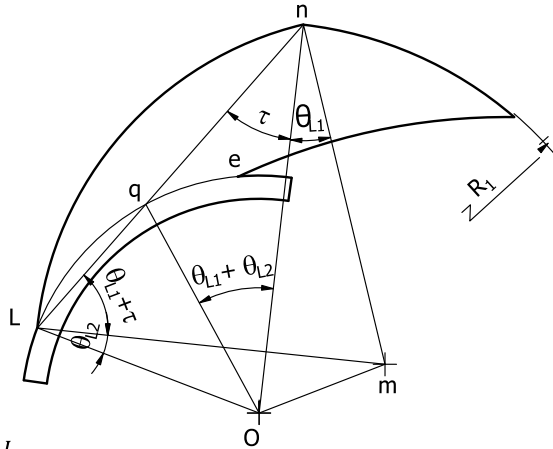
In Section view D-D

$$b_1 = b_3 + \frac{R_1 - R_3}{\tan \gamma} \tag{A.25}$$

$$b_{a1} = b_3 + \frac{R_{a1} - R_3}{\tan \gamma} \tag{A.26}$$

$$A_{in} = \left( \frac{b_1 + b_{a1}}{2} \right) a_1 \tag{A.27}$$

**Proof of Eqn. (A.16) and Eqn.(A.19)**



In Δ nmL

$$\therefore \overline{mn} = \overline{mL} = R_1$$

$$\therefore m\hat{n}L = m\hat{L}n = \theta_{L1} + \tau$$

In Δ oqL

$$\therefore \overline{oq} = \overline{oL} = R_2$$

$$\therefore o\hat{L}q = o\hat{q}L = \theta_{L1} + \theta_{L2} + \tau$$

In Δ noq

$$\therefore o\hat{q}L = n\hat{o}q + q\hat{n}o = \theta_{L1} + \theta_{L2} + \tau$$

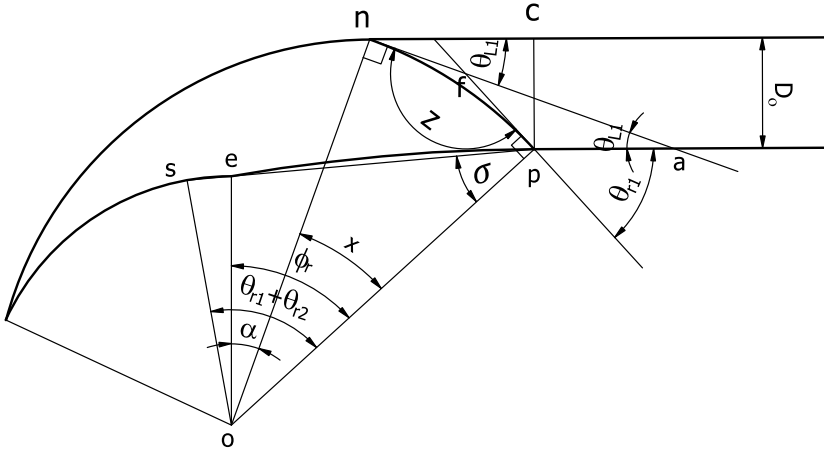
$$\therefore q\hat{n}o = \tau$$

$$n\hat{o}q = \theta_{L1} + \theta_{L2} \tag{A.16}$$

In Δ noL

$$n\hat{o}L = 180 - (\theta_{L1} + \theta_{L2} + 2(L\hat{n}o)) \tag{A.19}$$

### A.3 Inlet tube angles and diameter



$\overline{nc}$  and  $\overline{pa}$  are parallel and tangent to the channel arcs.

$sop = \theta_{r1} + \theta_{r2}$  ..... by analogy to equation (A.16)

In  $\Delta sop$

$$\overline{sp} = \sqrt{R_1^2 + R_2^2 - 2R_1R_2 \cos(\theta_{r1} + \theta_{r2})}$$

$$\therefore \frac{R_2}{\sin(\sigma)} = \frac{\overline{sp}}{\sin(\theta_{r1} + \theta_{r2})}$$

$$\therefore (\sigma) = \sin^{-1}\left(\frac{R_2 \sin(\theta_{r1} + \theta_{r2})}{\overline{sp}}\right)$$

$$\therefore o\hat{s}p = 180 - (\theta_{r1} + \theta_{r2} + \sigma)$$

In  $\Delta ose$

$$\therefore \overline{os} = \overline{oe} = R_1$$



$$\begin{aligned}\therefore o\hat{s}p &= o\hat{e}s = 180 - (\theta_{r1} + \theta_{r2} + \sigma) \\ \therefore o\hat{e}p &= 180 - o\hat{e}s = 180 - (180 - (\theta_{r1} + \theta_{r2} + \sigma)) \\ &\therefore o\hat{e}p = \theta_{r1} + \theta_{r2} + \sigma\end{aligned}$$

In  $\Delta oep$

$$\varphi_r = 180 - (\theta_{r1} + \theta_{r2} + 2\sigma) \quad (\text{A.28})$$

$$\therefore x = \varphi_r - \alpha$$

$$\therefore Z = 180 - x$$

$$\therefore a\hat{f}p + z = 180$$

$$\therefore a\hat{f}p = \theta_{r1} - \theta_{L1}$$

$$\therefore Z = 180 - \theta_{r1} + \theta_{L1}$$

$$\therefore 180 - \varphi_r + \alpha = 180 - \theta_{r1} + \theta_{L1}$$

$$\therefore \varphi_r = \theta_{r1} - \theta_{L1} + \alpha \quad (\text{A.29})$$

From equations (A.28) and (A.29)

$$\theta_{r1} = \frac{180 + \theta_{L1} - \theta_{r2} - 2\sigma - \alpha}{2} \quad (\text{A.30})$$

Where  $\alpha$  can be found in equ. A.20

In  $\Delta nop$

$$\overline{np} = \sqrt{R_1^2 + R_1^2 - 2R_1R_1 \cos(x)}$$

In  $\Delta npc$

$$\therefore (c\hat{n}p) = \theta_{L1} + (a\hat{n}p)$$

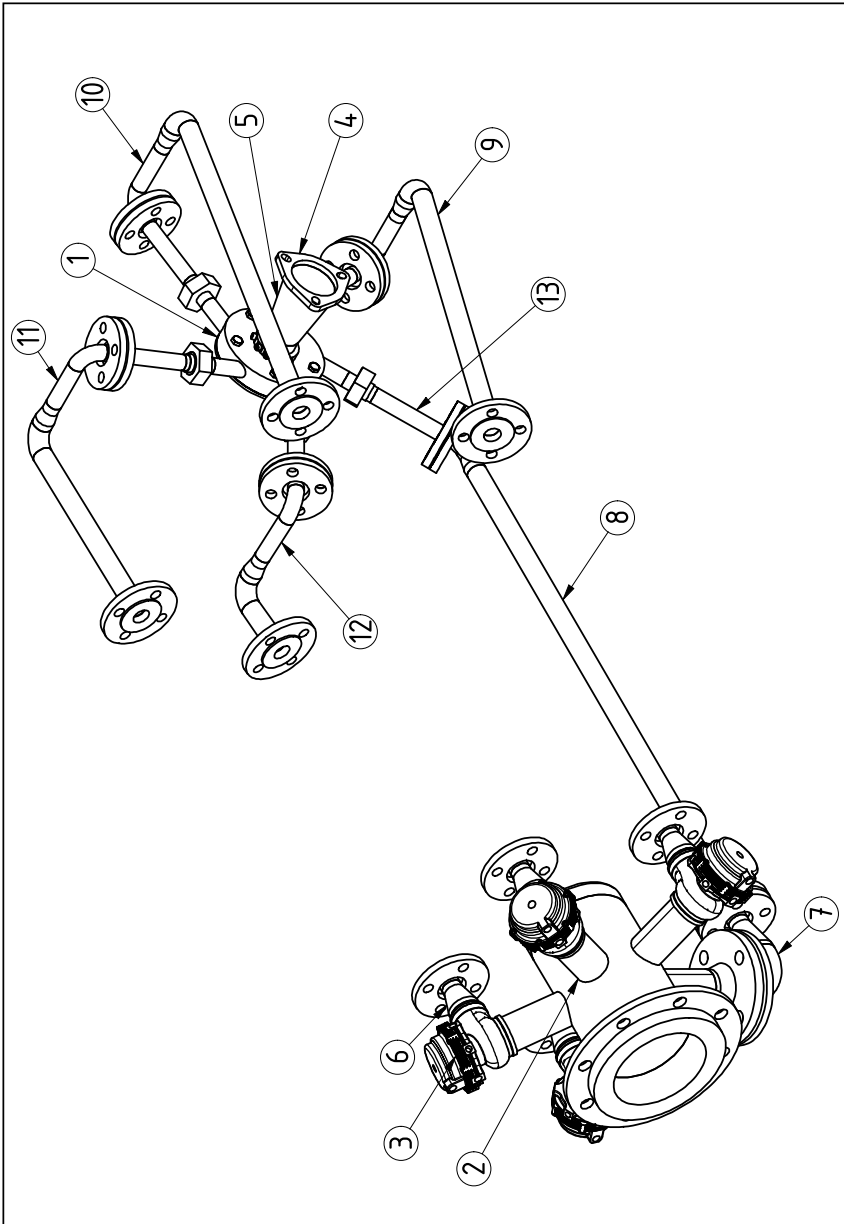
$$\therefore (a\hat{n}p) = \frac{180 - Z}{2} = \frac{\theta_{r1} - \theta_{L1}}{2}$$

$$\therefore (c\hat{n}p) = \theta_{L1} + \frac{\theta_{r1} - \theta_{L1}}{2} = \frac{\theta_{r1} + \theta_{L1}}{2}$$

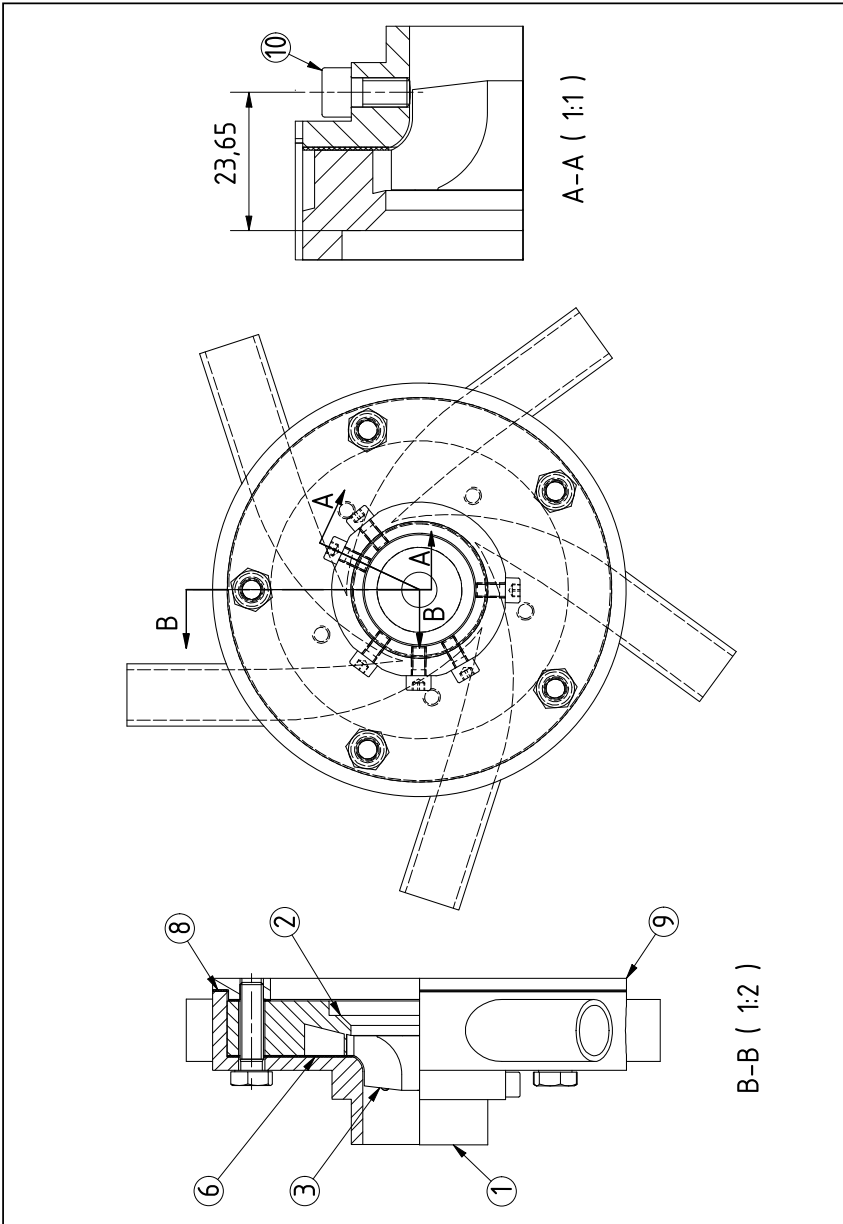
$$\therefore D_o = \overline{cp} = \overline{np} \sin\left(\frac{\theta_{r1} + \theta_{L1}}{2}\right) \quad (\text{A.31})$$



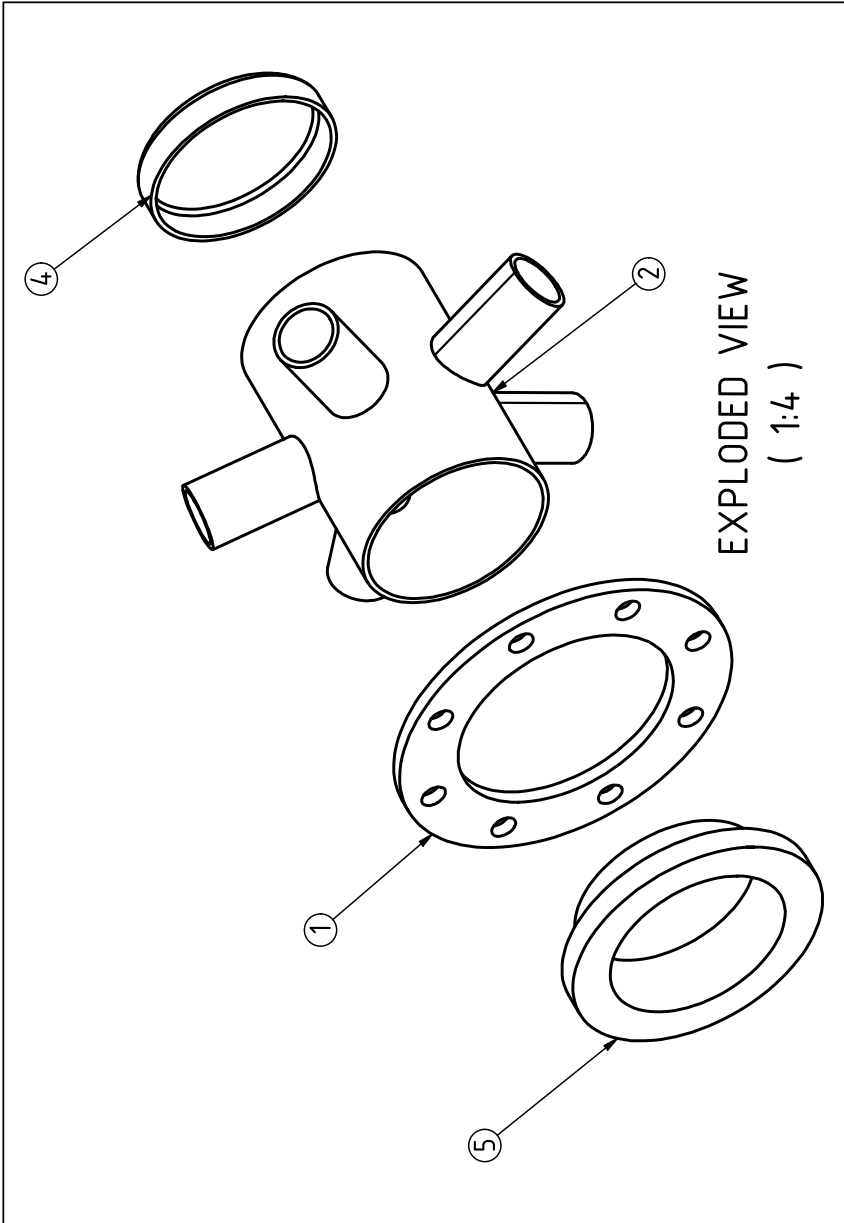
## **B Detail Drawing**



PART LIST			
SN	ITEM	QTY	DESCRIPTION
1	TURBINE CASING	1	SHEET # 2
2	FLOW DISRIBUTOR	1	SHEET # 3
3	WASTE GATE VALVE	4	Waste Gate Tial MV-S 38mm
4	TURBINE OUTLET FLANGE	1	SHEET # 7
5	OUTLET DIFFUSER	1	SHEET # 8
6	REDUCTION CONE	4	SHEET # 10
7	90 deg REDUCTION CONE	1	SHEET # 11
8	CHANNEL 1 CONECTOR	1	SHEET # 12
9	CHANNEL 2 CONECTOR	1	SHEET # 13
10	CHANNEL 3 CONECTOR	1	SHEET # 14
11	CHANNEL 4 CONECTOR	1	SHEET # 15
12	CHANNEL 5 CONECTOR	1	SHEET # 16
13	TURBINE INLET TUBE	5	SHEET # 17

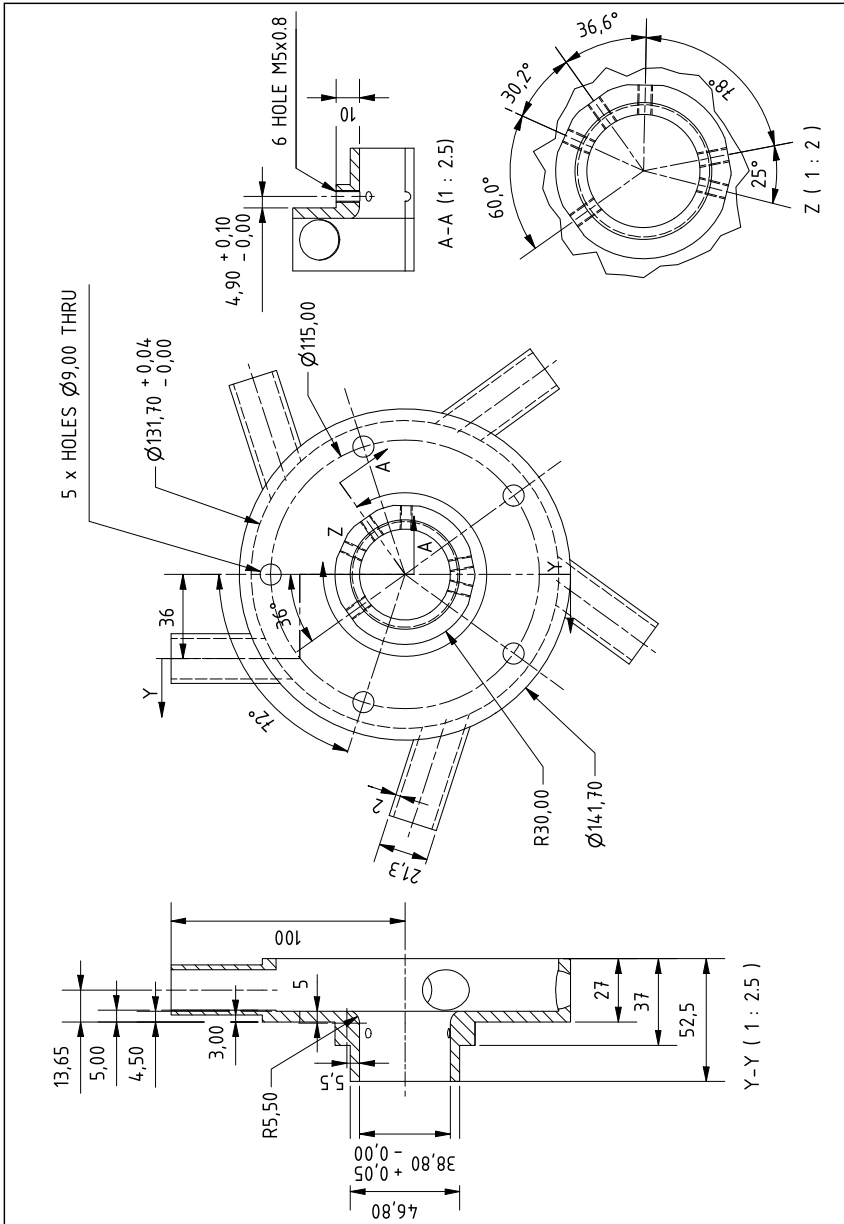


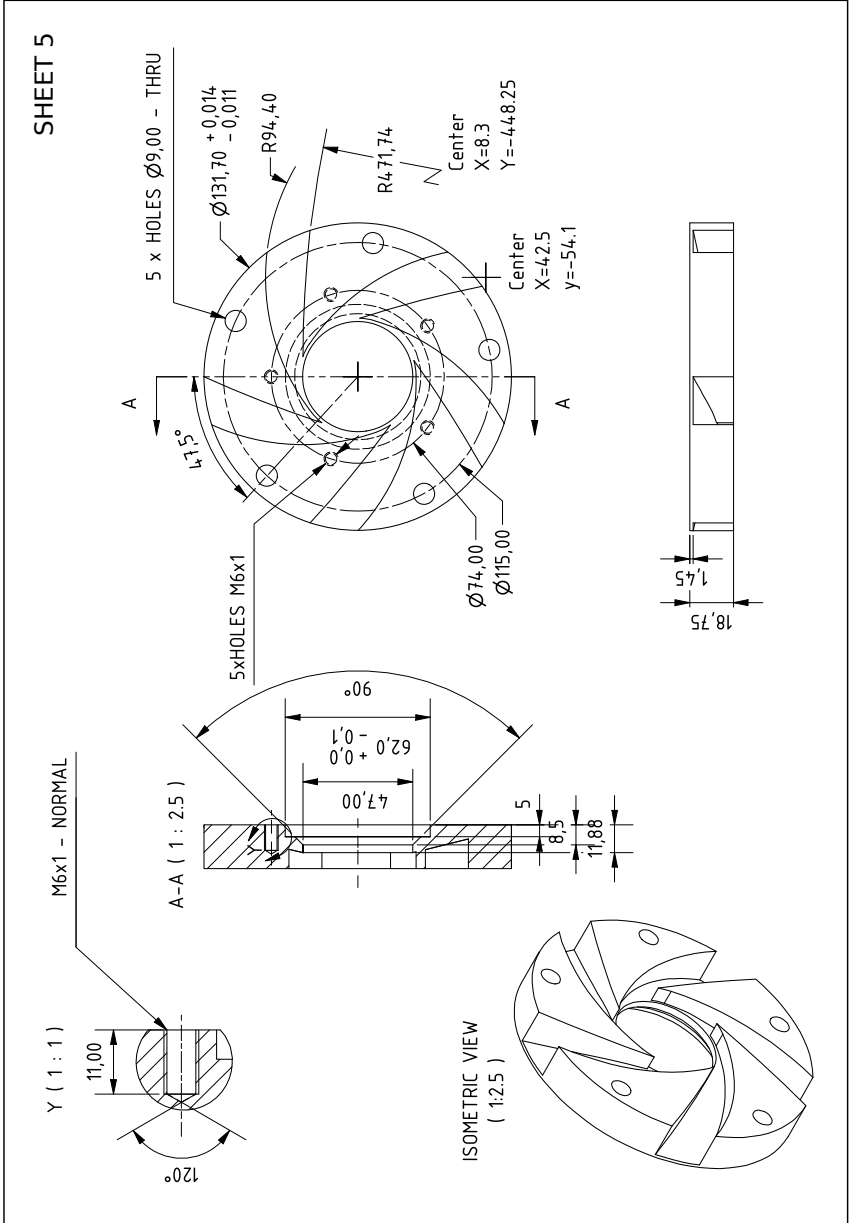
PARTS LIST			
ITEM	QTY	PART NUMBER	DESCRIPTION
1	1	SHROUD COVER	SHEET # 4
2	1	HUB COVER	SHEET # 5
3	1	Rotor	
4	5	DIN 933 - M8 x 30	Hex-Head Bolt
6	1	Copper Sealing 1	
7	1	Copper Sealing 2	
8	1	Copper Sealing 3	
9	1	SEALING RING	SHEET # 6
10	6	DIN 912 - M5 x 10	Cylinder Head Cap Screw



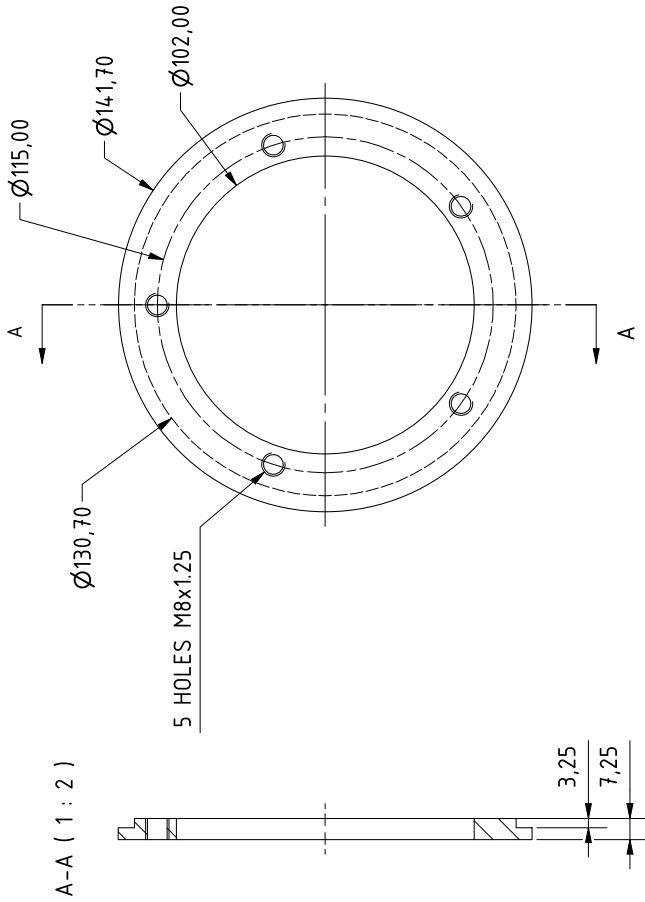


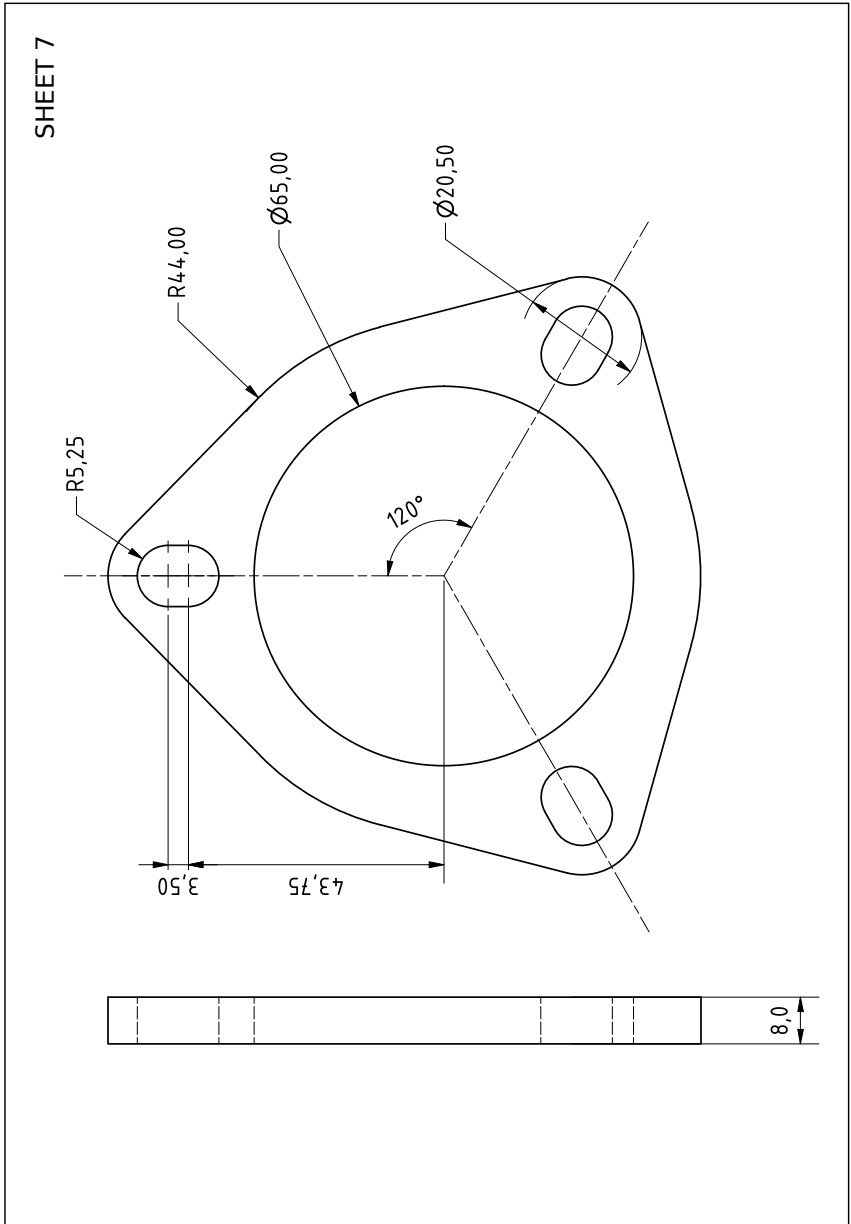
PARTS LIST			
ITEM	QTY	PART NUMBER	DESCRIPTION
1	1	Losser Flansch PN 16	DN 125/ 139,7 EN 1092-1/04, 1.4571, 4.75 kg
2	1	DISRIBUTOR BODY	SHEET # 9
5	1	Vorschweißbund PN 16	DN 125/ 139,7 EN 1092-1/34, 1.4571, 2.88 kg
4	1	Klöpferboden	Dn125 S4



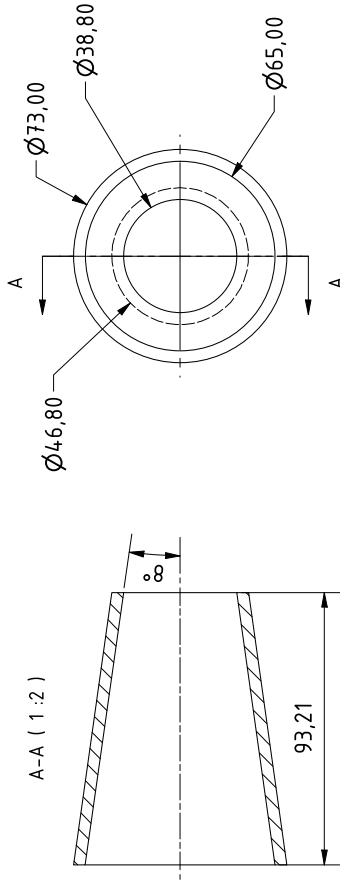


SHEET 6

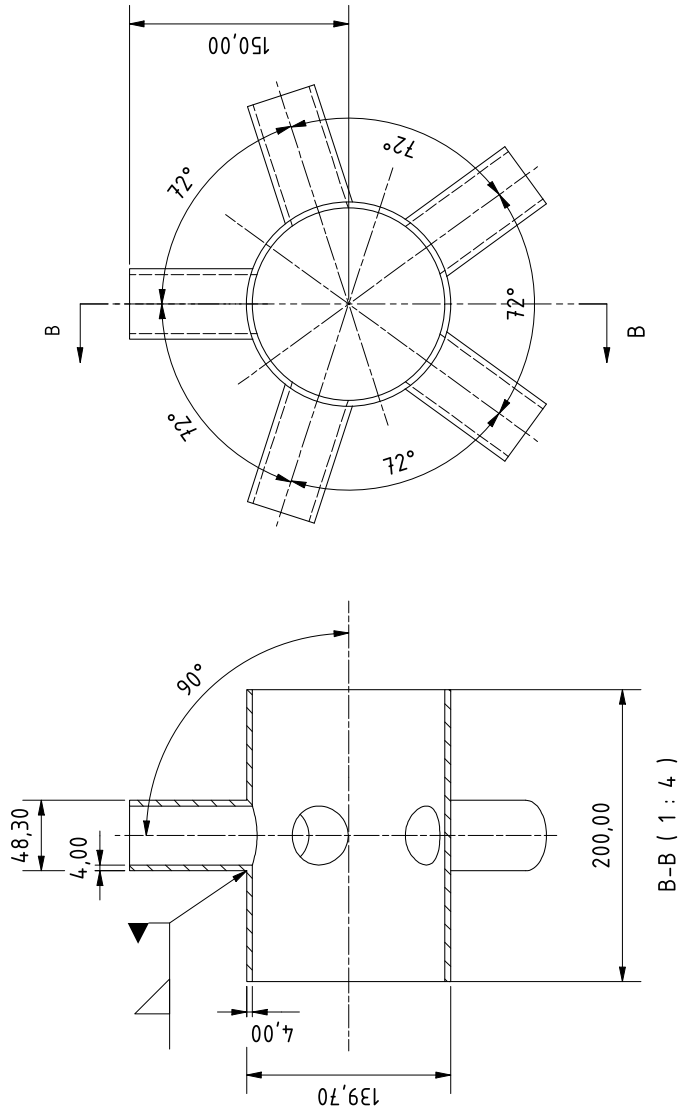




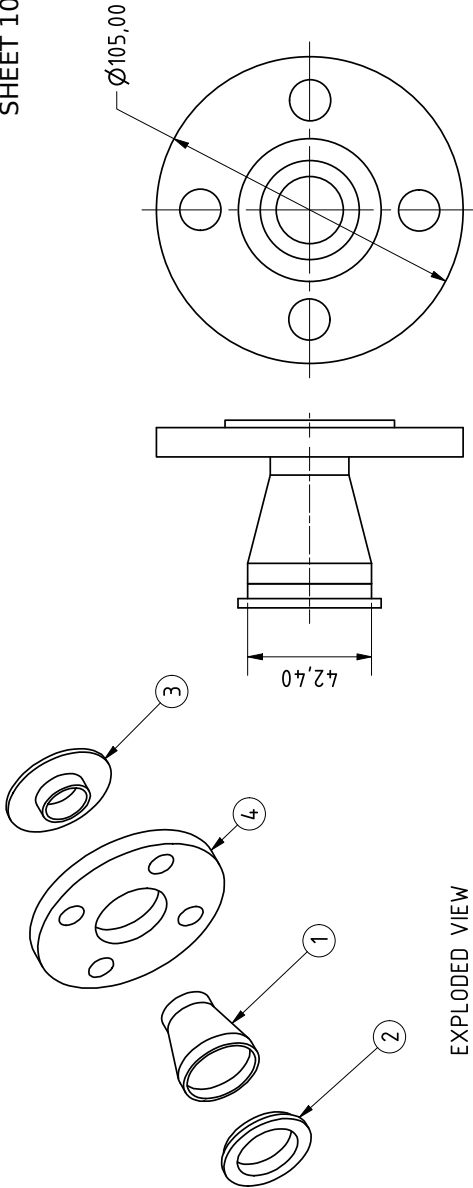
SHEET 8



SHEET 9



SHEET 10

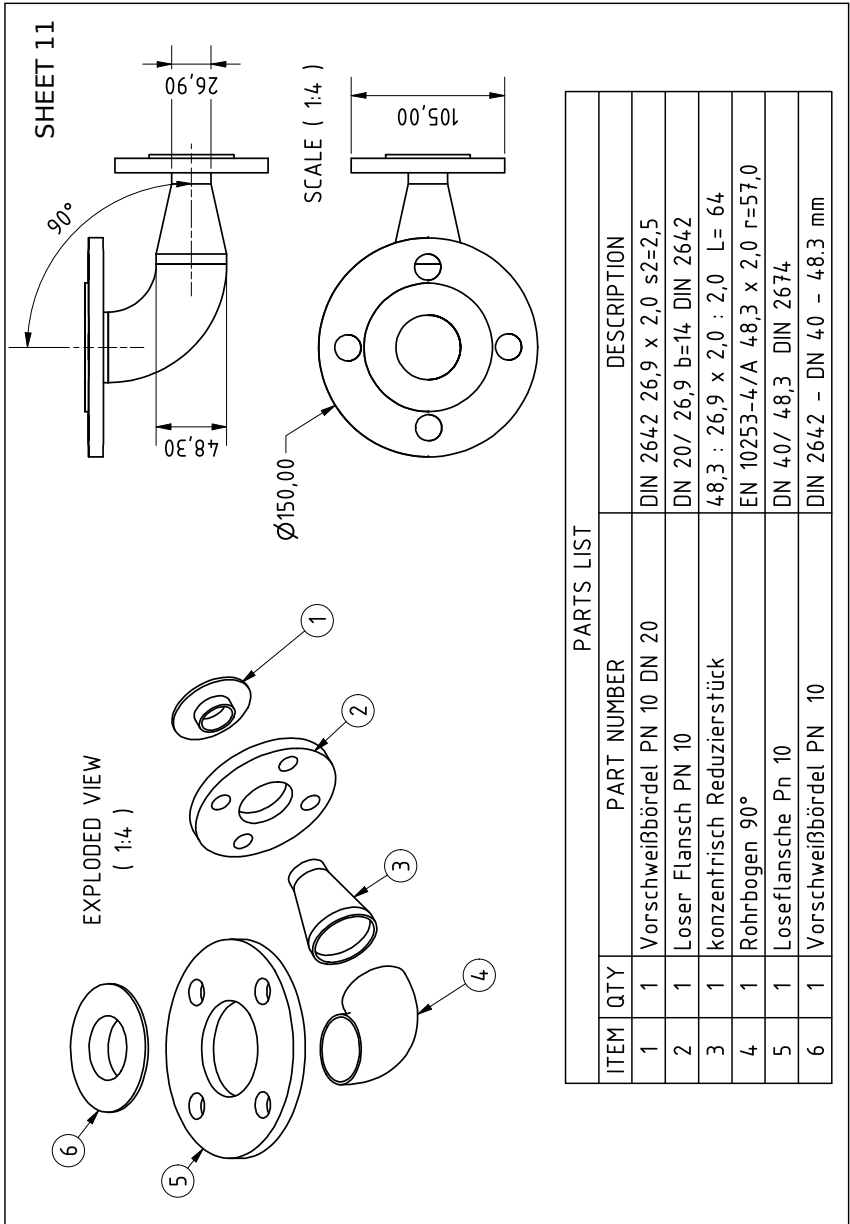


EXPLODED VIEW  
( 1:3 )

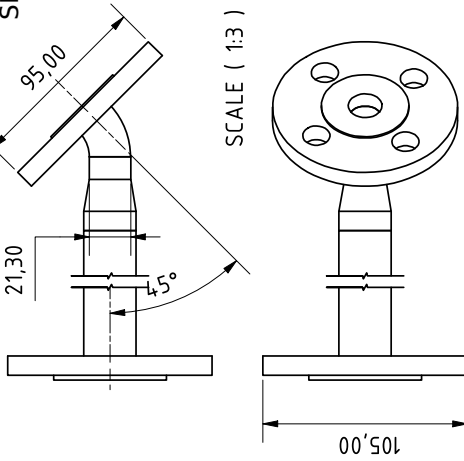
SCALE ( 1:2 )

ITEM		PARTS LIST	
QTY	PART NUMBER	DESCRIPTION	
1	Konzentrisch Reduzierstück	DIN EN 10253-4/A 42,4/ 26,9 x 2,0/2,0 L= 50	
2	Outlet F V-Band Flange	Waste Gate Tial MV-S 38mm	
3	Vorschweißbördel PN 10 DN 20	DIN 2642 26,9 x 2,0 s2=2,5	
4	Loser Flansch PN 10	DN 20/ 26,9 b=14 DIN 2642	

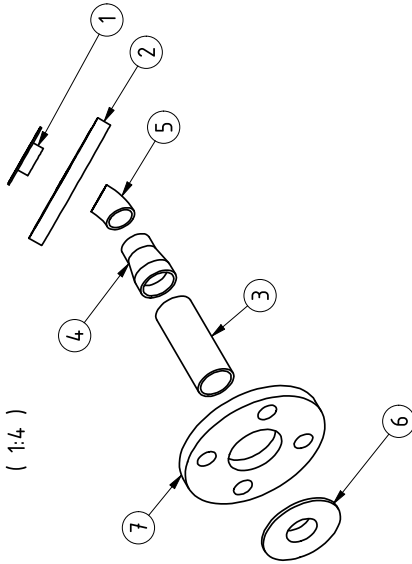




SHEET 12

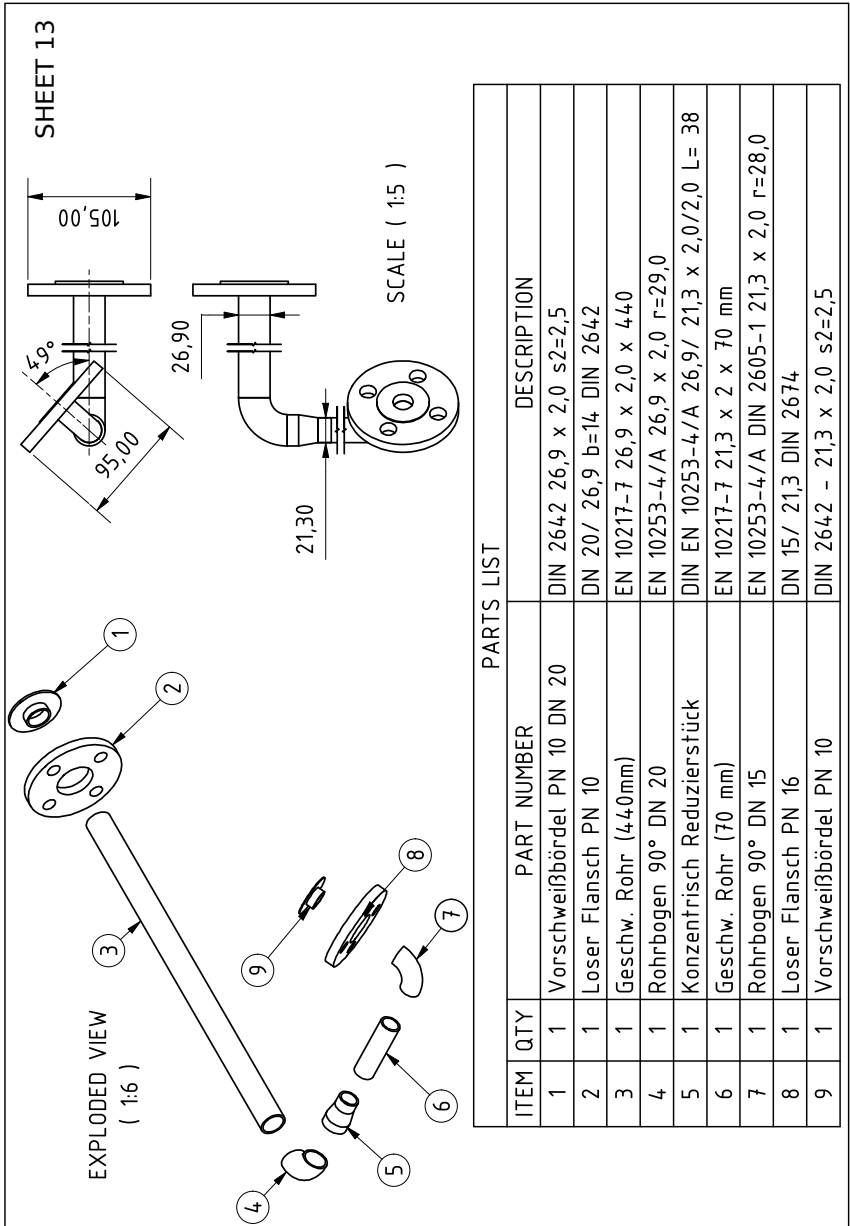


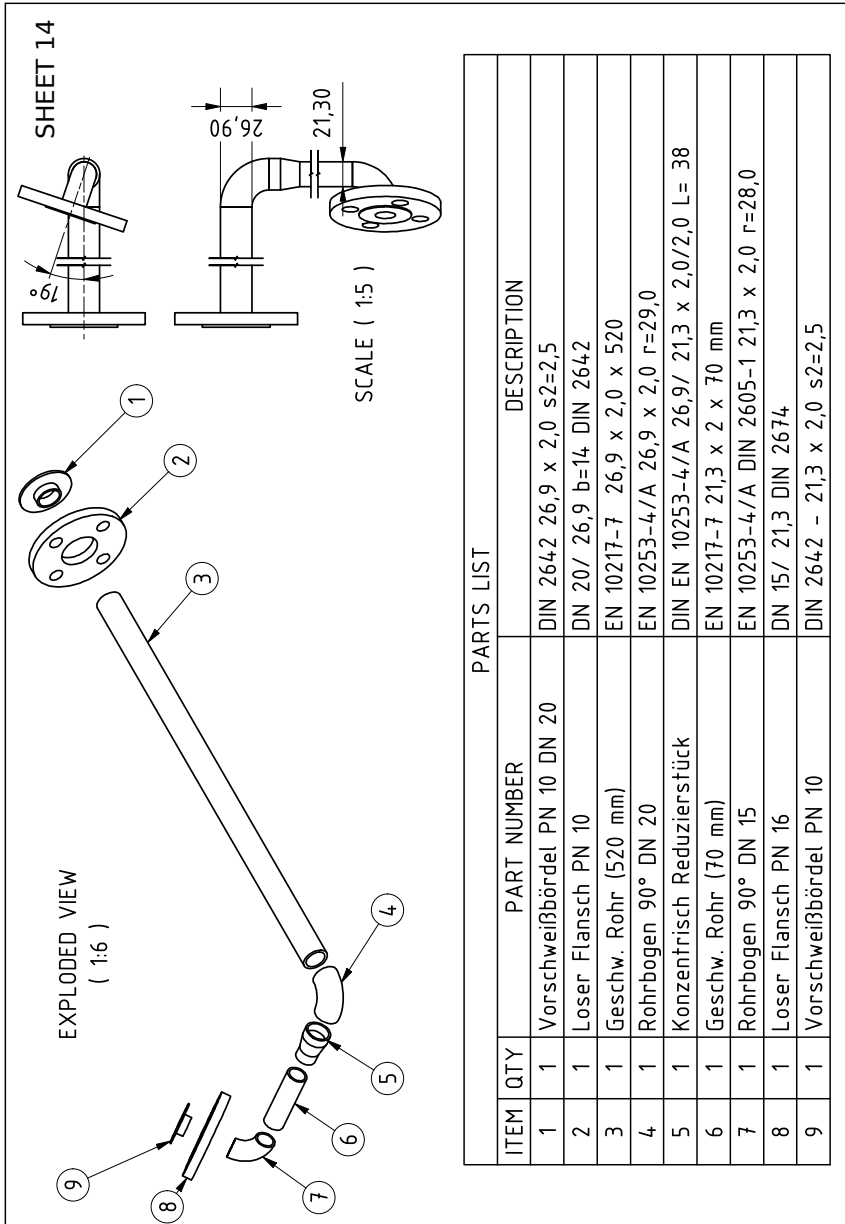
EXPLODED VIEW  
( 1:4 )

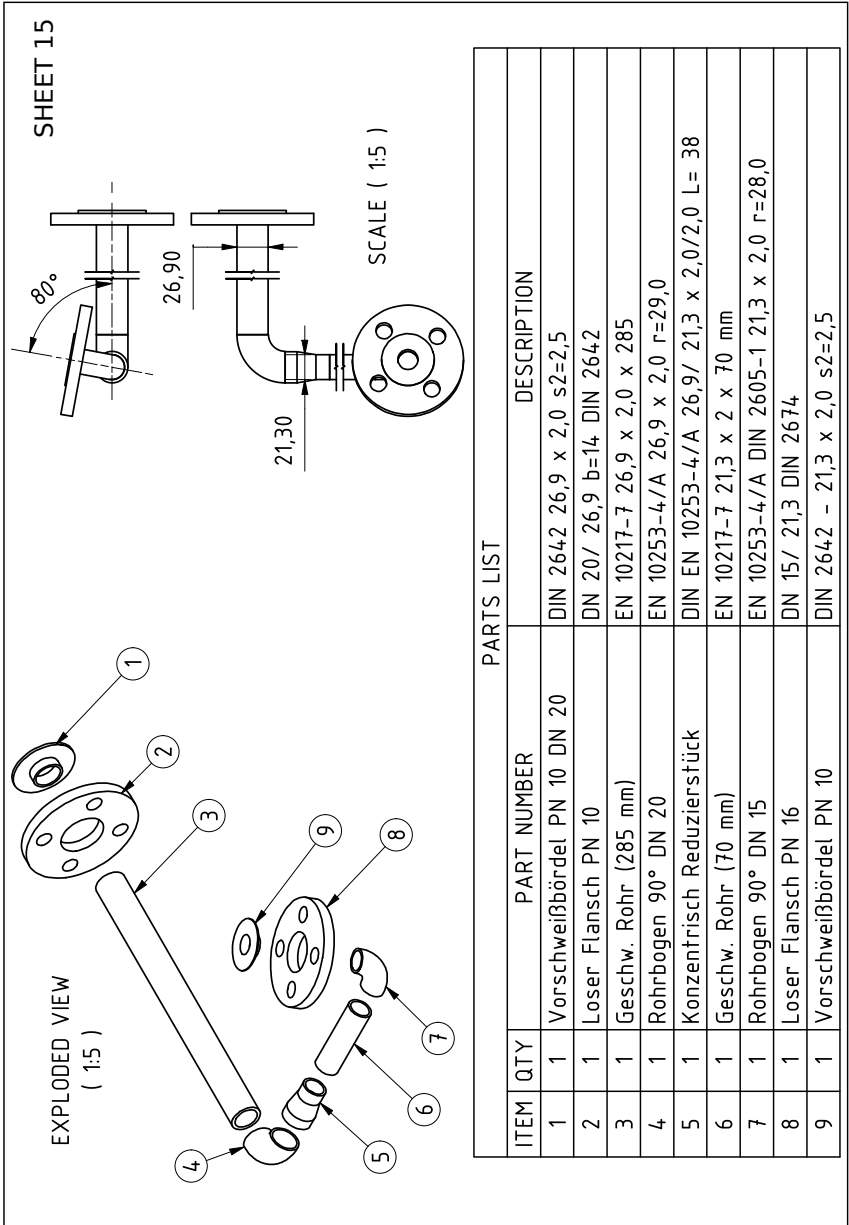


PARTS LIST

ITEM	QTY	PART NUMBER	DESCRIPTION
1	1	Vorschweißbördel PN 10	DIN 2642 - 21,3 x 2,0 s2=2,5
2	1	Losser Flansch PN 16	DN 15/ 21,3 DIN 2674
3	1	Geschw. Rohr L=800mm	EN 10217-7 26,9 x 2,0 x 800
4	1	Konzentrisch Reduzierstück	DIN EN 10253-4/A 26,9/ 21,3 x 2,0/2,0 L= 38
5	1	45° Rohrbogen	DIN 2605/ EN 10253 21,3 x 2,0 r=28,0
6	1	Vorschweißbördel PN 10 DN 20	DIN 2642 26,9 x 2,0 s2=2,5
7	1	Losser Flansch PN 10	DN 20/ 26,9 b=14 DIN 2642

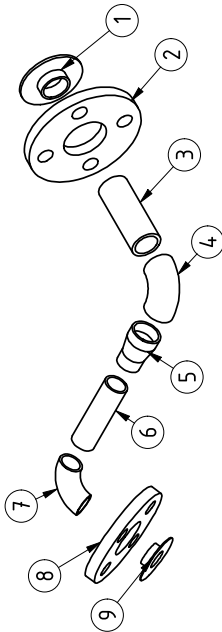




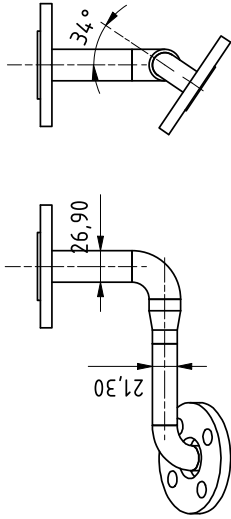


SHEET 16

EXPLODED VIEW  
( 1:5 )



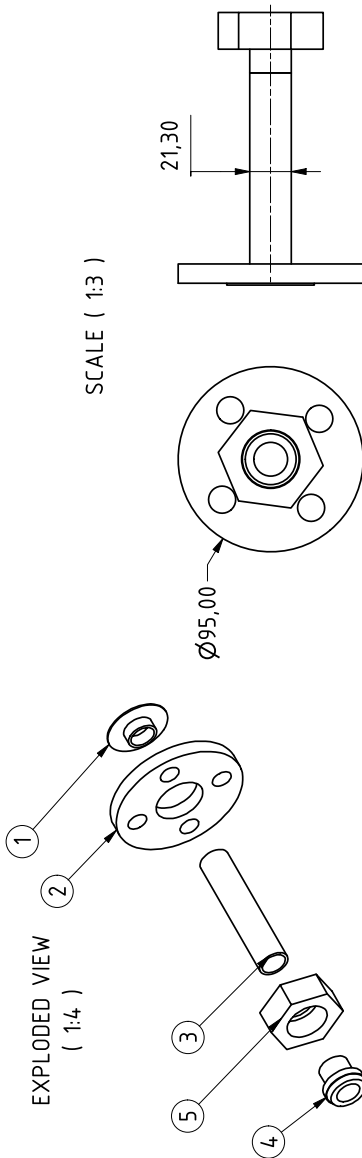
SCALE ( 1:5 )



PARTS LIST

ITEM	QTY	PART NUMBER	DESCRIPTION
1	1	Vorschweißbördel PN 10 DN 20	DIN 2642 26,9 x 2,0 s2=2,5
2	1	Losser Flansch PN 10	DN 20/ 26,9 b=14 DIN 2642
3	1	Geschw. Rohr	EN 10217-7 26,9 x 2,0 x 70
4	1	Rohrbogen 90° DN 20	EN 10253-4/A 26,9 x 2,0 r=29,0
5	1	Konzentrisch Reduzierstück	DIN EN 10253-4/A 26,9/ 21,3 x 2,0/2,0 L= 38
6	1	Geschw. Rohr (70 mm)	EN 10217-7 21,3 x 2 x 70 mm
7	1	Rohrbogen 90° DN 15	EN 10253-4/A DIN 2605-1 21,3 x 2,0 r=28,0
8	1	Losser Flansch PN 16	DN 15/ 21,3 DIN 2674
9	1	Vorschweißbördel PN 10	DIN 2642 - 21,3 x 2,0 s2=2,5

SHEET 17



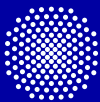
PARTS LIST			
ITEM	QTY	PART NUMBER	DESCRIPTION
1	1	Vorschweißbördel PN 10	DIN 2642 - 21,3 x 2,0 s2=2,5
2	1	Loser Flansch PN 16	DN 15/ 21,3 DIN 2674
3	1	Geschw. Rohr (100 mm)	EN 10217-7 21,3 x 2 x 100 mm
4	1	Anschweiß-Verschraubung teile 3	konisch dichtend R-134 S leicht 1/2" 21,3 x 2mm
5	1	Anschweiß-Verschraubung teile 2	konisch dichtend R-134 S leicht 1/2" 21,3 x 2mm





Radial turbines have proven their capability in many applications, due to their ability to operate at high-pressure ratios, structure robustness, and inherent cost advantages compared to the axial turbine. Controlling their performance allows efficient operation, even when operating at off-design conditions. Various control concepts are used for this purpose. These concepts depend mainly on movable parts and complicated control mechanisms, which limits radial turbines usability in some applications. Hence the need rises for a new control concept based entirely on fixed parts.

This thesis delivers a new control concept for radial turbines. The idea behind this concept is to replace the traditional spiral casing with a new Multi-channel casing. This casing consists of multiple channels. The main advantage of this new concept is that it is based only on fixed geometry, and the control valves could be placed away upstream of the turbine. Therefore the turbine can operate under control in any application requiring higher temperature ranges and smaller turbine size.



**University of Stuttgart**  
Germany